EXHAUST COMPOSITION IN A SMALL INTERNAL COMBUSTION ENGINE USING FTIR SPECTROSCOPY

THESIS

Kevin P. Horn, Captain, USAF

AFIT-ENY-MS-15-J-042

DEPARTMENT OF THE AIR FORCE
AIR UNIVERSITY

AIR FORCE INSTITUTE OF TECHNOLOGY

Wright-Patterson Air Force Base, Ohio

AFIT-ENY-MS-15-J-042

EXHAUST COMPOSITION IN A SMALL INTERNAL

COMBUSTION ENGINE USING FTIR SPECTROSCOPY

THESIS

Presented to the Faculty

Department of Aeronautical Engineering

Graduate School of Engineering and Management

Air Force Institute of Technology

Air University

Air Education and Training Command

in Partial Fulfillment of the Requirements for the

Degree of Master of Science in Aeronautical Engineering

Kevin P. Horn, B.S.M.E.

Captain, USAF

June 18th, 2015

AFIT-ENY-MS-15-J-042

EXHAUST COMPOSITION IN A SMALL INTERNAL

COMBUSTION ENGINE USING FTIR SPECTROSCOPY

THESIS

Kevin P. Horn, B.S.M.E.
Captain, USAF

Committee Membership:

Dr. Marc D. Polanka (Chairman)

Dr. Andrew W. Caswell (Member)

Dr. Paul I. King (Member)

Major James Rutledge, PhD (Member)

AFIT-ENY-MS-15-J-042

Abstract

The mission-specific needs of small, remotely piloted aircraft demand lighter, more efficient engines with increased performance for their propulsion systems. A wide range of experimental efforts were undertaken to further the ability to obtain performance data on small engines as well as to develop understanding of their operation. Data were collected to quantify friction losses present in the dynamometer drivetrain on the small engine research bench. A correction and calibration model was developed for brake power collected by the dynamometer. Mechanical efficiencies for 28 cm^3, 55 cm^3 and 85 cm^3 engines were 92.4%, 91.3% and 89.7%, respectively. Maximum fuel conversion efficiency for the three engines was calculated to be 14.9%, 15.4% and 18.3% at peak power, respectively. A 55 cm^3 two-stroke engine was converted to electronic fuel injection and its performance was tested and compared to the same engine equipped with a carburetor. Peak power was comparable between carbureted and EFI configurations. Fuel consumption, as measured by brake specific fuel consumption, was reduced significantly. Time-averaged and crank-angle resolved methods for the analysis of exhaust gasses in a 55 cm^3 two-stroke engine using Fourier transform infrared spectroscopy (FTIR) were developed and tested. Spectral features for CO_2 and unburnt hydrocarbons (UHC) were resolved. The time-averaged absorbance measurements showed that short-circuiting, as a function of the concentration of UHC, followed delivery ratio (Λ) at wide open throttle.

Acknowledgements

Table of Contents

List of Figures

List of Tables

Nomenclature

$\dot{E}_{e,k}$	exhaust kinetic energy flux
$\dot{H}_e$	exhaust gas enthalpy flux
$\dot{H}_{e,ic}$	exhaust chemical enthalpy flux due to incomplete combustion
$\dot{H}_{e,s,a}$	exhaust sensible enthalpy entering through atmosphere
$\dot{m}_f$	fuel mass flow rate
$\dot{Q}_w$	heat transfer rate to combustion chamber wall
$\dot{Q}_{c,e}$	heat flux radiated from exhaust system
$\dot{Q}_{c,e}$	heat rejection rate to coolant in exhaust ports
$\dot{Q}_{cool}$	heat rejection rate to cooling
$\dot{Q}_{misc}$	sum of remaining energy fluxes and transfers
η_{ch}	charging efficiency
$\eta_{f,i}$	ideal fuel conversion efficiency
η_{fb}	brake fuel conversion efficiency
η_f	fuel conversion efficiency
η_m	mechanical efficiency
η_{tr}	trapping efficiency
γ	ratio of specific heats
Λ	delivery ratio
μ	mean
σ	standard deviation
τ	torque
$\theta_{\tilde{\nu}}$	phase angle
$\tilde{\nu}$	wavelength
AC	alternating current
ADC	analog to digital converter
AKI	antiknock index
ATDC	after top dead-center
B$'$	phase-uncorrected spectrum
BDC	bottom dead-center
BMEP	brake mean effective pressure
BSFC	brake specific fuel consumption
BTDC	before top dead-center
B	true spectrum
CA$_{50\%}$	crank angle for 50% consumption of intake charge by mass

CAD	crank angle degrees
CI	compression ignition
COTS	commercial off the shelf
CoV	coefficient of variance
C	drivetrain friction slope coefficient
DC	direct current
DFT	discrete Fourier transform
ECU	engine control unit
EFI	electronic fuel injection
FFT	fast Fourier transform
FMEP	friction mean effective pressure
FTIR	Fourier transform infrared spectroscopy
FWHH	full-width half-height
F	force
$GC-MS$	gas chromatography - mass spectrometry
$GC-TCD$	gas chromatography - thermal conductivity detector
GC	gas chromatography
HeNe	helium neon
ICE	internal combustion engine
IMEP	indicated mean effective pressure
IRF	instrument response function
ISR	intelligence, surveillance and reconnaissance
L	stroke
m_f	mass of fuel
MCT	mercury cadmium telluride
MEP	mean effective pressure
$mid-IR$	mid-wavelength infrared
n_R	engine cycles per power cycle
N	engine speed
ON	octane number
OPD	optical path difference
$P-V$	pressure-volume
P_b	brake power
P_i	indicated power
p_i	indicated cylinder pressure
$P_{drivetrain}$	power lost to dynamometer drivetrain
P_{pf}	piston friction power

P_{tf}	total friction power
PID	proportional-integral-derivitive
PMEP	pumping mean effective pressure
PRF	primary reference fuel
PT	part throttle
PWM	pulse width modulation
Q_{LHV}	lower heating value of fuel
r_c	compression ratio
R_{sc}	short circuiting ratio
RPA	remotely piloted aircraft
RPM	revolutions per minute
R	universal gas constant
r	radial distance
SA	cylinder surface area
SI	spark ignition
SNR	signal to noise ratio
TDC	top dead center
TFMEP	total friction mean effective pressure
TTL	transistor to transistor logic
t	time
UAS	unmanned aerial system
UHC	unburnt hydrocarbons
USAF	United States Air Force
V_d	displaced volume
WOT	wide open throttle
X	molar concentration
ZPD	point of zero path difference

EXHAUST COMPOSITION IN A SMALL INTERNAL
COMBUSTION ENGINE USING FTIR SPECTROSCOPY

I. Introduction

This thesis documents the research, experimental setup, results, and conclusions related the study of small two-stroke internal combustion engines. The purpose of this research was to develop understanding of the operation of engines between 28 cm^3 and 85 cm^3 displacement. These engines exist in a size class where little empirical data is available on the performance, efficiency, and scaling trends of engines of similar size. This size class is ideal for the power requirements of current small remotely piloted aircraft (RPA). Better understanding of the performance of these engines will lead to increases in capability and military utility of current and future RPA platforms.

1.1 Background

The internal combustion engine (ICE) operates by converting potential energy in combustible fuel to usable work. This ability can be characterized and quantified by an engine's fuel conversion efficiency. An engine's size determines many of the parameters that affect its operation. An engine of smaller displacement will have reduced mass, but also reduced power and fuel conversion efficiency. In the realm of aerospace propulsion, specific power, that is the engine mass versus power produced, is an important parameter used to influence the design of a vehicle with mission specific capabilities. There exists a need to understand and characterize losses which impact the efficiency or small engines. Models have been developed previously to predict engine performance and efficiency for engines with larger displacements; however,

1

accurate models for engines below 100 cm^3 do not exist or are insufficient for full analysis and simulation of the engines. Development of improved models for small ICEs will drive higher performance RPA applications through efficient and optimized power plant solutions, directly supporting the interests of the United States Air Force (USAF). This work seeks to collect data quantifying the operation of these small engines to support the development of cohesive operation and performance models.

The demand for and development of small RPA platforms has outpaced the development of propulsion systems for these platforms. Typically, small RPA use small two-stroke cycle ICEs that are commercially available off the shelf. These engines are simple in design and and have low performance and are typically derived from small power equipment of model aircraft applications. The benefits of using commercial systems is their high availability and low cost. System reliability and overall performance are low and suffer at higher altitudes typical of modern missions, limiting military utility of the platform [29].

1.1.1 Case Study: Scan Eagle UAS.

The Scan Eagle is a small, group II unmanned aerial system (UAS) currently employed by the US military for light reconnaissance. Group II aircraft have masses between 21 and 55 pounds and typically operate at speeds below 250 knots and altitudes below 3500 ft. The Scan Eagle aircraft was originally envisioned as a long endurance, low altitude platform for commercial fisherman to track schools of oceanic tuna fish. Its military application was quickly realized after the September 11th terror attacks and it has become popular as a low cost intelligence, surveillance and reconnaissance (ISR) platform. Figure 1.1 shows a view of the flying wing planform and the pusher engine configuration ready for catapult launch. The aircraft uses a two-stroke, 3W-28i 28 cm^3 ICE, one of the three engines studied in this research

effort, and has a manufacturer rated endurance of 20 hours [13]. The absence of pilots in small UAS removes limits on endurance imposed by human factors in manned aircraft. A reduction of fuel consumed by engines used in these applications could accommodate endurances that are significantly higher than what is available today. Reduced fuel consumption enables more time on station, more range, and less ground handling time through fewer missions, improving effectiveness of the system as whole. Fuel injection has been shown to provide a significant reduction in fuel consumption, so the test and quantification of a fuel injection system applicable to an engine of similar size and construction is an important step to meeting increased endurance goals.

Figure 1.1. Scan Eagle aircraft on launcher in Iraq [28].

1.2 Research Problem Description

Figure 1.2, modified from Heywood [9], shows how fuel energy takes different routes through an ICE. This figure is notional but shows the complex interactions between the different forms of energy as they travel through an engine. It is important to consider each of these energy pathways when analyzing performance and losses in ICE. Improved determination of losses does not involve discovering new forms of

3

losses, but improving the measurement of and accounting for the energy pathways shown in this figure.
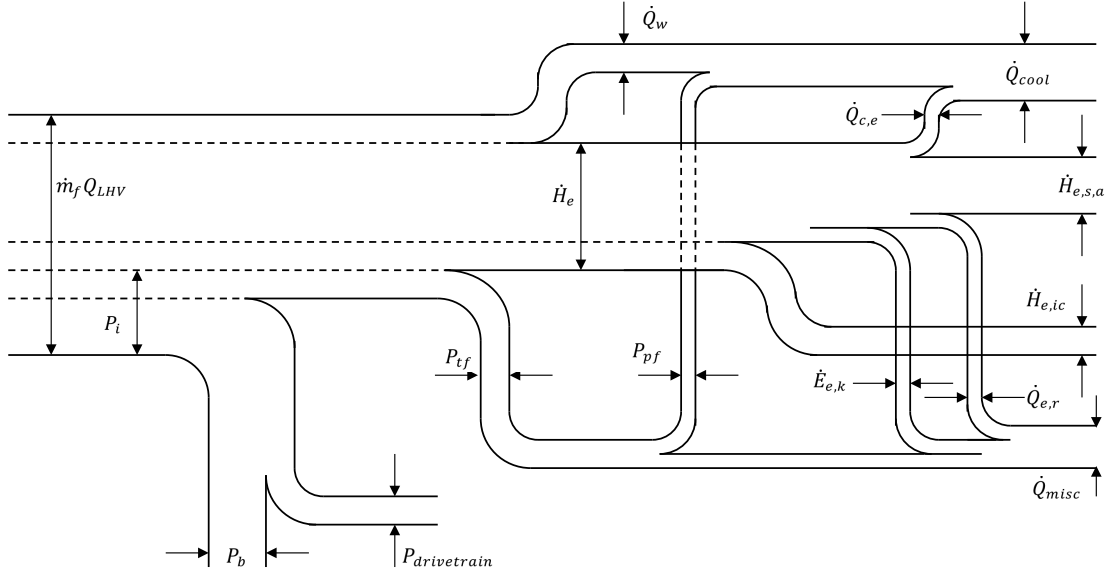
Figure 1.2. Diagram showing pathways taken by energy through the engine (modified from Heywood [9]).

Each of the arrows on this figure represents a possible location to measure these energy pathways. Brake power is the useful power output of an engine and is represented on the figure as P_b. In the test setup used here, brake power is further split into power lost to dynamometer drivetrain ($P_{drivetrain}$), which is a parasitic power loss in the test setup between the engine and measurement location. This energy pathway is not representative of anything in a real application and must be quantified through testing of the experimental setup so that it does not unduly affect the measured power and performance of the engine. The rest of the energy in the engine is split and recombined to ultimately be released as heat rejection rate to cooling ($\dot{Q}_{cool}$), exhaust sensible enthalpy entering through atmosphere ($\dot{H}_{e,s,a}$), exhaust chemical enthalpy flux due to incomplete combustion ($\dot{H}_{e,ic}$), and the sum of remaining energy fluxes and transfers ($\dot{Q}_{misc}$). Some of these states can be measured easily while others

prove more of a challenge.

Large gaps in understanding exist in the magnitude of exhaust gas enthalpy flux ($\dot{\text{H}}_e$) and its components. The exhaust gas enthalpy flux is one of the largest energy pathways in an engine, yet measurements that attempt to quantify its magnitude or components are difficult to obtain. Internal combustion engines have hot exhaust gasses which contribute to this enthalpy flux, as well as the energy retained in incomplete combustion products. Two-stroke engines have the additional penalty of short-circuiting, where fresh charge is sent directly into the exhaust without combusting in the cylinder. Several diagnostic techniques exist that have the potential to collect quantitative information on these energy pathways, but have not been implemented for small, two-stroke ICE. The quantification of the chemical species and temperatures present in the exhaust stream through analytical techniques is critical to the development of proper models that seek to tie together each of the energy pathways in an engine.

1.3   Research Objectives

The following research objectives were posed at the outset of this research effort to guide and scope the work performed. This effort builds upon previous works that started investigations into the fundamental processes and principals that internal combustion engines rely on for operation. The research focused on the following objectives:

1. Quantify the parasitic losses on engine performance due to drivetrain friction on the small engine research bench and develop a correction for collected data.

2. Convert a 55 cm^3 two-stroke engine to electronic fuel injection, quantify performance, and compare to the performance of the carbureted configuration.

3. Develop both time-averaged and crank-angle resolved quantifications of exhaust gas emissions using Fourier transform infrared spectroscopy.

1.4 Overview of Subsequent Chapters

Chapter I provides background information on the purpose and motivation behind the work documented in this thesis. Chapter II contains an overview of the literature consulted by the author during this work pertaining to small two-stroke ICE as well as a background on the science and application of Fourier transform infrared spectroscopy (FTIR) as used in this application. Chapter IV presents the findings and analyses of the experimental efforts undertaken to meet the research objectives posed in Section 1.3. Chapter V provides an overview and summary of the work performed as well as suggestions for future work.

II. Literature Review

This chapter contains a review of the literature pertinent to this research effort. The information presented here is intended to reinforce two-stroke engine operating concepts as well as to provide a background for the FTIR spectroscopy measurement that comprises a large portion of this work.

2.1   The Internal Combustion Engine

The ICE is a machine that functions to extract mechanical energy from chemical energy stored in fuel. The basic operation of an engine relies on the combustion of fuel with atmospheric air. Combustion occurs during a repeating process inside of the engine. A wide range of engine designs and cycles can be considered internal combustion engines but the scope of this work focuses on the reciprocating engine.

Reciprocating engines are typically referred to by the thermodynamic cycle employed; the Otto cycle or the Diesel cycle. These engines rely on a reciprocating piston inside of a cylinder to provide a moving surface for the high temperature and pressure combustion products to do work against. Figure 2.1 shows a pressure-volume (P-V) diagram of an Otto cycle engine, simulated by an ideal air-standard cycle analysis. The process proceeds clockwise around the curve and the enclosed area represents the work done on each cycle. The P-V diagram shows shows the isentropic compression, instantaneous heat addition, isentropic expansion and, instantaneous heat rejection phases of the idealized Otto cycle, which are simple approximations of the real processes in the engine.
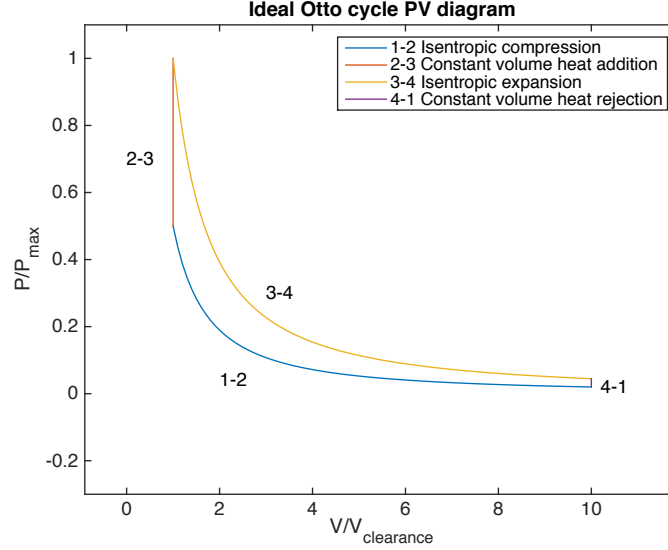
Figure 2.1. A P-V diagram for an air standard Otto cycle engine with $R_c = 10$.

The efficiency of the ideal Otto cycle can be derived using the assumptions mentioned previously. Through algebraic manipulation, it can be shown that the ideal fuel conversion efficiency ($\eta_{f,i}$) is a function of only the compression ratio (r_c) and the ratio of specific heats (γ), as shown in Equation 2.1.

$$\eta_{\mathbf{f,i}} = 1 - \frac{1}{r_c^{\gamma-1}} \tag{2.1}$$

The i subscript denotes that this is the ideal fuel conversion efficiency. Any real engine of a given compression ratio will never meet the ideal fuel conversion efficiency due to losses present in the system. The measurement and understanding of the losses present in a real engine is crucial to understanding why and how performance falls short of the idealized model. This knowledge enables new designs and technologies that improve performance and efficiency while reducing emissions to meet modern requirements.

2.1.1 Engine Cycles and Scavenging.

Internal combustion engines typically operate on either a two-stroke or four-stroke cycle. Both cycles share similar characteristics of operation; there is an intake phase, a compression phase, combustion and expansion phase, and an exhaust phase. A four-stroke engine divides each of these four phases into four separate upward or downward strokes of the piston, which requires two revolutions of the engine. Two piston strokes are devoted to promoting gas exchange and accomplish no useful work. Four-stroke engines are popular due to their low emissions and fuel efficient operation. They do incur a weight penalty due to the required valve train to control the gas exchange process and the additional engine cycle required for gas exchange, which requires a larger engine to produce equivalent power.

A two-stroke engine accomplishes the four phases of operation in only one revolution of the engine. Unlike the four-stroke engine, there is little dedicated time in the cycle for gas exchange so this process happens dynamically and rapidly, with the fresh intake charge displacing the the combustion products. Scavenging refers to the gas exchange process of a two-stroke engine; for scavenging to occur, both intake and exhaust ports must be open at the same time. Figure 2.2 compares the gas exchange processes of four-stroke engines and two-stroke engines. In a simple four-stroke engine, the intake and exhaust portions of the cycle each have 180 independent crank angle degrees to draw in fresh charge and force out exhaust products, respectively. The two-stroke engine opens its ports symmetrically around bottom dead-center (BDC). The exhaust port typically opens earlier than the intake port to allow any remaining excess pressure from combustion to escape into the exhaust. The four-stroke engine has a longer duration for gas exchange combined with dedicated strokes for both intake and exhaust for a positive displacement process that outperforms dynamic scavenging in two-stroke engines. The two-stroke engine will always

have reduced scavenging performance compared to the four-stroke engine.
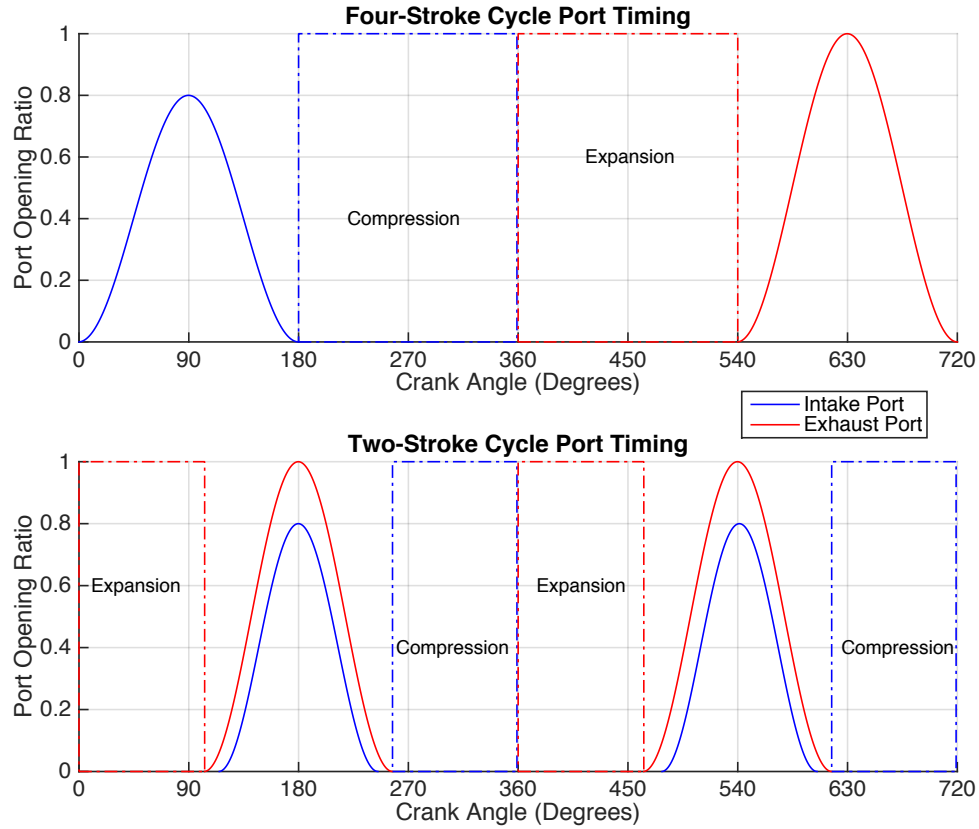
Figure 2.2. A comparison of four-stroke and two-stroke cycle gas exchange over two engine revolutions.

Multiple scavenging designs exist for two-stroke engines; they can be broadly divided into crankcase scavenged and uniflow designs. Uniflow designs are popular in larger engines and include cam actuated valves to open the exhaust ports. The small, single cylinder two-stroke engines of interest in this work rely on crankcase scavenging for gas exchange. A crankcase scavenged engine draws the intake charge into the crankcase using the motion of the piston. As the piston moves toward top dead center (TDC) and the volume of the crankcase is expands by the displaced volume and fresh charge is drawn in to the the crankcase. A flexible reed valve seals the intake charge

inside the crankcase as the piston moves back towards BDC. As the piston uncovers the intake ports, the pressurized intake charge in the crankcase is rapidly transferred into the the cylinder. This intake charge displaces the combustion products from the previous cycle, which exit through the exhaust port. As the piston moves back up towards TDC, the intake charge is compressed and combusted, completing the cycle. Cross and loop style crankcase scavenged designs as well as a uniflow scavenged design can be seen in Figure 2.3.
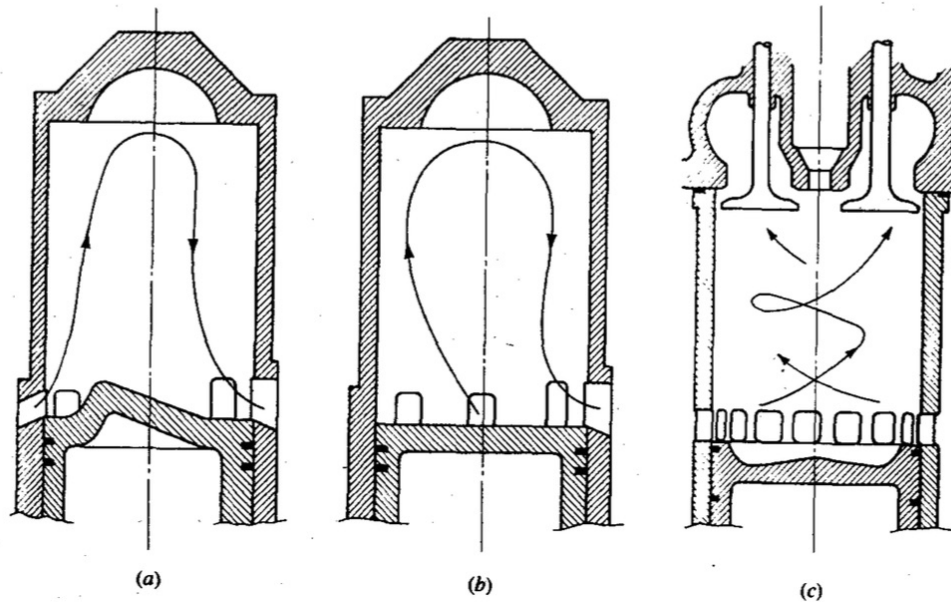
Figure 2.3. Cross scavenged (a), loop scavenged (b), and uniflow scavenged (c) two-stroke engines [9].

2.1.2 Performance of Two-Stroke Engines.

To understand engine performance, it is desired to recast engine performance parameters into values that can be directly compared between engines without having to account for differences in engine size. The typical parameter used for this type of comparison in engines is the mean effective pressure (MEP), which is defined in

11

Equation 2.2 with respect to brake power (P_b) [9].

$$\mathbf{BMEP} = \frac{\mathbf{P_b n_R}}{\mathbf{V_d N}} \tag{2.2}$$

where n_R is the number of engine revolutions per cycle, V_d is displaced volume and N is engine speed. The indicated mean effective pressure (IMEP) is the mean cylinder pressure over one complete cycle and represents the maximum potential work that can be done on the piston expanding through the swept volume. Cylinder pressure is directly measured via either a spark plug pressure transducer or a flush mount pressure probe. The indicated mean effective pressure is calculated numerically according to Equation 2.3.

$$\mathbf{IMEP} = \frac{\sum_{k=1}^{n} p_{i,k}}{n} \tag{2.3}$$

where p_i is indicated cylinder pressure. Finally, friction mean effective pressure (FMEP) can be calculated from 2.4 [4].

$$\mathbf{FMEP} = \mathbf{IMEP} - (\mathbf{BMEP} + \mathbf{PMEP}) \tag{2.4}$$

Therefore, FMEP represents the work lost due to mechanical friction in the engine and pumping mean effective pressure (PMEP) represents pumping losses in the intake system. The PMEP is actually higher at higher throttle settings, which is why the most efficient point for a two-stroke is often at throttled conditions [10]. With these equations, FMEP can be calculated using brake power from the dynamometer and in-cylinder pressure measurements. The losses due to PMEP are functionally similar to FMEP in that they both reduce the power output of the engine. The total friction mean effective pressure (TFMEP) in Equation 2.5 includes PMEP.

$$\mathbf{TFMEP} = \mathbf{IMEP} - \mathbf{BMEP} \tag{2.5}$$

Finally mechanical efficiency is defined as the ratio of brake mean effective pressure (BMEP) and IMEP in Equation 2.6 [9].

$$\eta_m = \frac{BMEP}{IMEP}$$ (2.6)

Two more terms can be used to understand an engine's ability to convert energy from fuel. An engine's brake specific fuel consumption (BSFC) is the amount of fuel burned to produce a unit power for a unit of time, typically an hour, and is defined in Equation 2.7 [9]. It is useful when comparing engines of different sizes since it can be calculated easily from experimental data.

$$BSFC = \frac{\dot{m}_f}{P_b}$$ (2.7)

where $\dot{m}_f$ is fuel mass flow rate. Finally, fuel conversion efficiency (η_f) is the ratio of power produced to fuel energy consumed by the engine and is defined in Equation 2.8 [9].

$$\eta_f = \frac{P_b}{\dot{m}_f Q_{LHV}}$$ (2.8)

where Q_{LHV} is the lower heating value of fuel.

The comparison of engines of different sizes will lead to issues with operating ranges that may not overlap. Engine rotational speed decreases as an engine increases in displacement, so it is important to define a term that bridges the gap between displacement of different engines to measure speed. Mean piston speed is the average speed that the piston travels in the cylinder over a cycle and is defined in Equation 2.9.

$$\bar{S}_p = 2LN$$ (2.9)

There are several parameters that are important to quantify the gas exchange

process in two-stroke engines. The delivery ratio (Λ), compares the mass of fresh charge delivered to the mass required for an ideal charging process and is defined in Equation 2.10.

$$\Lambda = \frac{\text{mass of fresh charge delivered}}{m_0} \tag{2.10}$$

where m_0 is the reference mass of an ideal charging process; that is the mass of ambient air that would fill the engine's displacement. The reference mass is assumed to have the same mass of fuel by volume as the fresh charge so any fuel related terms cancel out leaving only air in the numerator and denominator. In practice, the delivery ratio can have a value greater than one. This occurs whenever the engine draws more intake charge during a stroke than the displaced volume would hold, and leads to a situation known as short circuiting where some intake charge will be wasted and pass directly through to the exhaust.

The charging efficiency (η_{ch}) indicates how effectively the cylinder volume has been filled with fresh charge and is shown in Equation 2.11.

$$\eta_{\textbf{ch}} = \frac{\text{mass of fresh charge retained}}{m_0} \tag{2.11}$$

A charging efficiency of unity would indicate perfect volumetric efficiency. The scavenging efficiency, η_{sc}, indicates the extent that exhaust gasses have been replaced with fresh charge compared to total mass of the cylinder charge (m), and is defined in Equation 2.12.

$$\eta_{\textbf{sc}} = \frac{\text{mass of fresh charge retained}}{m} \tag{2.12}$$

The trapping efficiency (η_{tr}) indicates the extent the fresh charge is retained at the end of the gas exchange process and is defined in Equation 2.13.

$$\eta_{\textbf{tr}} = \frac{\text{mass of fresh charge trapped}}{\text{mass of fresh charge delivered}} \tag{2.13}$$

Finally, the short circuiting ratio (R_{sc}) is defined as the ratio of mass of fresh charge lost to the mass of fresh charge delivered in Equation 2.14.

$$\mathbf{R_{sc}} = \frac{\text{mass of fresh charge lost}}{\text{mass of fresh charge delivered}} = 1 - \eta_{tr} \tag{2.14}$$

It should be noted that all of the terms pertaining to two-stroke scavenging, with the exception of trapping efficiency, are instantaneous and can be computed for any point in the cycle [10]. In practice, it may be simpler to measure the rates of mass flow into and out of the engine to better determine an average value for each of these parameters at a given engine condition.

Engine operability can be assed by calculating the coefficient of variance (CoV) for IMEP. The CoV is a mathematical term that can be used to describe any statistical process. It is defined in Equation 2.15 as the ratio of the standard deviation (σ) over the mean (μ).

$$\mathbf{CoV} = \frac{\sigma}{\mu} \tag{2.15}$$

Determination of combustion phasing is important for optimizing power output. Combustion must initiate sufficiently early so that peak pressure occurs just after TDC. The crank angle for 50% consumption of intake charge by mass ($\text{CA}_{50\%}$) is useful for determining optimal spark timing as its value is consistent across all speed and load settings. Its value can be estimated through in-cylinder pressure measurements. Typical values for this parameter are between $8°$ to $10°$ after top dead-center (ATDC) [9].

2.1.3   Short Circuiting in Two-Stroke Engines.

Short circuiting is an issue that significantly affects crankcase scavenged engines. Short circuiting occurs when fresh intake charge passes through the cylinder while

both the intake ports and exhaust ports are open, near BDC. The intake charge that is lost to short circuiting is not burned in the cylinder and does not contribute to the useful work produced by the engine. Short circuiting represents a significant loss pathway for two-stroke engines so it is vital that this phenomena be understood and analyzed to reduce losses.

The scavenging performance of a two-stroke engine depends on the design of the engine and significant work has gone into understanding the effects of different designs. Sher [24] has compiled a summary of no fewer than 17 articles on experimental determination of scavenging efficiency. Represented in these articles are methods to quantify scavenging effects through analysis of CO, CO_2 and O_2. Hori et al. [11] measured scavenging in a two-stroke, loop scavenged diesel engine by installing valves in the head that would extract small samples of gas for later analysis. The results of the gas analysis were used to estimate trapping ratio and scavenging efficiency with respect to delivery ratio. The results gathered were plotted against the perfect mixing and perfect displacement models to determine the effect of delivery ratio on trapping efficiency and are shown in Figure 2.4. The perfect mixing model assumes that the the combustion gases in the cylinder after the scavenging process are instantaneously mixed with the intake charge based on the delivery ratio. The perfect scavenging assumes that there is no mixing and the intake charge displaces the combustion products. Any real engine will have some mixing while the combustion products are displaced so these models represent the upper and lower bounds of scavenging performance.

Perfect scavenging

Scavenging efficiency η_s
Trapping efficiency η_{tr}

1.0

0.8

0.6

0.4

$\eta_s = 1 - e^{-l_z}$

$\eta_s = l_z$

Eng. speed	Water temp.
800 r.p.m.	75°C
1200 "	75°C
1200 "	50°C
1600 "	75°C

Perfect mixing

$\eta_{tr} = \frac{1}{l_z}$

$\eta_{tr} = \frac{1}{l_z}(1 - e^{-l_z})$

0   1   2   3

Delivery ratio $l_z = l_0/C_r$
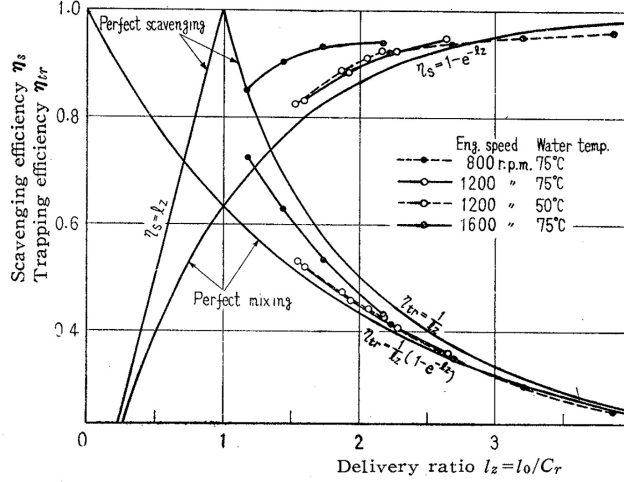
Figure 2.4. Scavenging and trapping efficiency versus delivery ratio as collected by Hori compared to perfect mixing and perfect displacement models [11].

Ohigashi and Hamamoto [18] used a fast acting valve in the combustion chamber of an engine to extract gases for analysis. Notably these measurements were performed in 123 cm^3 and 50 cm^3 two-stroke, spark ignition engines . Also detailed are works using tracers such as monomethylamine (CH_3NH_2), n-butane (C_4H_{10}), CO and other compounds. The findings and methods developed in these works are valuable and establish some of the best practices for the determination of scavenging performance in two-stroke engines. In every case, the data collected were from engines larger than those currently under investigation. Comprehension of the advantages and disadvantages of these different experimental methods is important for proper design of experiments related to scavenging.

The results of the experimental investigations drive the creation and validation of scavenging models to estimate the performance of two-stroke engines under a variety of conditions. These scavenging models are able to predict the parameters defined in Equations 2.11, 2.12, 2.13 and 2.14. Heywood and Sher [10] detail many of these models and compares them using the "β test" where the models are applied to a standard engine and plotted over the gas exchange cycle, as shown in Figure 2.5 .

This graphical representation provides an excellent analysis tool for the comparison of scavenging models as well as empirical data over a simulated engine cycle.
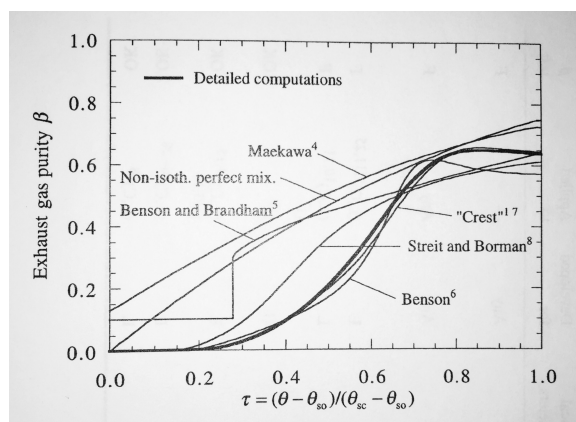
Figure 2.5. The "β test" with various scavenging models from Heywood and Sher [10].

2.1.4 Ignition and Fuel Delivery.

Internal combustion engines require the fuel-air mixture to ignite near TDC to build pressure in the combustion chamber. Precise control of this process is required to optimize combustion for maximum performance. There are two different types of ignition schemes in ICE, spark ignition (SI) and compression ignition (CI). A spark ignition engine ignites the fuel-air mixture via an electric arc across a spark plug located in the combustion chamber. The timing of the spark is controlled either mechanically or electronically and initiates the combustion event. The spark usually occurs between 35° and 10° before top dead-center (BTDC) so that the mixture has sufficient time to burn before the piston retreats and expands the volume of the cylinder. Spark ignition engines are popular for automotive, general aviation, and power equipment applications.

Fuel delivery can be controlled mechanically though a carburetor or via a fuel injection system. Electronic fuel injection is ubiquitous in medium to large SI engines due to stringent requirements on emissions and reduced fuel consumption. Carbu-

retors are still popular in small engines of less than 500 cm^3 displacement due to their affordability, simplicity, and light weight. The miniaturization of electronic fuel injection systems for small engines adds cost and complexity but has driven higher performance in these applications to meet increased requirements.

The combustion phasing of a CI engine relies on the fuel-air mixture reaching its autoignition temperature so that it combusts without the external energy input of a spark. In a premixed environment, the point at which the mixture reaches autoignition temperature can be difficult to control. Instead the fuel is injected near TDC so that it partially mixes with the intake charge and immediately combusts. The timing of the combustion event is controlled by the start of fuel injection. Compression ignition engines are commonly referred to as diesel engines and are popular in larger applications due to low fuel consumption. They typically operate on heavier fuels like diesel fuel, kerosene, and bunker oil that have low resistance to autoignition. Efficient combustion requires precisely timed injection events so CI engines employ either mechanical or electronic fuel injection systems. One notable exception are glow engines, which are very small two-stroke engines that operate at very high speeds. The heat of combustion is transferred to a fine wire that remains hot enough to auto-ignite the fuel-air mixture near top dead center. These engines share characteristics of CI and SI engine. The simplicity of glow ignition combined with a basic carburetor for fuel delivery makes glow engines popular for very small applications.

2.2   Performance and Scaling of Small ICE

In the realm of aerospace propulsion, specific power is an important measure of performance and technology in an engine. It is important to minimize the weight of the propulsion system and required fuel to maximize performance of the aircraft. Aircraft design for the last 50 years has focused on gas turbine engines for their low

mass and high performance. Gas turbine engines become impractical and inefficient when scaled to the sizes required in small UAS. Internal combustion engines are ideally suited to these applications due to their simplicity and low cost, but they are not comprehensively designed and sized for the specific mission in which they are used. Similar to gas turbine engines, the efficiency of ICE diminishes as size decreases. It is important to understand and characterize the losses that reduce efficiency. Models have been developed to predict performance and efficiency of ICE with larger displacements, but accurate models for smaller engines do not exist. The development of new performance and scaling models requires a complete understanding of the operation of engines with less than 100 cm^3 displacement. The following section documents the work done to quantify performance of engines in this size class.

2.2.1 Knock Limit Determination and Altitude Performance.

This research effort builds directly upon the work of previous students at AFIT. Wilson [29] tested the performance of a 34 cm^3 FUJI four-stroke, spark ignition engine on a dynamometer. The engine was designed to run on automotive gasoline with an antiknock index (AKI) of 87. The goal was to determine the octane number (ON) requirement for operation at conditions representative of what the engine would experience in a small aircraft. The engine was operated on a primary reference fuel (PRF) blend of n-heptane and iso-octane. The ratio of fuel components were varied to control ON. Through optimization of spark timing and fuel delivery, it was found that the octane requirements for the 34 cm^3 engine could be relaxed to the point of efficient operation without knock when running on pure n-heptane and 0 ON.

The small, two-stroke engines currently used in small UAS applications perform poorly at high altitude cruise conditions typically required of military operations. The United States Air Force has identified problems with reducing the size of UAS and the

technical difficulties of gaining acceptable performance and military utility from these platforms. Of the major points identified, engine efficiency and reliability pose the most significant challenges in the development of smaller platforms [27]. Crosbie [5] sought to test a 95 cm^3 two-stroke, spark ignition engine at various altitude conditions to better understand performance impacts of a high altitude environment . A fuel injection system was proposed as a solution to replace the carburetor. It was found that the engine, designed for operation near sea-level conditions, performed extremely poorly at altitude using the manufacturer recommended carburetor fuel delivery settings. Acceptable levels of performance that scaled with density were attainable if the carburetor was tuned for operation at a chosen altitude, however performance was sacrificed at off-design conditions. To mitigate the limitations imposed by a simple carburetor, a fuel injection system was implemented on the engine. The engine was retested with the fuel injection system. Peak power was similar to the carbureted configuration and operability was improved improved significantly off-condition, especially at higher altitudes. Fuel consumption and stability of performance as measured by CoV was also improved. Husaboe [12] continued the altitude testing on the same 95 cm^3 two-stroke engine and found that power reduced 3.5% and BSFC increased 3.5% per 300 m altitude .

These works show that control must be maintained over the fuel delivery for the engines to maintain peak performance at different altitudes. Carbureted engines are particularly sensitive to changes in altitude so optimized applications of ICE in small RPA must implement lightweight fuel injection systems to take advantage of this improved operability and efficiency. Reliance on simple, off the shelf engine and fuel delivery designs does not provide acceptable performance for current and future applications of small RPA.

2.2.2 Engine Scaling Studies.

A comprehensive set of performance models for small two-stroke engines relies on understanding how performance scales with the size chosen for an application. These models seek to capture the phenomena that influence these scaling effects. Rittenhouse [20] sought to develop understanding of how different loss mechanisms affect an engine as displacement is reduced. It was hypothesized that engines between 25 cm^3 and 250 cm^3 exist in a range where thermal losses begin to dominate engine efficiency, limiting peak fuel conversion efficiency to less than 20% in most applications [20]. A 55 cm^3, two-stroke spark ignition engine was tested on a small engine research bench developed by Ausserer et al. [2]. Additional information on the small engine research bench, as used in this work, is discussed in Section 3.1. To investigate the impact of heat rejection due to cooling, a custom engine enclosure was constructed to thermally isolate the engine and to act as a control volume. Cooling air was forced through the enclosure and the temperature difference between the inlets and outlets was taken to measure the heat transfer to the cooling airflow.

An energy balance was performed using a combination of data from the heat rejection, fuel flow, exhaust enthalpy estimates, and indicated power measurements from a flush-mounted in-cylinder pressure transducer [20]. The sum of this energy balance is shown in Figure 2.6. It should be pointed out that these different energy pathways do not sum to 100% and there remains a significant amount of energy from the fuel that is unaccounted for. The energy components for incomplete combustion, short-circuiting and exhaust enthalpy were estimates and not based on sufficient physical measurements made during testing. These estimates and models were taken from the literature and originally developed for engines 400 cm^3 and larger as outlined in Heywood and Sher [10]. Efforts need to be made to quantify incomplete combustion, short-circuiting, and exhaust enthalpy for engines in this size class to better

understand thermal losses.
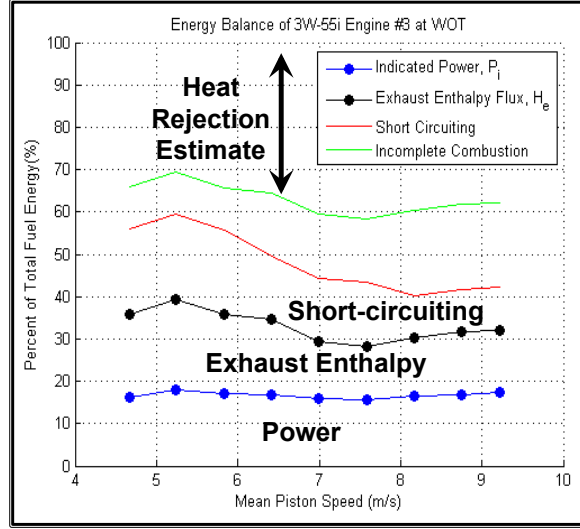
Figure 2.6. Energy balance results as a percentage of fuel energy versus speed [20]

A subsequent effort by Rowton [22] expanded the dataset originally collected by Rittenhouse to include 28 cm^3 and 85 cm^3 two-stroke engines of similar design to the 55 cm^3 used by Rittenhouse . The three engines tested were manufactured by 3W-Modellmotoren GmbH and can be considered geometrically similar insofar as possible for commercial off the shelf (COTS) engines. The operating points tested were chosen to cover the full range engine operability; from 4000 rpm to 7900 rpm. Throttle settings were 25%, 50%, 75%, and wide open throttle (WOT). The additional data collected were used to develop scaling laws for engines of similar size. Models were developed to represent brake fuel conversion efficiency (η_{fb}), total friction power (P_{tf}), and $\dot{Q}_{\text{cool}}$. These values were all normalized against the fuel energy consumed. The final scaling laws are listed in Equation 2.16, Equation 2.17 and Equation 2.18. The coefficients and trends developed by Rowton were an initial attempt in quantifying the phenomenology and performance of engines in the 28 cm^3 to 85 cm^3 size class.

$$\eta_{\text{fb}} = 21 \frac{\text{SA}}{\text{V}_{\text{d}}}^{-1.5} \tag{2.16}$$

23

$$\frac{P_f}{\dot{m}Q_{LHV}} = 1.4 \frac{SA}{V_d}^{2.5} \qquad (2.17)$$

$$\frac{Q_{cool}}{\dot{m}Q_{LHV}} = 1.8 \frac{SA}{V_d}^{-2} \qquad (2.18)$$

Rittenhouse [20] and Rowton [22] shared experimental setups and largely encountered the same difficulties and limitations. Each identified areas in which updates to test methodology and additional measurement techniques could refine and improve the scaling analysis performed. Most significant was the inability to precisely control fuel delivery; the carburetors installed on each engine could not precisely meter fuel under the varying speed and load conditions tested. Hysteresis in servo control of throttle opening prevented accurate and precise airflow metering [22] [29]. Limitations of exhaust enthalpy measurements required several assumptions on what was hypothesized to be the single largest energy pathway out of the engine. Finally, dynamic friction in the dynamometer drivetrain absorbed significant power as it was transmitted from the engine to the dynamometer, negatively affecting measured brake power output [22].

The work by Rittenhouse and Rowton both took advantage of in-cylinder pressure measurements to determine IMEP. Two types of pressure transducers were used; a flush-mount transducer located in the cylinder head and an integrated spark plug pressure transducer. Ausserer et al. [3] conducted a study of the repeatability and accuracy of these two methods of gathering in-cylinder pressure measurements using the 3W 55 cm^3 two-stroke engine. The same engine was instrumented with both transducers simultaneously and IMEP data were recorded. It was found that cycle to cycle variability in both transducers was less than 0.1% and was exceeded by the variability of the combustion process. Instrument uncertainty was low as well, contributing only 0.5% to overall uncertainty. Overall, a 4% difference in measured IMEP was observed between the two types of transducers. The close correlation between

the two transducers demonstrated that measuring spark plugs were both comparable to the stock plug in ignition performance and provided accurate measurements of IMEP in small scale engine applications. Both pressure transducers were used during experimentation conducted for this thesis so confidence in the data gathered by these measurements is high.

Other groups have investigated performance and scaling of small and micro internal combustion engines. Menon and Cadou from the University of Maryland [16] have created a small engine dynamometer and used it to measure the performance and efficiency of small two-stroke engines from 7.5 cm^3 to 0.16 cm^3 displacement. This dynamometer was used to collect performance data for these small glow-fuel engines. A dataset of manufacturer provided performance data combined with experimental data was aggregated. Scaling laws to predict estimates of power, torque and efficiency were be developed. This dataset, shown in Figure 2.7, included an extremely large range of engines, from some of the smallest available commercially available ICE to the largest shipboard diesel engines. Correlations for power developed from this dataset for two-stroke engines are shown in Equation 2.19 and thermal efficiency in Equation 2.20.
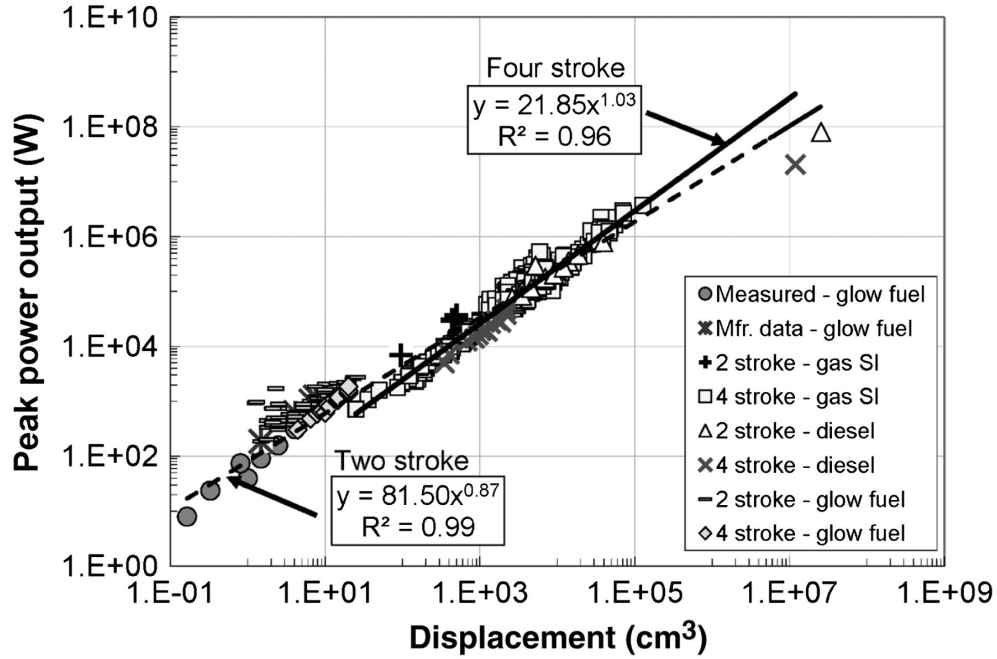
Figure 2.7. Data for power output versus displacement for nearly the entire size range of internal combustion engines [16].

$$P_b = 81.50 V_d^{0.87} \tag{2.19}$$

$$\eta_f = 14.21 V_d^{0.08}[1 - CV_d^{-2/3}] \tag{2.20}$$

where displaced volume (V_d) is given in units of cc. In Equation 2.20, the value for C depended on exhaust configuration and size of the engine. The term was ignored for larger engines with displacements above 25 cc.

The addition of the C term at very small displacements was indicative of additional phenomena that were possibly not being captured by this exponential trend. It is not clear how the C term influenced the trend and the reason why this term changed between glow engines with and without mufflers. Furthermore, glow engines rely on compression ignition and do not fully compare to the 28 cm^3, 55 cm^3, and 85 cm^3 engines targeted by this research effort. Additional testing and analysis is required to understand of the sizes relevant to this work; however, combined with performance

26

data for engines of smaller and larger displacements, a more complete picture of engine scaling effects can be seen.

Menon and Cadou [17] also investigated thermal loss pathways in small two-stroke glow engines. An apparatus was constructed that could motor the engine to determine FMEP while the engine was at operating speed and temperature. This was accomplished by running the engine to the target speed, cutting the fuel and allowing the engine to be motored by an external power source. Power lost to engine friction was determined to increase linearly with speed. A correlation was developed to predict the power loss due to internal friction of the small glow engines. As before, the engines studied exist outside the range of displacements investigated in this effort.

2.3 Fourier Transform Infrared Spectroscopy

In accordance with the research objectives, a goal of this effort is to develop both time-averaged and crank-angle resolved quantifications of exhaust gas emissions using Fourier transform infrared spectroscopy to better understand the properties of the exhaust gasses and the quality of combustion in the engine. Infrared spectroscopy is the study of the optical properties of substances in the infrared wavelength bands. A substance has a unique and identifiable infrared spectrum that results from transitions between quantized vibrational energy states of the constituent atoms in a molecule [7]. Fourier transform infrared spectroscopy has been identified as a diagnostic technique that can collect measurements on the working fluid of an internal combustion engine. This analysis capability seeks to improve understanding of the short-circuiting phenomenon in small, two-stroke engines. There are several measurements that all fall under the broad category of FTIR spectroscopy; however, they all share the ability to produce high-resolution, non-intrusive measurements of hot gasses across a range large wavelengths, simultaneously. The broadband nature of FTIR spectroscopy al-

lows spectral data corresponding to unique compounds to be gathered quickly which is ideal for the high-speed operation of ICE. The unique fingerprint of a molecule that is its infrared spectrum allows identification of a substance based on infrared spectroscopic measurements of infrared light. The following section will detail some of the scientific principals that underly FTIR spectroscopy as well as uses that are applicable to the focus of this research.

2.3.1 Beer's Law.

The Bouger-Lambert-Beer law, often referred to as simply Beer's law, is the foundation of analytical spectroscopy and states that the absorbance of any component in the sample is proportional to its concentration in the sample [7] [25]. It is stated mathematically in Equation 2.21, for the absorbance case [25].

$$\mathbf{A} = \varepsilon l x \tag{2.21}$$

where ε is the absorptivity, l is the optical path length, and x is the molar concentration of the substance. The absorptivity is a constant of the system and can either be analytically derived from Snell's law [7] or found through empirically testing the system against a known concentration. In layman's terms, Beer's law correlates the absorption of light by a substance to its concentration and state. The absorption of light at a single wavelength can be measured easily and directly correlated to the concentration and temperature of the substance which absorbs the light. Beer's law forms the foundation of FTIR spectroscopy as it is used in this research.

In practice, absorbance is found as the negative natural logarithm of the ratios of received power of light passed through the substance and reference power transmitted

through the substance.

$$\mathbf{A} = -ln\left(\frac{I}{I_0}\right) \tag{2.22}$$

It is important to know that the detected power of the light is not proportional to concentration, but is related by the natural logarithm. The reference power is typically found by passing light through the spectrometer system and measuring the received power without a sample in place.

2.3.2   Michelson Interferometer.

The key enabling technology for FTIR spectroscopy is the Michelson interferometer. As shown in Figure 2.8, a Michelson interferometer is a device that splits a beam of radiation into two paths, introduces a path difference between the two, and recombines the beams into one. Due to the wave-like properties of light, the optical path difference creates conditions where interference between the split beams will occur. The wavelengths of light that interfere constructively and destructively are a function of the optical path difference [7]. In applications of absorptive FTIR spectroscopy, the Michelson interferometer accepts light from a broadband source to create a spatially modulated light signal.
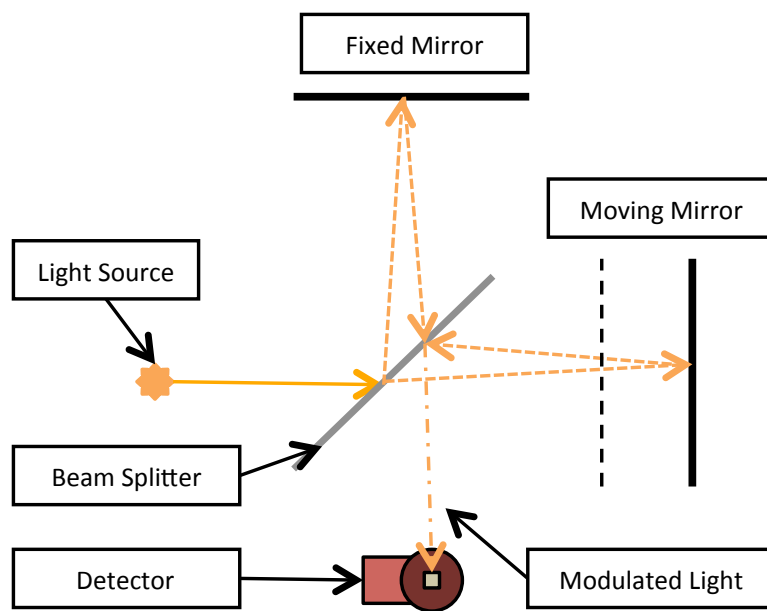
Figure 2.8. Michelson interferometer showing the source, beam splitter, two reflector mirrors, and detector.

In an FTIR spectrometer, the interferometer is used to modulate a broadband light source in such a way that it can be reconstructed later via Fourier transform. The broadband light source in an FTIR spectrometer emits a continuous, broadband beam of light that is routed into the interferometer for modulation. Tungsten alloys are commonly chosen as emitters because of their blackbody emission properties, consistent output, and long life. As the mirror moves from the centerburst and point of zero path difference (ZPD), the different wavelengths emitted by the light source will interfere constructively or destructively depending on the optical path difference (OPD) of the mirrors and wavelength. Only at the centerburst are all wavelengths of light interfering constructively. At all other mirror positions, there will be some level of destructive interference, reducing the light output by a deterministic amount. The level of interference behaves as a periodic function and will oscillate as the mirror continues to move away from the position of ZPD. This collection of light intensity information is known as an interferogram. The interferogram contains

the modulated information on all wavelengths of light emitted by the source at every mirror position. Each point on the interferogram is a cumulative measurement of every wavelength of light passed through the interferometer.

The quality of the modulated light signal leaving the interferometer depends on the precision available to track and control the motion of the mirror. The primary detector can be used to determine the centerburst with high accuracy by searching for the point of maximum power. The distance of the mirror away from the centerburst is tracked using the fringes of a monochromatic laser routed through the interferometer. As the mirror moves, the intensity of the laser light at the reference detector will follow a sinusoidal pattern as the beams interfere with eachother. Destructive interference occurs at a phase shift of 180° and an optical path difference of $\lambda/2$, where λ is the wavelength emitted by the monochromatic laser. A full cycle of interference occurs over a mirror translation of $\lambda/2$ with an OPD of λ and is repeated as the mirror continues to move. Most FTIR spectrometer instruments use a helium neon (HeNe) laser with a precise, single emission wavelength of 632.966 nm or 15,798.6 cm^{-1} to ensure easily identifiable interference fringes from interferometer [25]. The level of precision to which the emission of HeNe lasers is known and the simplicity of tracking the mirror in this method allows excellent accuracy and precision with respect to mirror position.

The Michelson interferometer is the practical application of what is commonly referred to as the Felgett Advantage [7]. The Fellgett Advantage is named after P. B. Fellgett and is based on his discovery that multiplexed signals show significant improvements in signal to noise ratio (SNR) for a given measurement, when compared to otherwise identical serial measurement experiments. It can be stated that spectrum measured on an FTIR spectrometer will have an improvement in SNR of $\sqrt{M}$ over the identical spectrum measured on a traditional grating spectrometer. For an equal

number of samples collected, M, on both instruments [7]. The FTIR spectrometer will always have an SNR advantage over a grating spectrometer for a given measurement time or quantity. Conversely, for a given SNR the FTIR spectrometer will be able to perform the measurement in fewer samples.

2.3.3   Discrete Fourier Transforms.

The discrete Fourier transform (DFT) is the application of the Fourier transform to a discrete domain. A full mathematical explanation and derivation is available in most engineering mathematics texts; however, a few points should be noted. The name Fourier transform infrared spectroscopy underlies the importance of the Fourier transform to the experiment. The discrete Fourier transform is used to extract the spectral information encoded in the interferogram. Establishing the limits of the transformed frequency information is important in a DFT since not all of the information is captured in the discrete samples. The maximum frequency that can be resolved is limited by the requirement of having two samples per cycle of the periodic function, according to the Nyquist limit [30]. The maximum resolved frequency, or minimum resolved wavelength, is dependent on the number of samples taken. Similarly, the resolution of frequencies resolved is inversely proportional to the physical length of the OPD away from the centerburst. A desired resolution of 2 cm^{-1} will require an OPD of $1/(2cm^{-1})$ or a 0.5 cm OPD. The units of wavenumber (cm^{-1}) simplify understanding of the physical dimensions required for these operations.

The fast Fourier transform (FFT) is an implementation of the DFT optimized for binary computer systems. It is a subset of the DFT and is most commonly used today in signal processing because it reduces the amount of computation needed to perform a Fourier transform in almost all cases. The optimizations made take advantage of the traits of a binary number system so some limitations are imposed. The FFT

relies on periodic, equally spaced points in the sample. In FTIR spectrometry applications, the requirement of equal spacing is met by careful control of mirror position, as monitored by the HeNe laser interference fringes. Certain strategies of FTIR spectroscopy may produce samples that are not evenly spaced within the interferogram. In this case, it is required that consistent spacing be enforced using some form of interpolation between points. With any interpolation scheme, data may be lost in the approximation and care must be taken to ensure that the interpolation process does not introduce spurious data into the measurement. The FFT also requires a sample size of 2^n to perform the calculations. The algorithm will not work with samples numbering fewer than the nearest power of two, so the solution for non-conforming data sets is to pad the data with zeros. Zero padding contains no frequency or phase information; however, the SNR of the output spectrum will be less than that of a full dataset because less signal is available. Measurements in the real world seldom conform strictly to the length requirements, so zero-padding is often automatically applied by current FFT software algorithms to ensure compatibility.

2.3.3.1 Apodization.

The interferogram that is produced by sampling the modulated light after exiting the Michelson Interferometer is what is known as a sinc function. The sinc function is the Fourier transform of a boxcar function, $D(\delta)$ [7]. The sinc function is shown in Figure 2.9 and mathematically defined in Equation 2.23. In a purely theoretical sense, no information is lost across a continuous Fourier transform of infinite length. In reality, a continuous signal cannot be completely captured by a digital system so it is approximated by a finite collection of discrete points. In this example, the DFT is performed on the sinc function to return to the boxcar function. Ringing in the sidelobes is apparent, indicating the loss of information in the discretization of the

continuous periodic function, as shown in Figure 2.10.

$$\textbf{sinc(x)} = \frac{\textbf{sin}(\pi \textbf{x})}{\pi \textbf{x}} \tag{2.23}$$
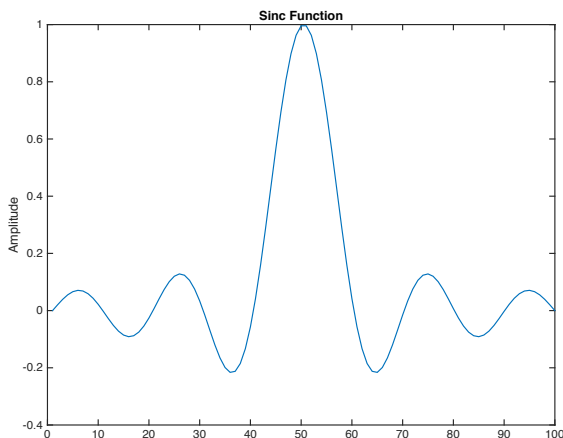
Figure 2.9. **Fourier transform of the boxcar function** $\mathbf{D}(\delta)$.
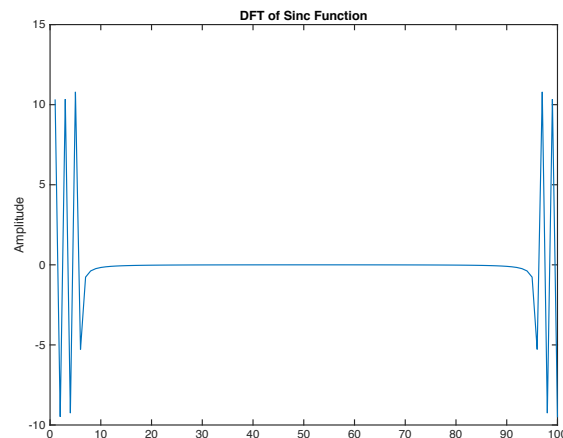
Figure 2.10. **Fourier transform of the sinc function with ringing in the side-lobes.**

The solution to the problem of ringing and side lobes what is known as apodization. It is a method of modifying the discrete signal to reduce the undesirable characteristics of the DFT by suppressing oscillations in the transformed signal [7]. The particulars of apodization can vary greatly but any function that has a value of unity at ZPD and decreases as the function moves out from center can be used an apodization function. Apodization functions can have drawbacks, namely in the reduction of data fidelity that is returned by the Fourier transform. Typically, the full-width half-height (FWHH) is reduced and peaks will be widened. It is up to the user to determine the proper tradeoff between the different apodization functions available when processing data.

The Norton-Beer apodization function was developed through an analysis of many different apodization functions used in FTIR spectroscopy [7]. Variants of the func-

tion are widely used today for consistency between different measurements. The general form of the Norton-Beer apodization function is shown in Equation 2.24 and the coefficients for the weak, medium, and strong functions are listed in Table 2.1. Selection of the proper coefficients is dependent on the details of the spectra to be measured. The Norton-Beer strong apodization function was used in this work for both step-scan and linear-scan measurements.

$$\mathbf{A}(\delta) = \sum_{i=0}^{n} \mathbf{C_i} \left[\mathbf{1} - \left(\frac{\delta}{\mathbf{\Delta}} \right) \right]^{\mathbf{i}} \tag{2.24}$$

Table 2.1. Norton-Beer apodization coefficients [7].

	C_0	C_1	C_2	C_3
Weak	0.384093	−0.087577	0.703484	0
Medium	0.152442	−0.136176	0.983734	0
Strong	0.045335	0	0.554883	0.399782

2.3.3.2   Phase Correction.

The Fourier transform of the interferogram is a vector of complex values. It can be represented as a magnitude and phase at every wavelength in the spectral range. The magnitude of the complex value represents the majority of the spectral information at any given point in the spectrum. The phase information, however, contains additional spectral information that is relevant to the measurement. A process for correcting the magnitude of phase information was developed and is known as the Mertz phase correction. The output of the phase correction is known as the true spectrum (B) [7]. The equation used to determine the phase angle ($\theta_{\tilde{\nu}}$) is given in Equation 2.25 and the equation used to calculate the B at a wavelength ($\tilde{\nu}$) from the $\theta_{\tilde{\nu}}$ and phase-

uncorrected spectrum (B') is given in Equation 2.26.

$$\theta_{\tilde{\nu}} = \arctan\frac{\mathbf{Im}(\tilde{\nu})}{\mathbf{Re}(\tilde{\nu})} \tag{2.25}$$

$$\mathbf{B}_{\tilde{\nu}} = \mathbf{B}'(\tilde{\nu})\mathbf{e}^{-\mathbf{i}\theta_{\tilde{\nu}}} = \mathbf{Re}(\tilde{\nu})\mathbf{cos}\theta_{\tilde{\nu}} + \mathbf{Im}(\tilde{\nu})\mathbf{sin}\theta_{\tilde{\nu}} \tag{2.26}$$

2.3.4 Absorbance Spectra.

The final result of the apodized and Fourier transformed interferogram is what is known as a single beam transmission spectrum. This single measurement is not useful on its own for revealing concentration information as it contains information pertaining specifically to the optical transmission properties of the experimental setup. To isolate the sample from the effects of the optical components, it is required to obtain the instrument response function (IRF). The IRF is obtained by making a scan the background spectrum, which is taken with the sample removed from the optical path [25]. The absorbance of the sample is calculated using Equation 2.22 and is the final product of the FTIR spectrometer. Figure 2.11, Figure 2.12 and Figure 2.13 show the instrument response function, the sample single line spectrum and the sample absorbance for atmospheric CO_2 and H_2O, respectively collected from the experimental setup of this project.
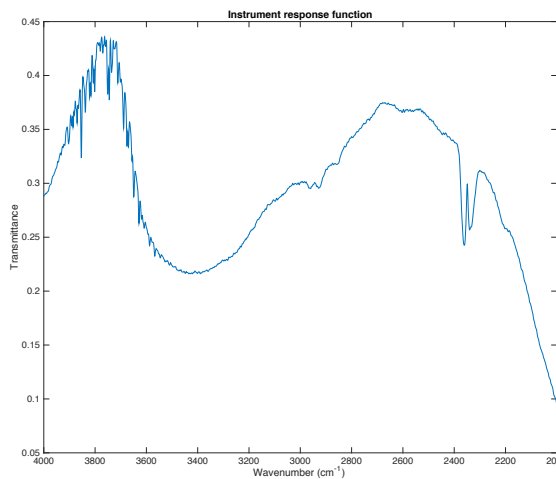
Figure 2.11. Instrument response function for a nitrogen purged sample.
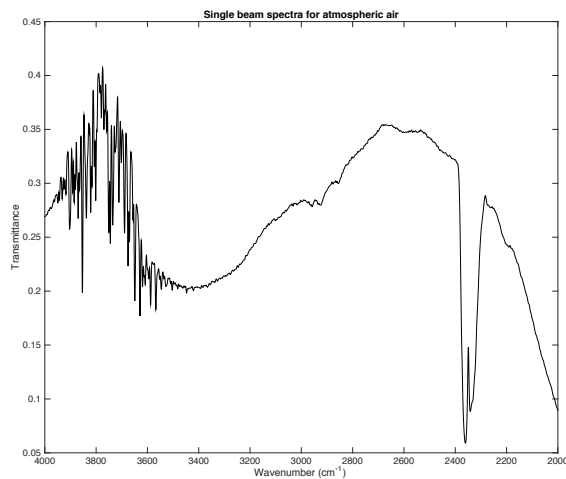
Figure 2.12. Single line spectrum for atmospheric air.
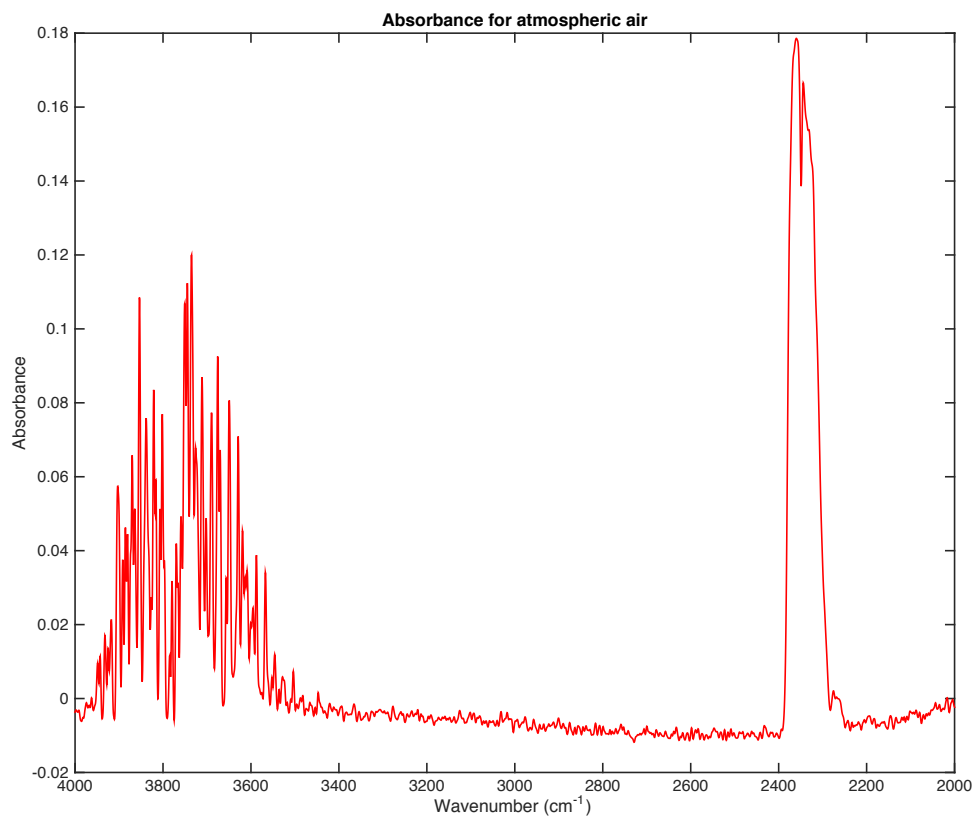
Figure 2.13. Absorbance spectra for air with absorbance bands for H_2O and CO_2.

2.4 FTIR Spectroscopy and its Uses

The versatility of FTIR spectroscopy has made it useful for many analytical chemistry applications. The ability of FTIR spectroscopy to measure concentrations of several species simultaneously has provided particularly versatile to combustion diagnostics in modern engines. Widespread application of FTIR spectroscopy has been enabled by the advancement of computer hardware and detector technology. A search of the literature shows published documents on the subject back to the 1970s and earlier. Most experimental efforts for ICE pertain to automotive applications where exhaust emissions are the focus. These measurements all diverted a small portion of exhaust flow to a long path-length, heated gas cells with optical paths between 2 m and 20 m in length [6] [8]. The goal was to quantify levels of emission controlled substances like aromatic unburnt hydrocarbons (UHC), CO, and other volatile organic compounds. The ability to quickly process the spectra and provide concentrations allowed these measurements to take place in near real-time and sometimes while a vehicle is in motion. This rapid insight enabled by these measurements have proved invaluable to understanding engine emissions under real world conditions.

2.4.1 Step-Scan FTIR Spectroscopy.

Typical applications of FTIR spectroscopy use a rapidly scanning mirror that traverses its entire OPD at a constant or near constant velocity. The interference fringes produced by the HeNe laser are used both to track the mirror as it moves and trigger sampling of the detector at a constant interval. The mirror requires a finite time to traverse the physical distance required so the chemical process being studied must be in a steady state condition. The steady state requirement of linear scan FTIR spectroscopy poses a challenge for fast processes that exhibit significant change over time. A method of operation called step-scan FTIR spectroscopy provides

an alternate solution to linear scan tests. For a high speed, repeatable process, a step-scan interferometer can be used to make multiple measurements of the repeated process at different points in time.

Step-scan FTIR spectroscopy is enabled by improved mirror control which allows the mirror to stop or virtually stop around a point so that multiple samples can be collected. The position and motion of the mirror is controlled by a magnetic voice coil connected to a digital controller that references the interference fringes of the HeNe laser [15]. Holding the mirror in a fixed position with nanometer precision is a difficult task but advances in control technology have made this measurement available for high speed, repeatable processes like ICE operation.

2.4.2 Crank-Angle Resolved FTIR Spectroscopy.

Typical applications of FTIR spectroscopy in ICE diagnostics seek to quantify combustion products in a time-averaged measurement that represents the engine's operation at a single condition. The requirement of sampling a small amount of exhaust gas inside the spectrometer and far from the engine makes this an inherently time-averaged measurement. It is desirable to understand the relative concentrations and temperatures of the combustion products with respect to crank angle degrees (CAD) so a different method must be used to perform the measurement. Crank-angle resolved FTIR spectroscopy addresses this by drawing on the fast nature of the individual samples that make up an interferogram to collect multiple, parallel interferograms at many points in the engine cycle.

Rein [19] investigated a variety of methods for collecting crank angle resolved FTIR spectroscopy measurements in a 190 cm^3, four stroke ICE and a 2440 cm^3 single-cylinder oil-test engine. Testing performed included emissive measurements on both engines and absorptive measurements on the 190 cm^3 engine in the mid-IR

band between. The measurements were taken in-cylinder by an optical spark plug probe. The modulated light was transmitted to and from an optical spark plug probe via sulfide fiber-optics. The probe used sapphire rods to bring the light into the combustion chamber where it was reflected off of a mirror and returned to an $InSb$ optical detector.

In these experiments, the interferometer was scanned repeatedly at a rate independent and unrelated to the speed of the engine. Simultaneously, the engine was run and angular position was recorded. The engine was held at a constant speed and load setting. It was assumed that the engine operation was sufficiently repeatable so that the same angular point from different cycles could be averaged together. Measurements were taken for a time deemed necessary to gain a sufficient amount of data for good SNR characteristics. After the test, the samples were sorted so that individual interferograms could be populated for different angular positions of the engine and the spectra processed. Figure 2.14 shows selected spectra for the engine during the intake and power strokes. It can be seen that the concentration of fuel in the mixture, as measured by bulk C-H bonds, increases during intake, reaches a peak near TDC, and then is consumed quickly until 20° ATDC when there is no detectable UHC signal remaining.
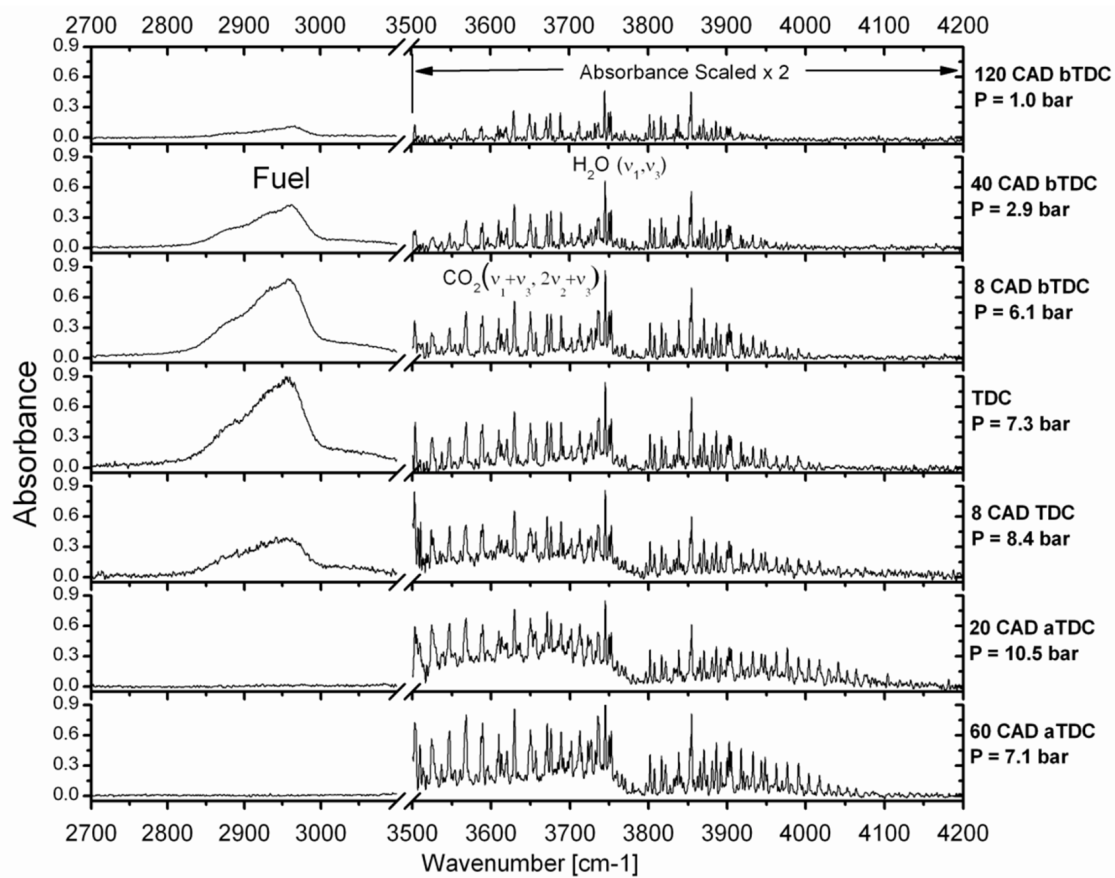
Figure 2.14. Measured absorption spectra at seven crank positions as collected by Rein [19].

III. Experimental Setup

The objectives identified in Chapter I all required extensive facility support to meet the experimentation requirements that they establish. This chapter documents the experimental setup designed, built, and operated in support of testing related to each of the three objectives.

3.1   Small Engine Research Bench

The experimental capability documented here was built around a small engine research bench that was constructed specifically to test engines with up to 6 kW of power output. It was designed to provide full control of small internal combustion engines for speed, load, and operating point. The small engine research bench has been developed incrementally by Ausserer et al., Rittenhouse et al., and Rowton et al. [2] [21] [23]. The development work previously completed on this facility was leveraged as a starting point for the build up for this experimental effort.

The small engine research bench was designed to provide the ability to operate an engine in a controlled manner so that data about the performance of the engine may be collected. Figure 3.1 shows a diagram of the small engine research bench in the configuration used for this research and Figure 3.2 shows an overhead image of the same. The components and subsystems shown in these figures are used to operate, control, and monitor engines and their performance. The major subsystems of the small engine research bench will be discussed in this section.
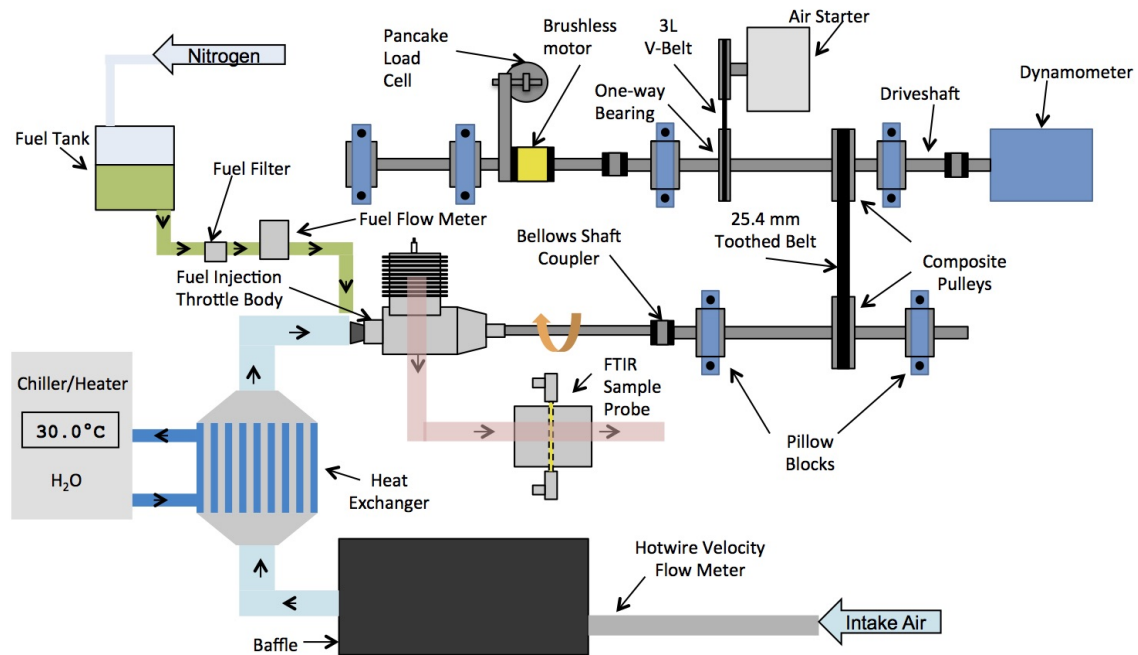
Figure 3.1. A diagram of the small engine research bench.
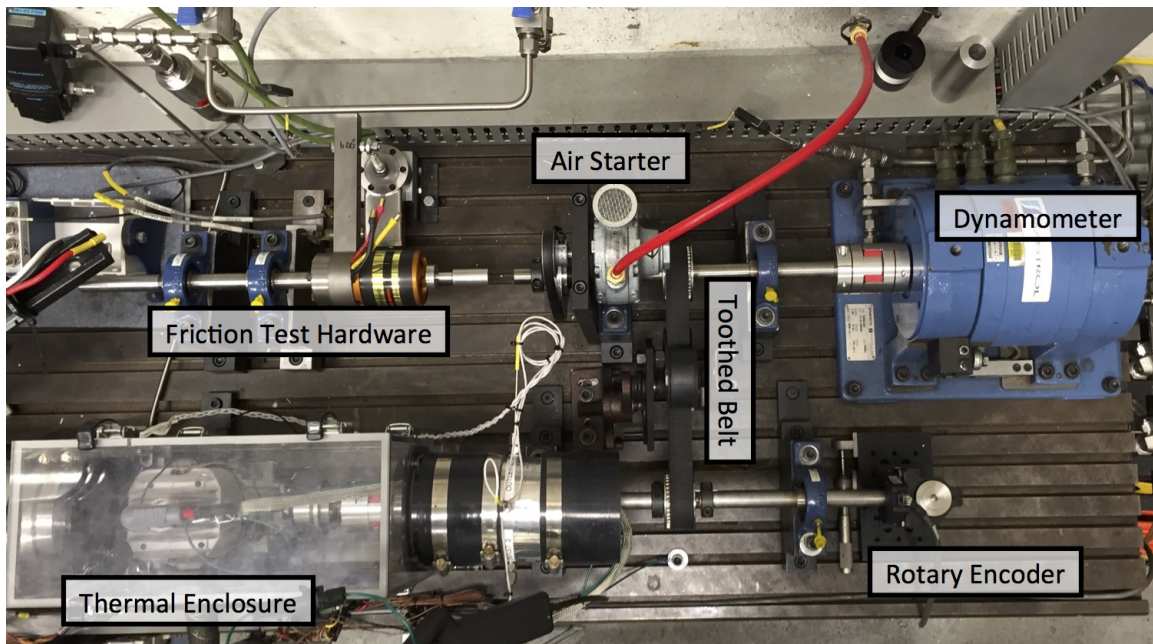
Figure 3.2. Overhead view of the small engine research bench.

3.1.1 Dynamometer and Drivetrain.

The core functionality of the small engine research bench was the ability to operate engines at different conditions. The speed of and load on the engine was maintained by a Magtrol 1WB-65 eddy current dynamometer, shown on the small engine research bench in Figure 3.3. It was water-cooled and had an adjustable, closed-loop proportional-integral-derivitive (PID) controller for constant speed or torque settings. The dynamometer was capable of dissipating up to 6 kW of continuous shaft power. Speed was measured from a 60 tooth reluctor ring internal to the unit. Applied torque was measured by a beam type load cell 105 mm from the centerline of the shaft. The dynamometer was mounted to a T-slot steel optical table for location and alignment that formed a foundation for the entire small engine research bench.
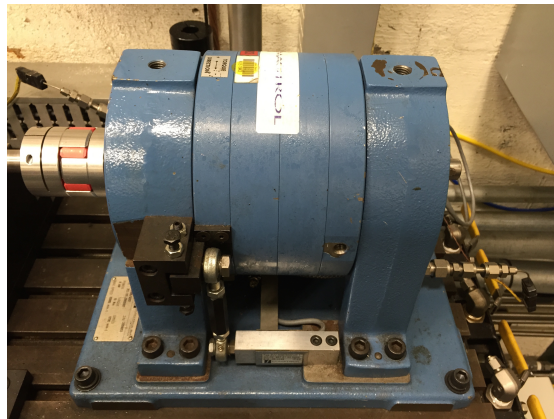
Figure 3.3. The water cooled, eddy current dynamometer used measure engine power.

The engine and dynamometer were connected by two parallel 19.05 mm diameter, precision stainless steel shafts supported on high speed pillow-block bearings. The shafts were connected to the engine and dynamometer by zero-backlash spider couplers. A 25.4 mm wide, toothed belt similar to an automotive camshaft timing belt connected the two shafts at a 1:1 ratio and kept them synchronized, as shown in Figure 3.4. The belt was tensioned on the slack side by an idler pulley on a radial

spring tensioner. The tensioned side had a fixed idler pulley to prevent undesired motions at high speed. High speed pillow-block bearings were used to support and anchor the shafts in place. The bearings were ABEC-1 class, high-seed bearings and have grease fittings for periodic lubrication. The bearings were mounted on custom riser blocks that attached to the T-slot table. The platforms raised the bearings to a uniform height. Minor differences in height were adjusted out by thin metal shims to ensure proper alignment. The shafts were aligned to the engine and dynamometer with alignment sleeves that provide ±0.25 mm of precision in translation; spider couplers absorbed any remaining misalignment.
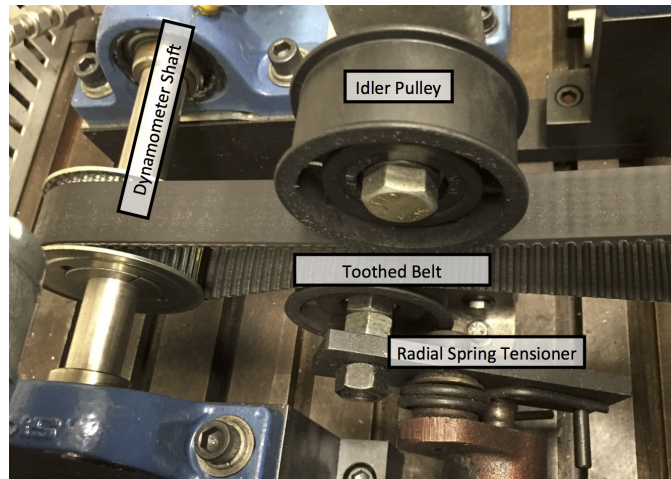
Figure 3.4. Toothed belt assembly that connected the shafts with idler pulleys and pillow block bearings visible.

Primary speed and angular position information were gathered by a US Digital E6 quadrature shaft encoder shown in Figure 3.5. This encoder provided a high speed, digital signal corresponding to the position of the shaft attached to the engine. The encoder wheel had 1800 counts per revolution and provided an angular resolution of 0.2 degrees. The encoder wheel was mounted to the shaft and the support for the optical reader and base were provided by a pillar-post mount attached to single axis translational mount on the T-slot table.
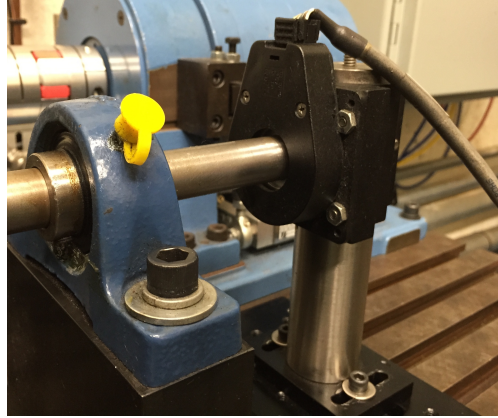
Figure 3.5. Optical encoder used to track engine position with $0.2°$ resolution.

The engine was started by an pneumatic air starter attached to the dynamometer shaft. The air starter, shown in Figure 3.6, was connected to the shaft by a 3L-sized v-belt with a 50.8 mm pitch-diameter pulley on the air starter and a 101.6 mm pitch-diameter pulley on the dynamometer shaft. These pulleys provided 2:1 torque multiplication for the starter and are shown in Figure 3.7. To reduce drag on the running engine, the shaft pulley included a press fit, one-way needle bearing that allowed the shaft to disconnect from the pulley once the speed of the engine exceeded the speed of the air starter.

It was found that commercially available pulleys were not designed to have press-fit bearings inserted. They also typically had an asymmetric mounting on the shaft that applied a torsional load in the longitudinal direction of the shaft. An offset pulley was originally used. The asymmetric loading caused the bearing to fail, ruining the shaft after only a few minutes of operation. A custom pulley was designed and manufactured out of aluminum to accept the 25.4 mm diameter one-way bearing with a 0.025 mm interference fit. The pulley was designed so that the bearing would be completely enclosed and centered with respect to the v-belt. Needle-type thrust bearings were used on either side of the pulley with locking collars to locate the assembly on the shaft and prevent walkout during operation.
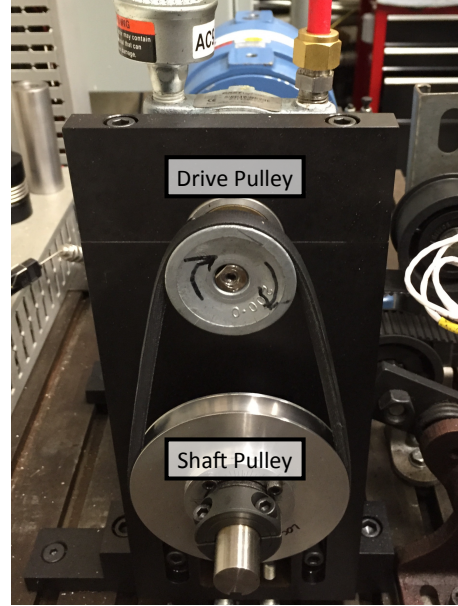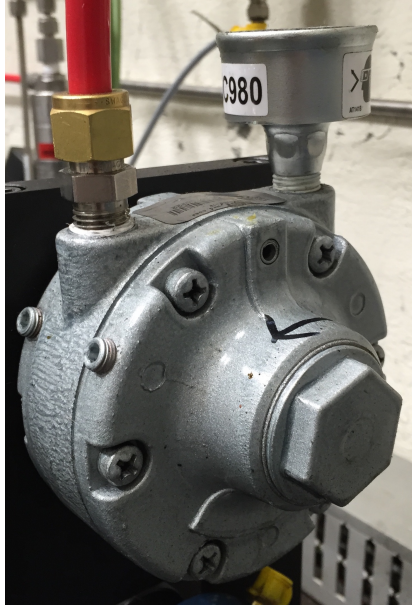
Figure 3.6. The pneumatic air starter.

Figure 3.7. The air starter v-belt pulleys.

3.1.2   Dynamometer Drivetrain Friction Calibration Hardware.

Previous testing on the small engine test bench had not considered how losses in the dynamometer drivetrain might reduce the power measured by the dynamometer. The multiple shafts, belts, and bearings all induced losses in the system that reduced the power measured. It was important to develop a better understanding of the magnitude of this the parasitic friction in the dynamometer drivetrain and its effect. A system was designed and constructed which attached an electric motor to the drivetrain to spin the shafts and hardware. Similar to the dynamometer, a method to measure torque was implemented using a load cell at a fixed radial distance from the center of the shaft. The motors used were AXi 5330-18 and 5345-16 out-runner brushless motors and were controlled by a Castle Edge HV160F, 50 volt, 160 amp direct current (DC) brushless motor controller. The controller took high-amperage, DC input and converted it to a variable frequency and current, three phase alternating current (AC) output for the brushless motor. The motor, controller and batteries were commercially available components designed for giant-scale model aircraft and large

47

acrobatic model helicopters. They were chosen due to their low costs, high output, and availability.

The first reaction fixture designed was made from 101.2 mm steel tubing and served to support the motor and locate it relative to the shaft and load cells. Two load cells were mounted 127 mm to the right and left of the centerline as shown in Figure 3.8 and were connected by adjustable turnbuckle linkages to prevent lateral loadings and torques on the load cells. Additional adjustable turnbuckle linkages were used to secure the reaction fixture in all axes except for axial rotation. Each load cell had a ± 44.5 N capacity. In this manner, the load cells supported the weight of the motor and steel reaction fixture while allowing a torque to be measured as a force couple.

This configuration was susceptible to undesirable loadings from any minute misalignment in the assembly, unbalanced rotating parts, and other imperfections. Figure 3.9 shows the effect of these imperfections on the force readings from the load cell through approximately four rotations of the shaft at very low speed. Visible is a once per revolution force typical of a minor shaft misalignment that creates a large offset load in both load cells of approximately ± 9 N. There is also a smaller, high frequency torque as indicated by opposing magnitudes of the forces on the plot. This pattern corresponds to the poles of the brushless motor, in this case 14 per revolution, as the motor overcomes the magnetic force of each pole. The forces shown in Figure 3.9 were exacerbated at high speed to create severe vibration. The data collected from initial tests of the system proved to have high noise and both load cells were saturated.
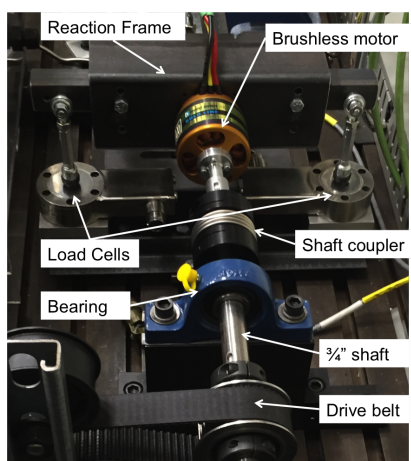
Figure 3.8. First generation reaction fixture.
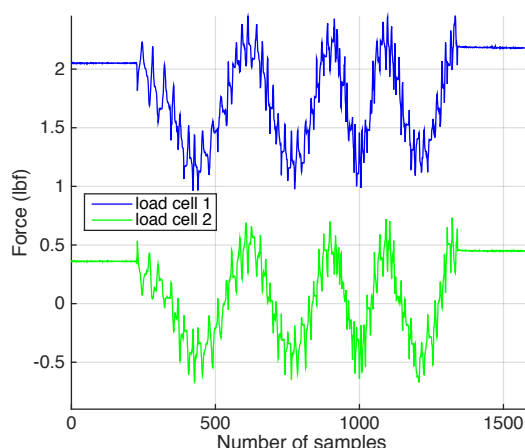
Figure 3.9. Force measurements showing torque potential and cyclic static loading.

Checkout of the assembly indicated that the friction calibration hardware as designed would not provide acceptable results. The literature was consulted for information that may be helpful to design a torque measuring setup that was more insensitive to vibration. Menon and Cadou developed a small engine dynamometer that mounted the engine on a shaft to allow torque to be measured by a load cell. The use of a stationary shaft, supported by bearings, eliminated motion in all axes except axial rotation while permitting axial torques to be transmitted to the load cell [16]. Starting with this information, a new reaction device was designed to reduce the impact of vibration on the force measurement at the load cell.

The redesigned friction testing reaction fixture was comprised of two parts; a lever arm to attach to the electric motor and load cell via linkage, and the stationary support shaft. A diagram of the revised friction testing setup is shown in Figure 3.10. The lever arm was designed so that the motor attached directly to it and was secured with recessed cap screws. The stationary support shaft attached to the lever arm with additional screws to make an assembly. The assembly was mounted on the same type of pillow block bearings used on the driveshafts for commonality, as shown

49

in seen in Figure 3.11. Set screws were used to secure the shaft in the pillow blocks. A single load cell with a ±44.5 N capacity was connected to the 152.4 mm lever arm to measure torque. Due to space limitations on the T-slot table, the assembly was attached to the dynamometer shaft instead of the engine output shaft. In this configuration power was not directly routed through the toothed belt, eliminating the ability test the exact configuration used to . A zero-backlash spider coupling attached the motor and the shaft. The resulting assembly demonstrated significant reduction in translational loading when spun at slow speeds, as seen in Figure 3.12.
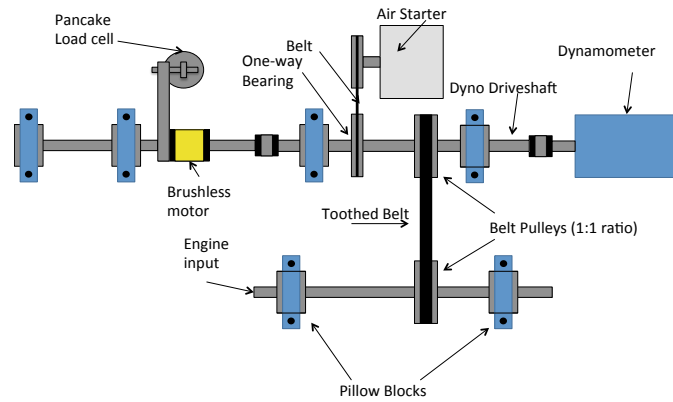
Figure 3.10. Small engine test bench showing friction testing setup.
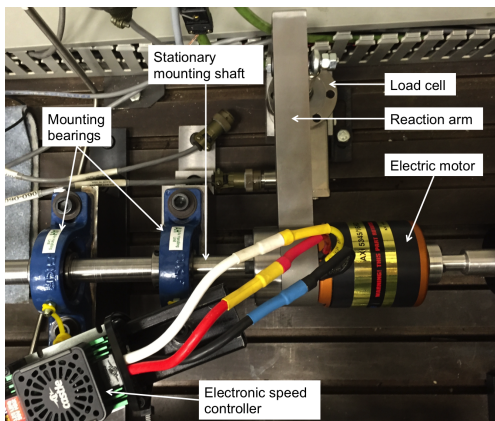
Figure 3.11. Second generation reaction fixture.
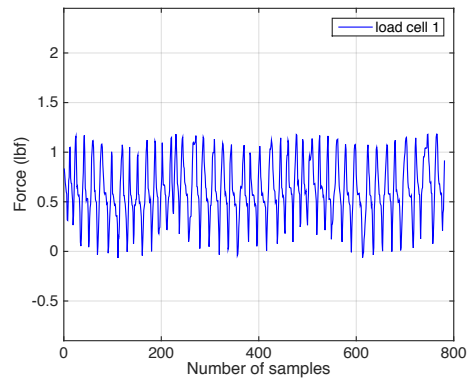
Figure 3.12. Force measurements showing torque potential on redesigned hardware.

50

The following equations were used to calculate the performance of the electric motor during drivetrain friction calibration testing. The torque (τ) of the motor is calculated in Equation 3.1.

$$\tau = \mathbf{F_{loadcell}} \times \mathbf{r} \tag{3.1}$$

where F is given in units of Newtons and r is the length of the lever arm, in this case 0.1524 m. Power is calculated in Equation 3.2.

$$\mathbf{P_{motor}} = 2\tau\mathbf{N} \tag{3.2}$$

The power of the electric motor is given in units of watts where speed is measured by the dynamometer as revolutions per second. The electric motor was operated at maximum power and the dynamometer was used to absorb the power produced by the electric motor and maintain a constant speed. The shaft power that was absorbed and measured by the dynamometer was subtracted from the shaft power produced by the electric motor to calculate the power absorbed by the drivetrain at speed. The results and analysis of the dynamometer drivetrain friction testing effort are given in Section 4.1.

The efficient operating speeds for the brushless motor were determined by the supply voltage and a manufacturer provided kV specification. The kV specification for the AXi 5345/16 motor was 195 revolutions per minute (RPM) per volt and this used to calculate the unloaded speed of the motor for a supply voltage. Electrical power was provided to the system by lithium polymer chemistry batteries with a 4.2 volt nominal cell potential. Battery packs made of four, five and six cells were used, which were combined as pairs for eight, ten and twelve cell packs to set the appropriate input voltage level for the desired speed.

Several motors were destroyed during tests due to excessive electrical loads. The

motors were found to have low stall torque and were sensitive to rapid changes in speed. The default firmware of the electronic speed controller did not place limits on how quickly the speed or load could be commanded to change. Rapid changes in speed induced a ripple current through the motor that caused the windings to overheat and short-circuit. Revised electronic speed controller settings were developed in conjunction with the manufacturer of the controller to alleviate the excessive current draw during changes in the operating condition. The revised settings were derived from those intended for large acrobatic helicopters which seek to keep the rotor blades at a constant speed and vary the torque rapidly to reduce component stress. The slow, progressive loading enabled by these controller settings increased the life of the motors used.

3.1.3 Air and Fuel Delivery.

Intake airflow for the engine was first drawn into a pipe with an internal diameter of 50.8 mm. A hot wire based air velocity transmitter, pictured in Figure 3.13, was mounted in the pipe 15 diameters from the inlet and measured the velocity of the airflow near the center of the pipe. A turbulent velocity profile model was chosen based on the internal flow Reynolds number and was used to determine the bulk flow velocity. The mass flow was calculated from the velocity measurement and the density of the ambient air in Equation 3.3. The intake pipe lead into a 208 L barrel with internal baffles to ensure steady flow for intake velocity and pressure measurements. Downstream of the intake baffle was an air to water heat exchanger. The heat exchanger was combined with a water bath temperature regulator to hold a consistent 30.0° C temperature for all intake conditions, as shown in Figure 3.14.

$$\dot{m}_{intake} = \frac{2\pi R^2 U_{hotwire}}{1/7 + 2} \frac{p_{intake}}{R T_{intake}} \pi R^2 \qquad (3.3)$$
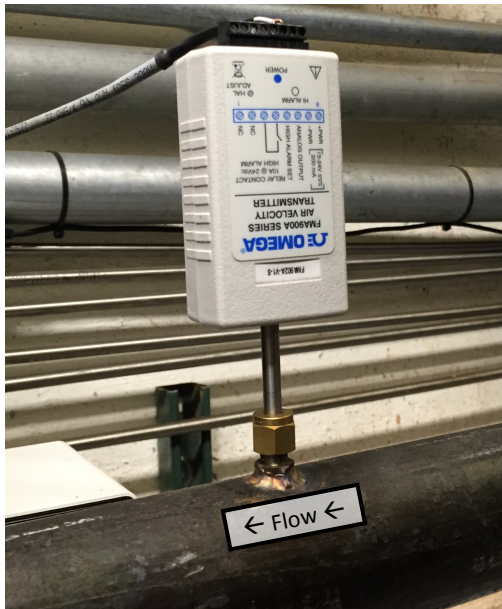
Figure 3.13. The intake pipe hot wire for intake mass flow measurements.
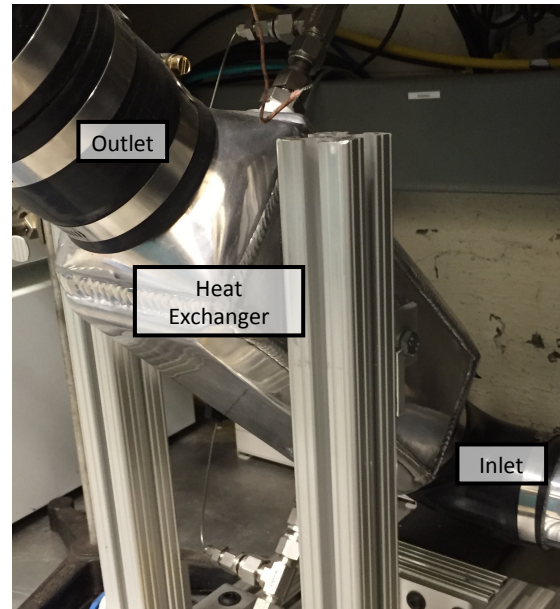
Figure 3.14. The air to water heat exchanger used to condition the intake air.

A primary reference fuel of 98 parts iso-octane and two parts n-heptane for an octane rating of 98 was used on the small engine research bench. The use of primary reference fuel eliminates uncertainty in fuel composition, heating value, and physical properties. Fuel was provided to the engines by a nitrogen pressurized fuel external fuel system. One tank included a bladder to prevent nitrogen saturation in the fuel during operation and the second tank was used for storage and filling of the fuel blend. The fuel was routed through a series of filters and a high precision, piston-type flow meter. The flow meter provided an analog signal for precise measurements of fuel flow in real time. Pressure was regulated and fully adjustable to accommodate carbureted or electronic fuel injection systems.

3.1.4 Thermal Enclosure and Engine Cooling.

The engines were mounted in a thermal enclosure with an instrumented cooling flow to control operating temperature and measure heat rejection. The thermal en-

closure was constructed of clear, 6.35 mm thick polycarbonate and formed a control volume around the engine, as shown in Figure 3.15. There were openings for cooling air intake and exhaust flow as well a pass through for the exhaust manifold. A 480v three-phase centrifugal blower connected to a variable frequency drive provided high speed airflow to the cooling enclosure. It was desired to replicate the cooling conditions experienced by a small ICE mounted in an aircraft with forced convection from the propeller. The mass flow rate of air to the enclosure was estimated by a hot wire based air velocity transmitter. Three resistance temperature detectors on both the inlet and outlet of the thermal enclosure measured cooling flow temperature. The difference in temperature at the inlet and outlet combined with the mass flow and an ideal-gas assumption was used to estimate the heat rejection of the engine, as shown in Equation 3.4.

$$\dot{Q}_{cool} = \rho A V_{bulk} C_{p_{air}} (T_{outlet} - T_{inlet}) \tag{3.4}$$
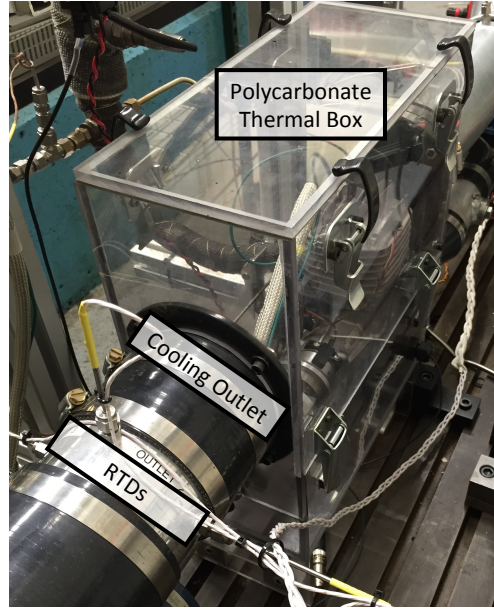
Figure 3.15. The thermal enclosure and RTDs used to estimate cooling load.

3.1.5 Data Acquisition and Diagnostics.

Data acquisition was handled jointly by two different systems, depending on the requirements of the measurement. Primary data was collected by a National Instruments FieldPoint compact data acquisition system. This system provided digital counters, analog inputs, analog outputs, relay control, thermocouple, and resistance temperature device acquisition. Data was read, processed, and stored by a custom LabView computer program that also controlled the cooling blower and dynamometer. Data was written serially to a binary data file that allows post processing of the full data collected on the small engine bench.

High speed data collection was made by an AVL IndiSmart combustion analyzer. This system conducted data acquisition on various high speed sensors including in-cylinder pressure, intake pressure, and exhaust pressure transducers. All data was processed with respect to CAD as read from the quadrature encoder mounted on the shaft. The combustion analyzer system allowed real time tracing of pressure-volume diagrams, pressure versus CAD, spark timing, injector timing, and injector duration. Calculated from these measurements were indicators of performance including IMEP, IMEP CoV, and $CA_{50\%}$. These values were averaged over 400 engine cycles to show a moving average of engine performance. Figure 3.16 shows the spark plug pressure transducer and flush-mounted in-cylinder pressure transducer installed in the cylinder head of the 55 cm^3 two-stroke engine.
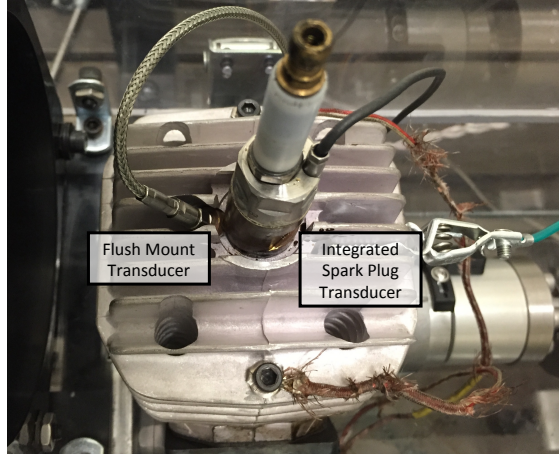
Figure 3.16. Spark plug and flush mount in-cylinder pressure transducers.

3.2 Research Engines

The small engine research bench was used in previous work to quantify the performance of a set of three, two-stroke engines with displacements of 28 cm^3, 55 cm^3, and 85 cm^3 from the manufacturer 3W-Modellmotoren GmbH. They were crankcase scavenged with a Schnürle-loop intake port configuration. Schnürle-loop scavenging is a hybrid between cross scavenged and loop scavenged designs where each engine has three intake ports and a single exhaust port. Two transfer ports provide the majority of intake flow while a third, smaller boost port energizes the charge for improved mixing near the top of the cylinder [10]. Timing varies between the boost port and transfer ports in Schnürle loop configurations due to the different geometry and position required for the full effect. The intake charge was drawn into the crankcase through a carburetor as equipped from the manufacturer and reed valves sealed the crankcase on the downward stroke of the piston to prevent reverse flow.

The engines all had spark ignition and a hemispherical combustion chamber. The factory ignition was digitally controlled with a linear advance. Crankshaft position was measured once per revolution by a hall-effect sensor connected to the ignition

56

control unit. The engines were air cooled with fins on the cylinder head and walls. The moving parts were lubricated by an ash-less lubricating oil premixed in the fuel system at a ratio of 50:1. The crankshaft and connecting rod were supported by needle bearings to reduce friction and required lubrication. All engines had aluminum construction for the crankcase, cylinder head, and piston. The 28 cm^3 and 55 cm^3 engines had a single piston ring and a single exhaust port. The 85 cm^3 engine had two piston rings and two exhaust ports. The manufacturer performance data and specifications of the three engines are listed in Table 3.1. This work primarily focuses on the 55 cm^3 engine. In carbureted form, the engine had a rated output of 3.9 kW. Figure 3.17 shows the engine as delivered from the manufacturer, equipped with carburetor.

Table 3.1. Engine geometric and performance parameters.

Engine	3W-28i	3W-55i	3W-85Xi
Displacement (cc)	28	55	85
Rated power (kW)	2.5	3.9	6.8
Mass (kg)	1.21	1.94	2.40
Bore (cm)	3.6	4.5	5.1
Stroke (cm)	2.8	3.5	4.1
Compression Ratio	10:1	10:1	10:1
Exhaust Port Timing (CAD)	106°	103°	104° + 97°
Transfer Port Timing (CAD)	125°	118°	124°
Boost Port Timing (CAD)	121°	110°	118°
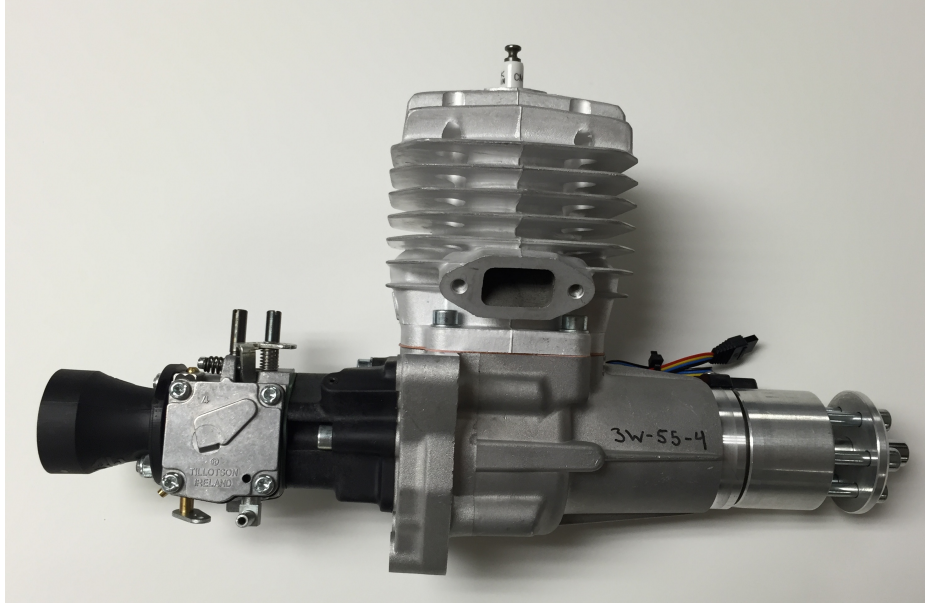
Figure 3.17. The exhaust port side of the 55 cm^3 engine with carburetor installed.

3.2.1 Electronic Fuel Injection.

The 55 cm^3 engine was converted to an electronic, port fuel injection system to maintain better control over mixture. The throttle body was part of a complete conversion kit manufactured by Currawong Engineering specifically designed for these engines. In this application, only the throttle body with the throttle plate servo and injector was used for the conversion to electronic fuel injection (EFI). A custom fuel injector designed for the low fuel delivery rates required for this engine was used. Fuel pressure was set by the nitrogen pressurization level in the accumulator tanks previously described in Section 3.1.3.

Fuel injection was controlled by a custom laboratory engine control unit (ECU) that was developed in-house. It was based on the XMOS XS1-L high-speed micro controller. The ECU was programmed to maintain full control of an engine's spark timing, injection timing, and injector duration. Spark energy was produced by a digital inductive ignition coil manufactured by AEM. The ECU maintained synchro-

nization with the engine through the digital quadrature encoder. A custom LabView program enabled the operator to communicate with and control the ECU and adjust any of the parameters while the engine was running.

3.3   Fourier Transform Infrared Spectrometer

The FTIR spectrometry analysis capability was intended to provide in-situ measurements of the exhaust gases while the engine is operating. This capability was built around a Thermo Scientific IS-50R research spectrometer shown in Figure 3.18. This instrument had a spectral range of 7,800 cm^{-1} to 350 cm^{-1}. The instrument was capable of resolving spectral resolutions as small as 0.09 cm^{-1}. It was equipped with a coated KBr beamsplitter in the interferometer to promote operation in the mid-wavelength infrared (mid-IR) spectral range of 5,000 cm^{-1} to 2,000 cm^{-1}, or 2 μm to 5 μm, respectively. The instrument was also equipped with a liquid nitrogen cooled, mercury cadmium telluride (MCT) detector with external AC and DC analog signal outputs. The nitrogen dewar provided 18 hours of cooled detector operation between fills. The body of the FTIR spectrometer was desiccated and purged by dry nitrogen recovered from a 500 L liquid nitrogen dewar. The instrument was also fitted with an external signals hub that provided the ability to directly interface with many of the inputs and outputs in the FTIR spectrometer. Figure 3.19 shows a diagram of the entire FTIR spectroscopy experimental setup used in this effort.
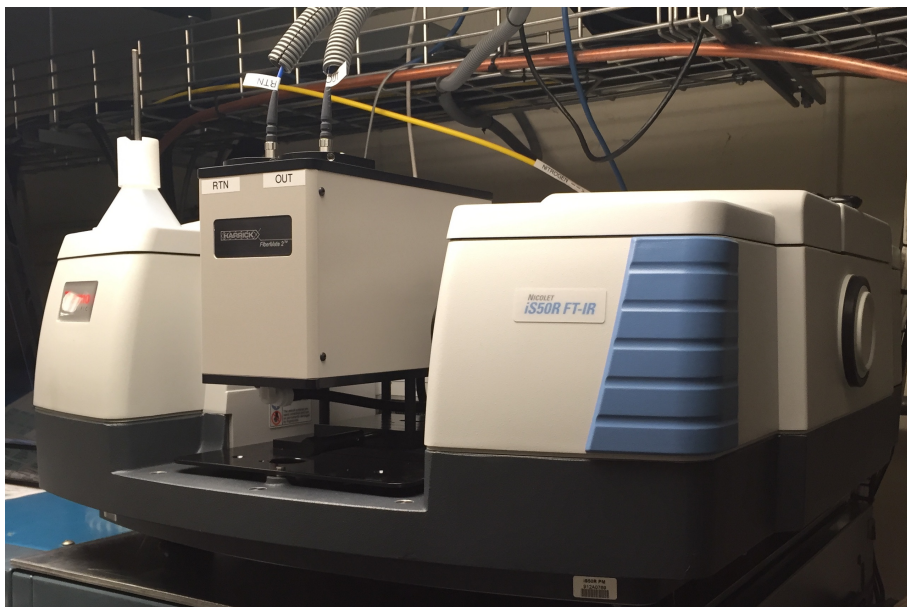
Figure 3.18. The FTIR spectrometer.
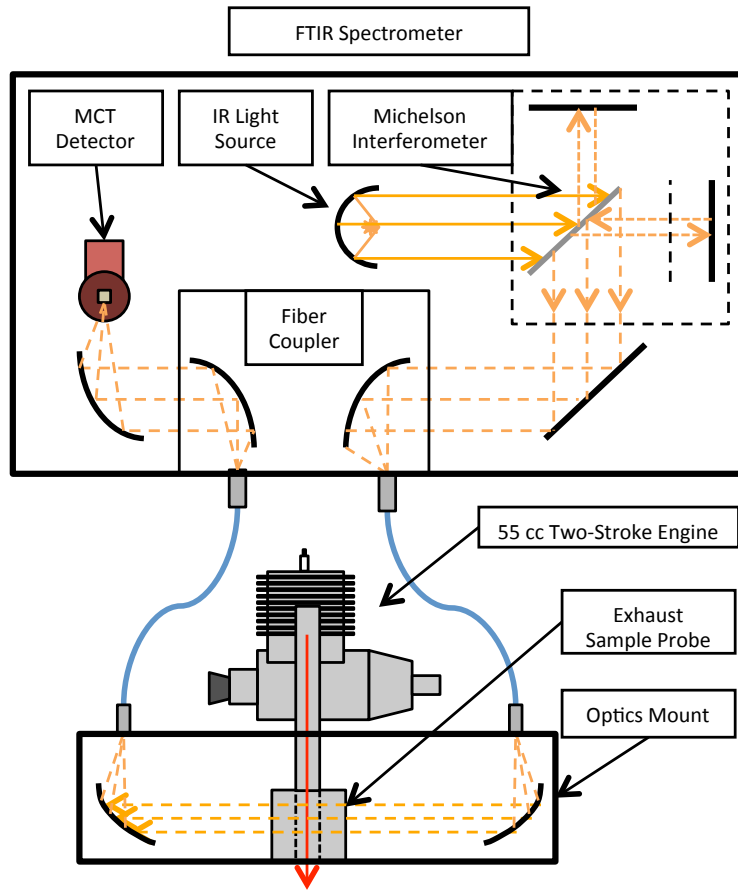
Figure 3.19. Diagram of the entire FTIR spectroscopy experimental setup.

3.3.1 Fiber Optics.

The FTIR spectrometer was required to be located in a separate room from the small engine research bench to protect the instrument. In-situ measurements of exhaust gasses required fiber optics to transport the modulated light to the optical exhaust probe and back. The light was focused into the fiber optics using a Harrick FiberMate II fiber optic coupler. This device was installed in the sample compartment of the FTIR spectrometer. It used off axis, parabolic reflectors to focus the light received into a 1 mm spot size at the tip of the fiber. It was equipped to accept SMA fiber optic connectors and provided full adjustability of alignment through tilt

and rotation of the internal focusing optics as well as two axis translational adjustment of the SMA connectors. The fiber optic coupler is shown installed in the FTIR spectrometer in Figure 3.20.
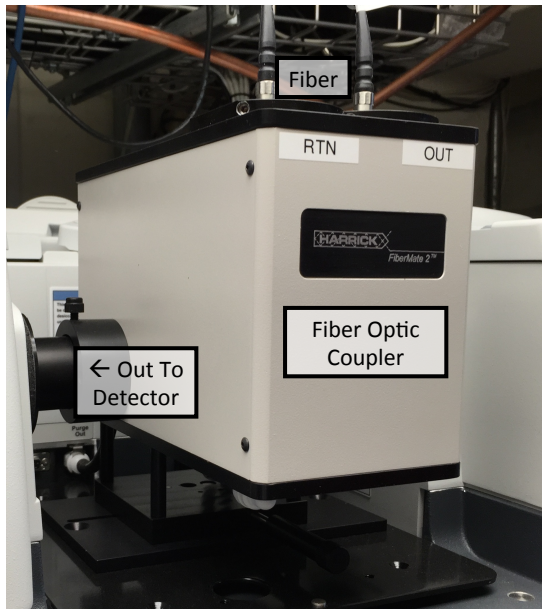
Figure 3.20. The fiber optic coupler used to interface with the FTIR spectrometer.

The fiber used was carefully selected to maximize signal throughput. Calcogenide glass fibers were historically used in mid-IR applications; however, they do not provide sufficient signal propagation for long fiber runs beyond 1 m. Multimode fluoride based fibers have excellent signal propagation characteristics, lower cost, and much greater durability than calcogenide fibers. Figure 3.21 shows the transmission properties of the InF_3 fiber used in these experiments. The high-performance optical characteristics of fluoride fiber enabled this experiment which required long separations of the FTIR spectrometer and the sample probe of greater than one meter. An InF_3 fiber with a 100 μm core diameter from Thorlabs was selected for this application. Two custom fibers were obtained with 4.0 m length and SMA connectors on each end. The fiber ends have a numerical aperture of 0.26 in the mid-IR band. The fibers were housed in plastic conduit and run through the 30 cm concrete wall.
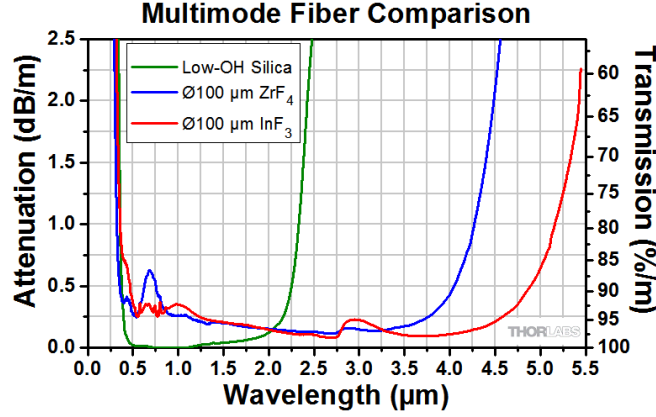
Figure 3.21. Transmission and attenuation per meter of InF$_3$ fiber (in red). [26]

3.3.2 Data Acquisition and Control.

Two primary modes of FTIR spectrometry data collection and acquisition were used. Linear-scan measurements were the traditional mode of data collection where the interferometer mirror moves continuously and is sampled at regular intervals by the detector. The second mode used was step-scan interferometry where the mirror is held at a fixed position while data is collected on a repeating process, in this case the operating cycles of the engine. This process is repeated at thousands of mirror positions to populate an entire interferogram. Step-scan interferometry allows interferograms for each angular position of the engine to be collected in parallel.

In the time-averaged linear-scan mode, the operation of the engine was monitored by the small engine research bench data acquisition equipment discussed in Section 3.1.5, while the FTIR spectrometer sampled the interferograms internally. The spectrometer is equipped with an 24 bit analog to digital converter (ADC) and is capable of continuous sampling at 50 k samples/s. For linear-scan measurements, the FTIR spectrometer post-processed the interferograms to produce single beam transmission spectra for analysis.

Crank-angle resolved FTIR spectrometry data acquisition was more complicated.

It was desired to sample the analog detector on every pulse of the quadrature encoder with the engine running for up to an hour at a time to obtain sufficient data for the step-scan measurement. At an engine speed of 8000 RPM and sampling the digital encoder on each of its 1800 pulses each revolution, a data rate of 240,000 kHz was required. The data rates and length of the measurement combined with the requirement to synchronize externally with the quadrature encoder required a high performance ADC to collect the analog signal from the detector. A National Instruments PCIe-6353 high speed data acquisition card was selected for its ability to accept an arbitrary clock input at sample rates of up to 1.25 M samples/s.

Proper data collection in step-scan mode required synchronization of the data acquisition card with the engine and mirror position of the FTIR interferometer. A scheme to synchronize all of the instruments and control stepping of the mirror was developed in conjunction with the manufacturer of the FTIR spectrometer. Using simple digital signals in and out of the FTIR spectrometer, the data acquisition card could command the mirror to move after data collection had completed. To improve SNR characteristics, the ability to capture data for multiple engine rotations was required. Custom LabView computer software was developed to interface with the data acquisition card and control all of the functions required for proper step-scan operation. This software monitored the clock signal from the quadrature encoder and tracked mirror position. The software recorded the analog detector signals, mirror position, engine angular position, and time in a binary file for post-processing.

3.4 Optical Exhaust Probe Design

Design of a satisfactory optical sampling probe for the exhaust proved to be challenging. The probe was required to provide an unobtrusive measurement of the exhaust flow, allow optical access to the flow, and provide a fixed OPD for consistent

absorption measurements. The initial study focused on determining a suitable optical path for the anticipated gaseous molar concentrations. Complete combustion of iso-octane in air was assumed. The balanced equation for the combustion of iso-octane in air is shown in Equation 3.5.

$$\mathbf{C_8H_{18} + 12.5(O_2 + 3.76N_2) = 8CO_2 + 9H_2O + 47N_2} \tag{3.5}$$

The combustion products had molar concentrations $X_{CO_2} = 0.125$ and $X_{H_2O} = 0.140$. A temperature of 500 K and pressure of 1 ATM were also assumed for the study. These parameters were input into the spectraplot.com absorbance simulation tool for a numerical simulation of absorption spectra using the HITRAN database [14]. A spectral range of 2200 cm^{-1} to 2400 cm^{-1} with a resolution of 4 cm^{-1} was chosen to encapsulate the CO_2 absorbance band. The ability to accurately determine concentrations depends on a known optical path length for absorption to occur. A path length too short will not create detectable absorption. Too long of a path length will attenuate the modulated light to the extent that no light is received by the detector and thus, no spectral information.

To appropriately determine an optical path length, several path lengths were simulated based on a variety of factors. It was initially thought that peak absorbance needed to remain near one. Very short path lengths were chosen for the simulation to meet the absorbance requirements, with distances of 1 mm, 2 mm, and 3 mm as shown in Figures 3.22, 3.23, and 3.24, respectively. These short path lengths were impractical from an experimental perspective since the only way to accommodate this small size would have been to divert a small portion of the exhaust flow through the optical sampling chamber. The absorption bands for CO and H_2O are not visible in this spectral range, although they were included in the simulation.
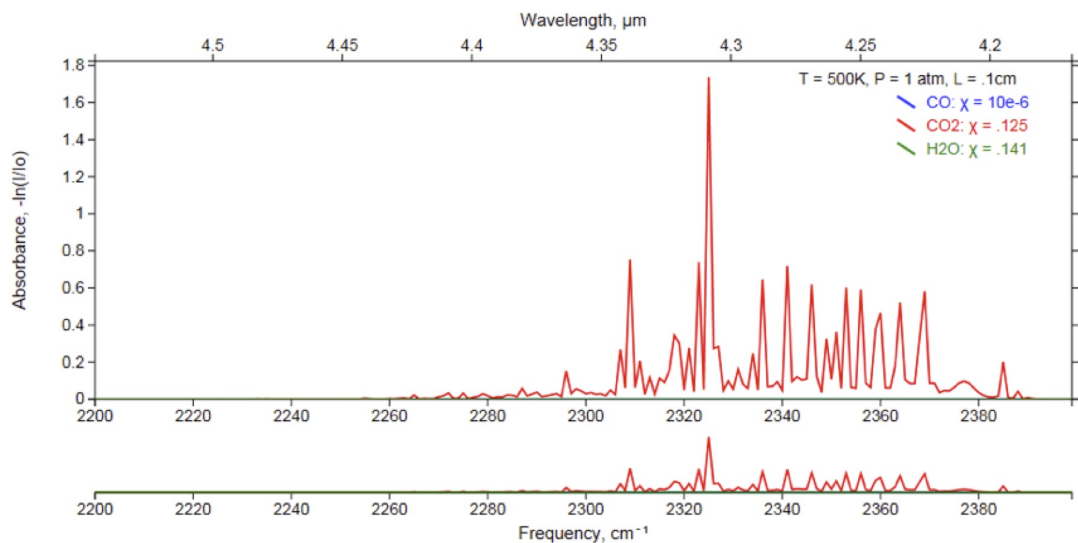
Figure 3.22. Absorbance for $X_{CO_2} = 0.125$ at **500 K and 1 ATM for a 1 mm optical path.**
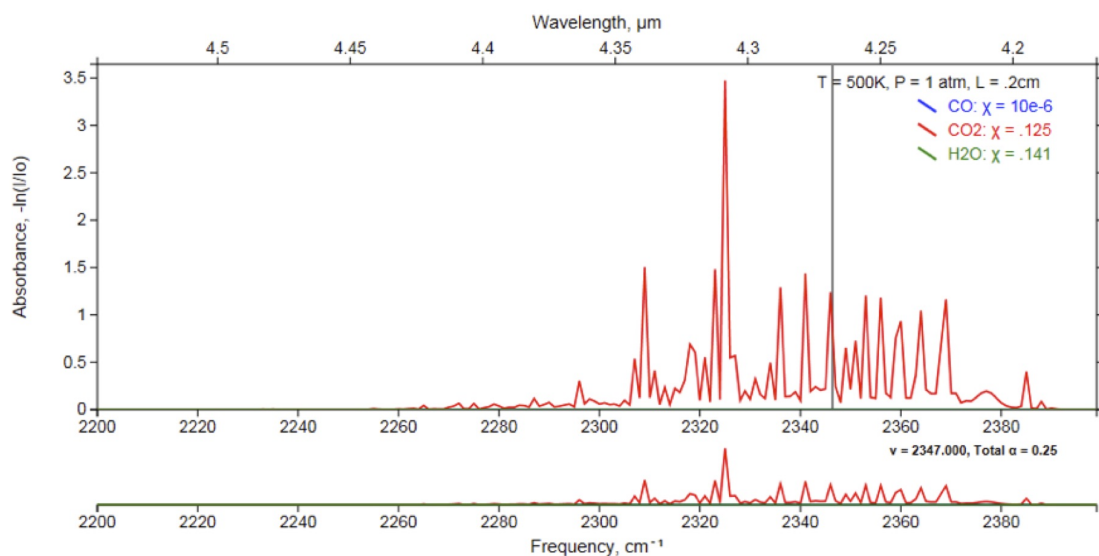
Figure 3.23. Absorbance for $X_{CO_2} = 0.125$ at **500 K and 1 ATM for a 2 mm optical path.**
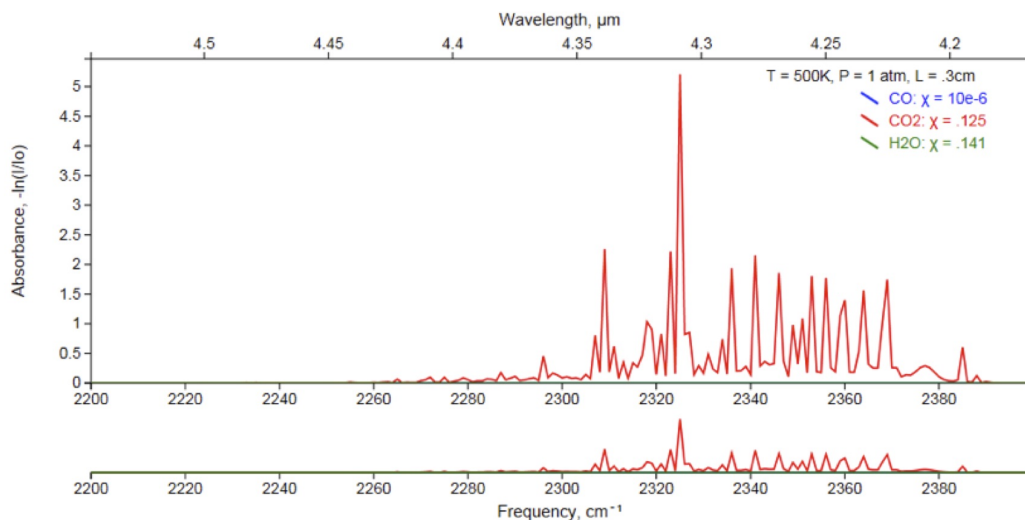
Figure 3.24. Absorbance for $X_{CO_2} = 0.125$ at 500 K and 1 ATM for a 3 mm optical path.

Figure 3.25 shows the absorption simulation results for a 20 mm optical path. This length was chosen based on the input from those experienced with the measurement and because it was similar to the physical dimensions of the exhaust manifold used on the 55 cm^3 engine. The larger size allowed all of the exhaust gases to pass through the optical path, simplifying the design. Absorbance is significantly higher than that for the shorter path lengths simulated. At this level of absorbance, the light signal is heavily attenuated by the gas.
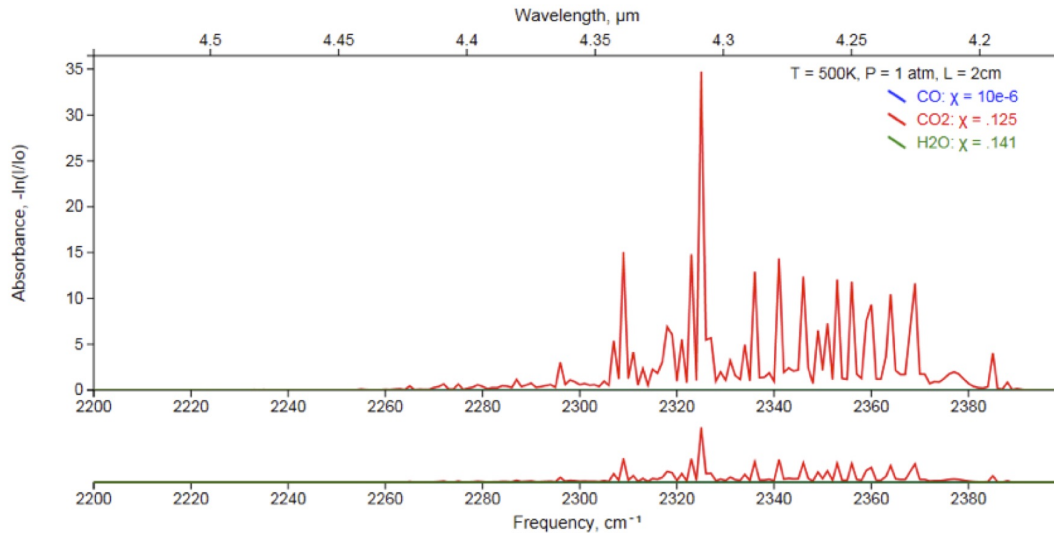
Figure 3.25. Absorbance for $X_{CO_2} = 0.125$ at 500 K and 1 ATM for a 20 mm optical path.

A 20 mm optical path length was chosen as the starting point for the optical exhaust probe based on the practical advantages of this size. The initial design integrated all of the optics as a single unit that was installed in the exhaust and had the entire exhaust flow pass through the unit. The exhaust flows through a 20.3 mm by 15.2 mm flow path, similar to the size of the exhaust flange. The optical components consisted of 12.7 mm x 3.0 mm round sapphire windows, 25.4 mm diameter optics compatible kinematic mounts on a 30.0 mm cage system, 12.7 mm optics compatible off-axis reflective collimators with SMA connectors. Combined with the numerical aperture of the fiber, the collimators produced a 4.0 mm beam. With all of the components integrated, the optical path was 22.3 mm in length.

The optical probe was designed in a manner to include the ability to adjust alignment of the optics, allow the exhaust gas to flow through freely, provide a fixed optical path length, and provide a nitrogen purge outside of the optical path. The first optical probe design was custom machined from mild steel and sought to integrate all

of these functions into a single unit. Two 12.7 mm x 3.0 mm sapphire windows were selected to seal the optical path. These windows were designed to mount in Thorlabs 0.5 in lens tube which was a threaded cylinder designed to mount lenses and other optics. The thread was specified 0.535 in x 40, so this thread was designed into the probe to facilitate containment of the windows using lock rings. The body of the probe was designed to accept 6.0 mm cage rods to form a 30.0 mm cage system to which the kinematic mounts attached. These kinematic mounts provided two axes of adjustability and supported optical collimators that would collimate the beam of modulated light between the fibers. A lossy dry nitrogen purge was employed to remove atmospheric and exhaust gases that may have escaped past by the windows. The first generation optical probe is pictured in Figure 3.26 and Figure 3.27.
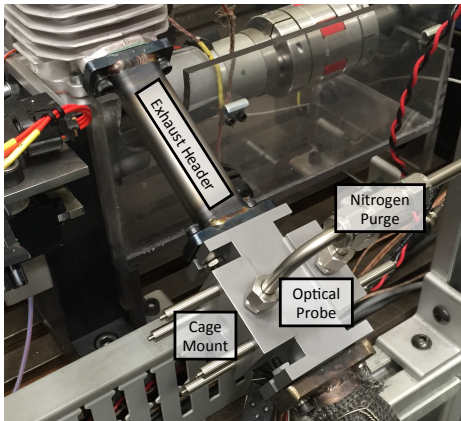
Figure 3.26. First generation optical probe partially assembled.
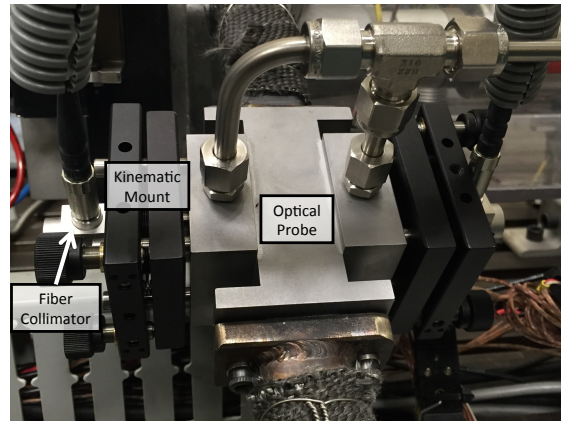
Figure 3.27. First generation optical probe installed in exhaust.

The initial probe was not suited to the heat and vibration present in the location which it was mounted during engine operation. A short engine run of approximately 6 minutes was conducted to test the components. At the end of the run, no light was being transmitted through the system so it was disassembled and inspected. The vibration had loosened the lock rings securing the windows and allowed hot exhaust gases to impinge directly on the sensitive optical components. The reflective

collimators experienced high temperature and had a coating of soot on the mirrors. The ends of the fibers also had a coating of soot. The vibration caused the kinematic mounts to lose their alignment. Figure 3.28 and Figure 3.29 shows the components after teardown and inspection.
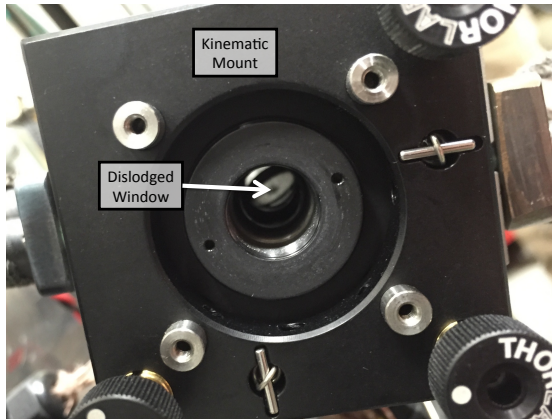
Figure 3.28. Partially disassembled optical probe showing dislodged window (center).
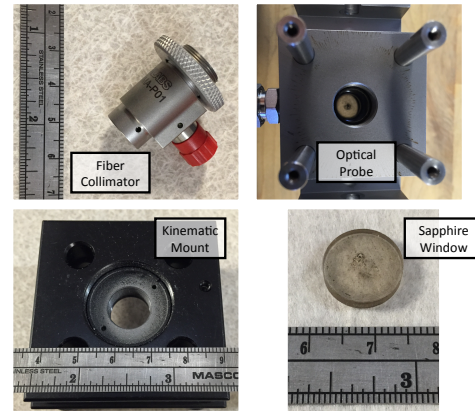
Figure 3.29. Individual optical components showing effects of exhaust impingement.

3.4.1 Revised Optical Probe.

A new optical probe was designed which incorporated lessons learned from the initial design and test. The major goals of the design were secure window mounting, rapid window replacement, consistent optical alignment, and isolation of the optics from heat transfer and vibration. The new optical probe accommodated larger 25.4 mm x 2.25 mm sapphire windows. A cup-like system was designed to securely hold the windows as a unit with graphite gasket material to seal the windows on either side. This window holder assembly used six screws to affix it to the body of the probe. As the screws were tightened, the graphite gaskets compressed to form a complete seal. After installation of the windows and compression of the gaskets, the optical path length was calculated to be $33.66^{+0.00}_{-0.80}$ mm. A dry nitrogen purge was used, similar to the initial design. The disassembled, revised optical probe with the window holder

and a clean sapphire window is shown in Figure 3.30 and fully assembled in Figure 3.31. Figure 3.32 shows a cutaway view of the probe with exhaust flow represented by red arrows and the modulated light represented by yellow arrows.
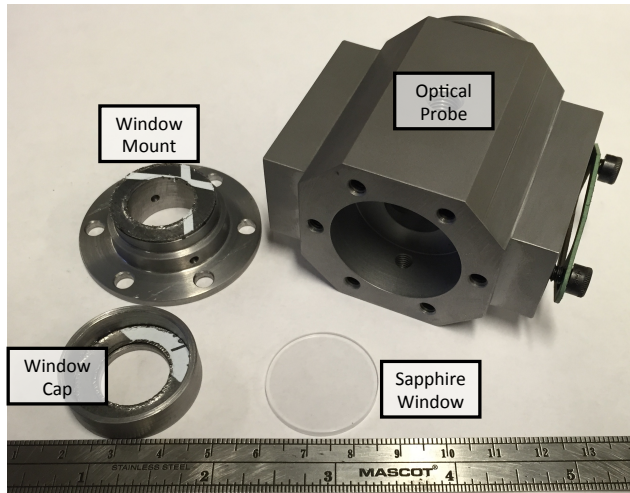
Figure 3.30. Second generation optical probe with window holder components.
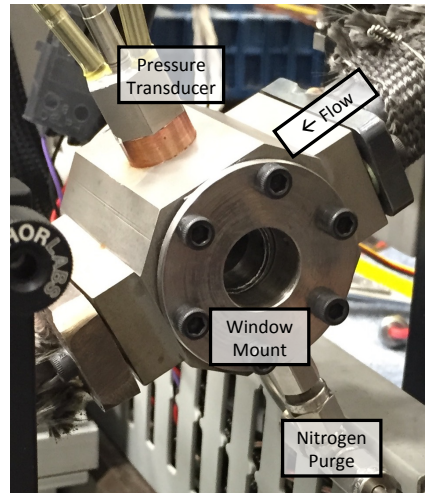
Figure 3.31. Second generation optical probe installed in exhaust.

SECTION A-A
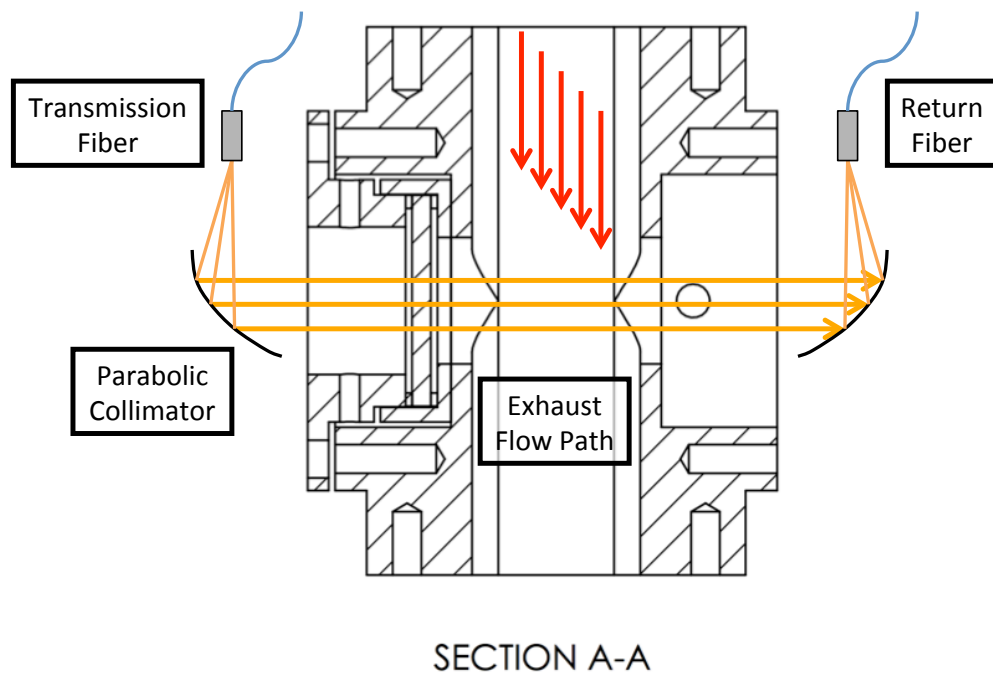
Figure 3.32. Cutaway of optical probe showing exhaust flow and modulated light pathways.

All of the optical components were mounted to the small engine research bench instead of the exhaust tube to maintain alignment, accommodate window replacement, reduce heat transfer from the exhaust, and reduce vibration. A 152 mm by 305 mm optical breadboard was selected to form the base of the optics system. The breadboard was mounted to 45 mm square T-slot tubing that allowed the entire breadboard to be moved and secured as a unit. Attached to the breadboard were 25.4 mm diameter pillar posts with a three point clamp and a 1/4 in - 20 fastener for additional security. On top of the pillar posts were 25.4 mm compatible kinematic mounts with two fine adjustment screws. These kinematic mounts held the reflective collimators and fiber, as seen in Figure 3.33. The structure of the breadboard was ideal; it provided a strong and inflexible base that maintained alignment between the two optical collimators well. It also allowed the optics to be moved out of the way of the optical probe easily and quickly for window changes and alignment by simply loosening four screws and sliding the assembly on the 45 mm T-slot rails, shown in Figure 3.34.
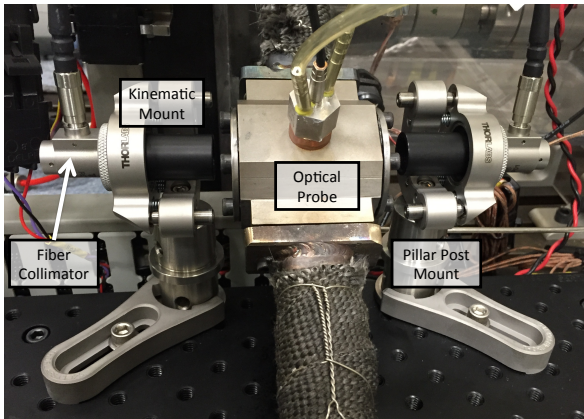
Figure 3.33. The redesigned optical probe fully assembled.
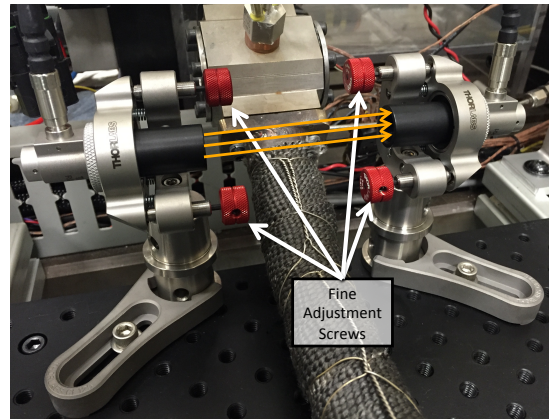
Figure 3.34. The redesigned optical mounting assembly removed from the probe for alignment.

3.4.2 Optical Alignment.

Optimization of light throughput in the optical system was a priority to maximize SNR. A careful and methodical process was followed to align the optics for maximum signal. The FTIR spectrometer was used to measure the light throughput by placing it into a rapid, linear scan state. The peak to peak of magnitude of the interferogram's centerburst was monitored during adjustments. The goal was to have two parallel and collinear collimated beams of light; one from each reflective collimator for maximum light transmission.

Using a visible, red laser fiber tester, the fibers were focused in the reflective collimators by focusing the emitted beam on a piece of paper. Bronze shims were inserted into the SMA connector on the end of the fiber to control the depth of insertion of the fiber in the collimator to focus the emitted beam. The beam was monitored as shims were added until the spot of the collimated beam was crisp and of a minimum diameter, approximately 4.0 mm. Shims with thicknesses of 0.003 in, 0.005 in, 0.010 in, and 0.020 in were available. A total of 0.016 in of shims were used on the ends of both fibers connected to the optical probe. No shims were needed on the fiber optic coupler connectors at the FTIR spectrometer.

The alignment process of the optics was initiated by visually aligning the kinematic mounts to remove large misalignments. A single 8-32 screw attached the kinematic mounts to the pedestal post and allowed them to be rotated on the base. Upon the first signal detected by the FTIR spectrometer, the 8-32 mounting screw was locked in place and the fine adjustment screws were used exclusively. The adjustment screws on the kinematic mounts were rotated by hand to improve signal. Each screw was rotated a small amount until the peak was found. Once the local maxima was found, an intentional perturbation of alignment was added through a significant adjustment of two or more screws. The process used to find a local maxima would be repeated

and compared to the previous value. The overall alignment - perturbation - alignment process was repeated until a global maximum was found. The fiber optic coupler was also adjusted in this manner. Using this method, the signal strength as measured by the peak to peak height of the interferogram at the centerburst was increased to 500% over an initial, best-effort alignment, to 3.2 $\pm$0.2 V. The alignment of the system was checked after each change of the windows before the start of the next test. Minimal adjustment was necessary on the final optics configuration between tests.

IV. Results

This chapter encompasses the results gathered and analysis performed in this experimental effort pursuant to the research objectives listed in Chapter I. In this chapter, each objective will be addressed in the order proposed.

1. Quantify the parasitic losses on engine performance due to drivetrain friction on the small engine research bench and develop a correction for collected data.

2. Convert a 55 cm^3 two-stroke engine to electronic fuel injection, quantify performance, and compare to the performance of the carbureted configuration.

3. Develop both time-averaged and crank-angle resolved quantifications of exhaust gas emissions using FTIR spectroscopy.

4.1   Dynamometer Drivetrain Friction Calibration

Previous works by Rittenhouse et al. and Rowton et al. utilized the small engine research bench to conduct performance testing on small carbureted two-stroke engines. During these efforts, dynamometer drivetrain friction was identified as a potential source of error in the measurement of brake power produced by the engines [21] [23]. The design of hardware, testing, and analysis for drivetrain friction calibration was conducted early in this effort so that additional engine testing would include the appropriate calibration for brake power data collection. The test setup used was previously described in Section 3.1.2. Tests were conducted at speeds from 3000 RPM to 7000 RPM to stay within the voltage limits of the motor while encompassing the majority of the speed range of the 3W engines. Data were recorded at 10 Hz for 10 seconds, which was then averaged. Motor load was determined by a pulse width modulation (PWM) servo signal sent to the motor controller with a typical setting

of 90% duty cycle. The difference in measured power between the electric motor and dynamometer is shown in Figure 4.1.
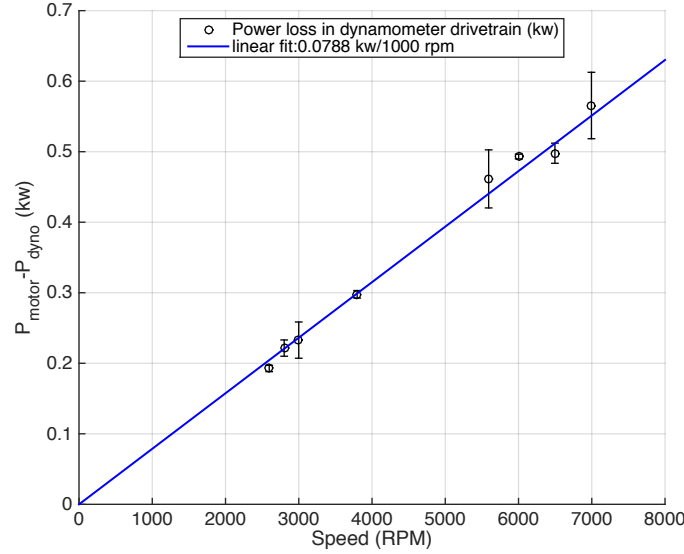
Figure 4.1. Difference between electric motor and dynamometer with trend line.

Significant vibration was encountered at specific speed ranges; between 3000 RPM and 3600 RPM as well as from 4000 RPM to 5000 RPM. These speeds were avoided for continuous operation to avoid damage to the components or overload to the load cell. Operation at higher speeds required a quick transition through these vibrational modes. Additionally, the slow acquisition rate led to aliasing in the force measurement when significant vibration was present. The vibration would be on the order of 50 Hz to 117 Hz, and corresponded to the speed of the motor. The low sampling rate did not pose a problem as the force due to the torque of the motor was nearly constant when the motor was on-condition. The strong DC signal from the torque was easy to detect and distinct from AC signal from the vibration.

A linear fit trend line, crossing at the origin, was found by taking the average of the element-wise division of the power values by the speed values. The slope was 78.8 watts per 1000 RPM and represented the power absorbed by the drivetrain as a

function of speed. This calibration corrects for friction in the dynamometer drivetrain; it does not represent internal friction of an engine and is specific to this experimental setup. A linear, zero-crossing function was expected since this friction was largely due to rolling friction in the bearings. Second order effects due to hydrodynamic viscous lubrication forces in the bearings were not observed.

The correction factor was applied to data previously collected for the 3W engines by Rowton et al. [22]. Recalling Equation 2.2, MEP is a linear function of power and speed. The drivetrain friction mean effective pressure was derived for an engine of known type and displacement in Equation 4.1.

$$\mathbf{FMEP_{drivetrain}} = \frac{\mathbf{Cn_R}}{\mathbf{V_d}} \tag{4.1}$$

Where the value C is the drivetrain friction correction factor and n_R is one revolution per cycle for two-stroke engines. Calculating a friction mean effective pressure in this manner reduces the power loss in the drivetrain for a given engine to a single value for all operating speeds. The $FMEP_{drivetrain}$ value would have been previously captured by TFMEP but now should be added to engine BMEP to increase measured brake power output. Table 4.1 shows the $FMEP_{drivetrain}$ calculated for each engine.

Table 4.1. Engine mean effective pressures recalculated with drivetrain friction included.

Engine	3W-28i	3W-55i	3W-85Xi
$FMEP_{drivetrain}$ (kPa)	153	78	50
$IMEP$ (kPa)	645	630	584
$BMEP$ (kPa)	595	575	524
$TFMEP$ (kPa)	49	55	60
η_m	92.4%	91.3%	89.7%

Mechanical efficiency was approximately 91% for all three engines once the drivetrain friction correction was applied. The engines tested did not have accessories like water pumps, oil pumps, or alternators, therefore, mechanical efficiency was a measure of the internal friction of the engine and was hypothesized to be similar between the set.

Brake power was corrected at each operating condition of the carbureted engine performance data originally collected Rowton [22], consistent with Equation 4.2. Figure 4.2 shows the corrected and uncorrected brake power values for all three engines across the operating range. The data is presented here is with respect to mean piston speed so the magnitude of correction at an x location depends on both speed and stroke length. Due to the small size and low output of the 28 cm^3 engine, the correction applied as a percentage of measured power was much larger than that applied to either the 55 cm^3 or 85 cm^3 engine.

$$\mathbf{P_b(N) = P_b(N)_{(uncorrected)} + CN} \tag{4.2}$$
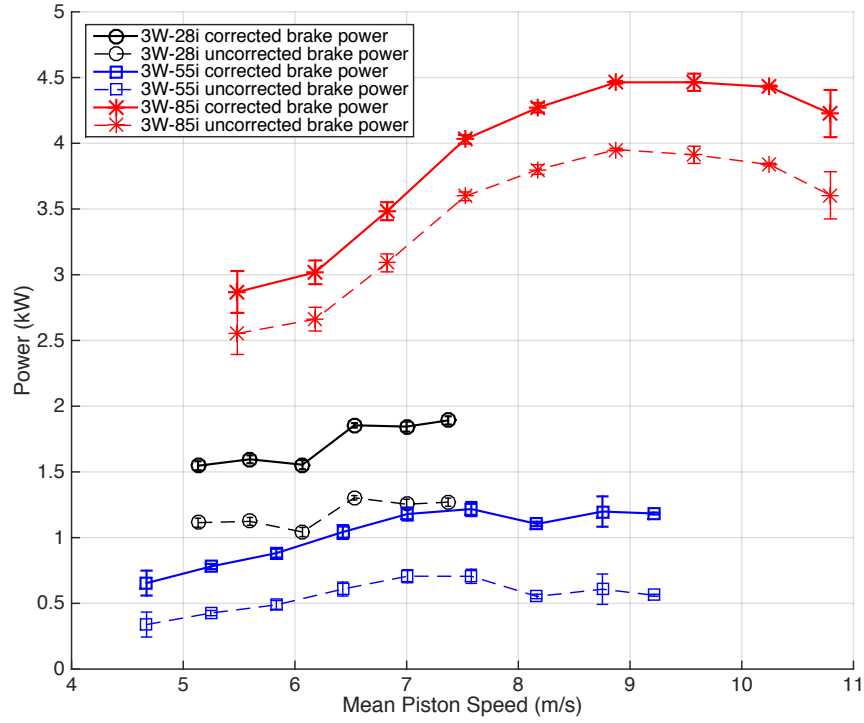
Figure 4.2. Full throttle brake power for three 3W two-stroke engines.

Brake fuel conversion efficiency provided insight into the effect of the power correction on each engine's performance data. Since this value was a measure of the brake power over the fuel consumed, a ratio of corrected brake power to uncorrected brake power was be applied to the data to correct it at every point, as in Equation 4.3.

$$\eta_{\mathbf{fb}}(\mathbf{N}) = \eta_{\mathbf{fb}}(\mathbf{N})_{(\mathbf{uncorrected})} \times \left[\frac{\mathbf{P_b}(\mathbf{N})(corrected)}{\mathbf{P_b}(\mathbf{N})(uncorrected)} \right] \tag{4.3}$$

Brake fuel conversion efficiency was higher at every point for all three engines. The magnitude of correction depended on the percentage of power absorbed by the drivetrain at a given speed. Figure 4.3 shows corrected and uncorrected brake fuel conversion efficiency for each of the three engines across the operating range. The 28 cm^3 and 55 cm^3 engines partially overlapped for brake fuel conversion efficiency where

they did not before the correction. On average, the 28 cm^3 engine was less efficient than the 55 cm^3 engine, but after the correction was applied, the deficit shrank significantly. Again this was attributed to the magnitude of correction relative to the output that was applied to brake power numbers for the 28 cm^3 engine. The 85 cm^3 engine had the highest brake fuel conversion efficiency.
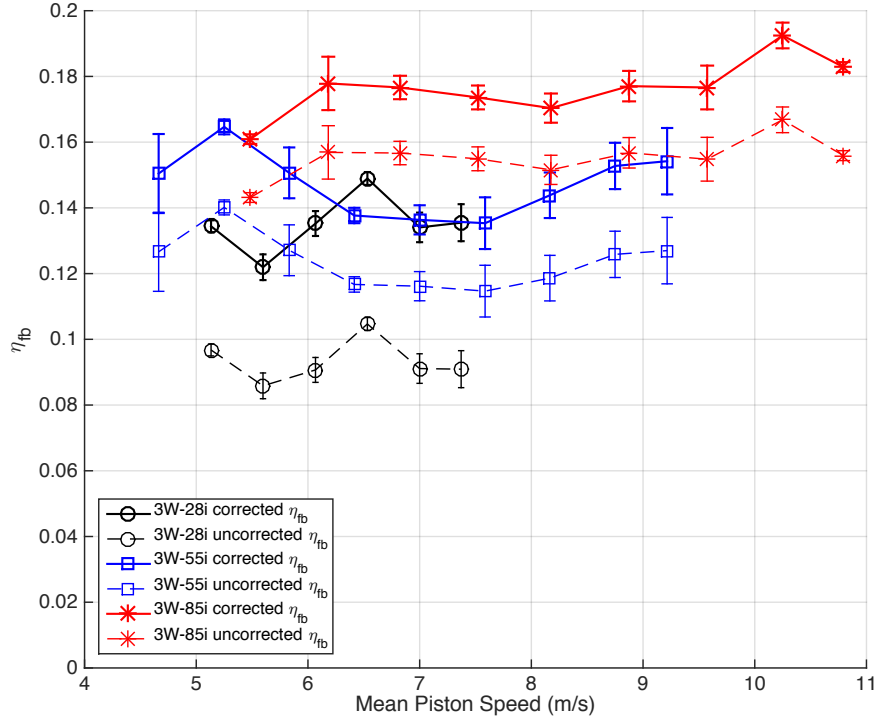
Figure 4.3. Full throttle fuel conversion efficiency for three 3W two-stroke engines.

Brake specific fuel consumption was also corrected, but the inverse correction was applied as shown in Equation 4.4.

$$\mathbf{BSFC(N)} = \mathbf{BSFC(N)_{(uncorrected)}} \times \left[\frac{\mathbf{P_b(N)}(corrected)}{\mathbf{P_b(N)}(uncorrected)} \right]^{-1} \qquad (4.4)$$

Figure 4.4 reveals similar trends where the improved BSFC was lower for all speeds in the corrected cases. The 28 cm^3 engine had a minimum BSFC of 544 $g/(kW-hr)$,

the 55 cm^3 engine had a minimum BSFC of 494 $g/(kW-hr)$, and the 85 cm^3 engine had a minimum BSFC of 422 $g/(kW-hr)$.
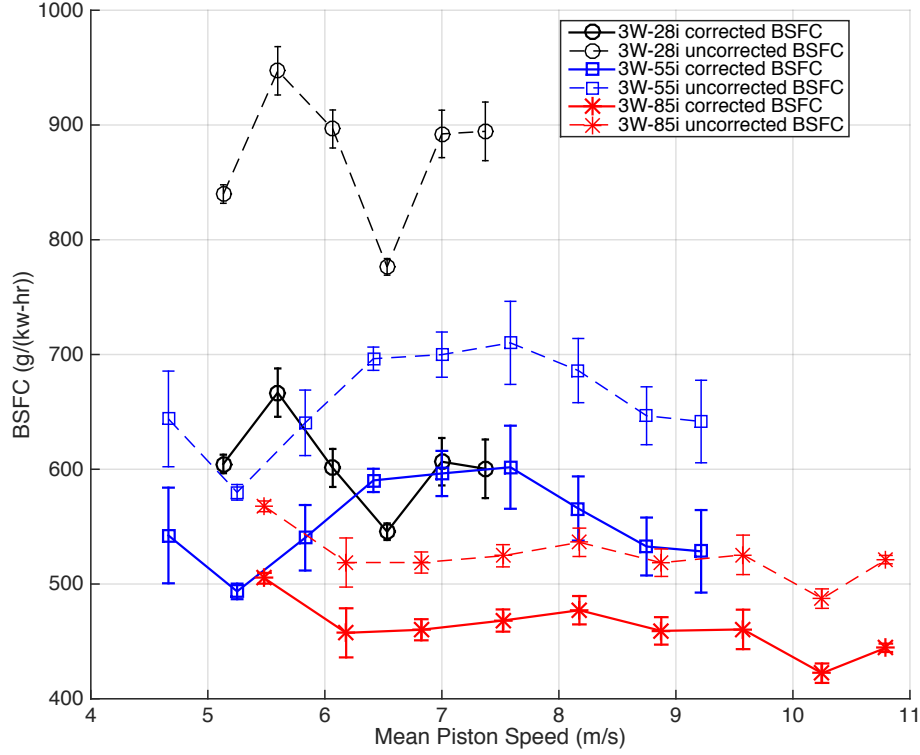
Figure 4.4. Full throttle brake specific fuel consumption for three 3W two-stroke engines.

The corrected performance parameters presented are more representative of the engines' true performance as tested on the small engine research bench. The performance parameters are summarized in Table 4.2 and compared to the manufacturer rated power.

Table 4.2. Corrected engine performance data.

Engine	3W-28i	3W-55i	3W-85Xi
Displacement (cc)	28	55	85
Rated power (kW)	2.5	3.9	6.8
Measured power (kW)	1.89	3.53	4.46
Specific power (kW/dm^3)	67.5	64.2	52.5
Fuel conversion efficiency (η_{f_b})	14.9%	16.5%	19.3%
WOT minimum BSFC (g/(kW-hr))	546	494	422

4.2 Conversion to Electronic Fuel Injection

The 55 cm^3 engine was converted to run with the electronic fuel injection system described in Section 3.2.1. This conversion was performed to maintain better control over engine operation at different speed and load settings than possible with the simple carburetors the engines were originally equipped with. It was therefore important to quantify the effect that the fuel injection system had on the performance of the engine and compare that to the output of the carbureted system.

Test points were chosen across the operating range and performance data was collected simultaneously with FTIR spectroscopy data collection to provide performance parameters associated with spectra collected. Testing was conducted at WOT and part throttle (PT). Part throttle was defined as nominally one half airflow of WOT at a given RPM. The airflows at each of the WOT operating points were recorded and halved for each of the PT operating points. Airflow was controlled by modulating the servo controlling the butterfly valve. It was found that the throttle valve had little authority over the airflow of the engine until it neared the closed state. The wide open throttle state occurred at a 1.200 ms digital servo pulse width and fully

closed throttle occurred at 2.000 ms. Part throttle data was typically taken at a 1.860 ms pulse width, with some variation depending on the engine speed. For both full throttle and part throttle tests, the ignition timing was set to maintain $CA_{50\%}$ at $8° \pm 0.5°$ ATDC as measured by the AVL combustion analyzer. An equivalence ratio of $\phi = 1.1 \pm 0.05$ was maintained through modulation of fuel injection duration. The full map of settings used to operate the 55 cm^3 engine are shown in Table 4.3.

Table 4.3. Fuel injected engine test matrix and settings map.

WOT						
Dynamometer (RPM)	4000	5000	6000	6500	7000	7900
Throttle Servo Pulse Width (ms)	1.200	1.200	1.200	1.200	1.200	1.200
Fuel Injector Pulse Width (ms)	4.700	5.000	5.200	5.500	4.200	3.200
Ignition Timing (degrees BTDC)	19.0	20.0	23.0	25.0	27.0	31.0
PT						
Dynamometer (RPM)	4000	5000	6000	6500	7000	7800
Throttle Servo Pulse Width (ms)	1.860	1.860	1.870	1.850	1.880	1.860
Fuel Injector Pulse Width (ms)	2.800	2.900	3.200	3.300	3.100	2.700
Ignition Timing (degrees BTDC)	17.0	19.0	21.0	23.0	25.0	27.0

For each run, the fuel injection settings were manually entered into the engine control software. The engine controller was not programmed with an operating map so it was required to step the engine between different operating points by progressively changing speed, fuel, ignition and throttle to reach at the desired point. Engine performance would fluctuate depending on operating condition and engine behavior. The settings were modified from the tabulated values as needed to maintain the desired equivalence ratio and $CA_{50\%}$ during the test. It is also important to note that

maximum speed for the PT condition was limited to 7800 RPM to avoid a long-period dynamometer harmonic at 7900 RPM.

4.2.1   Comparison of EFI and Carbureted WOT Performance.

Brake power output, shown in Figure 4.5 for the fuel injection configuration was reduced slightly from the carbureted configuration. Peak power occurred at 6500 RPM and fell off significantly at higher speeds. The 4000 RPM datapoint had higher power output on in the fuel injected configuration while 7900 RPM power was significantly reduced.
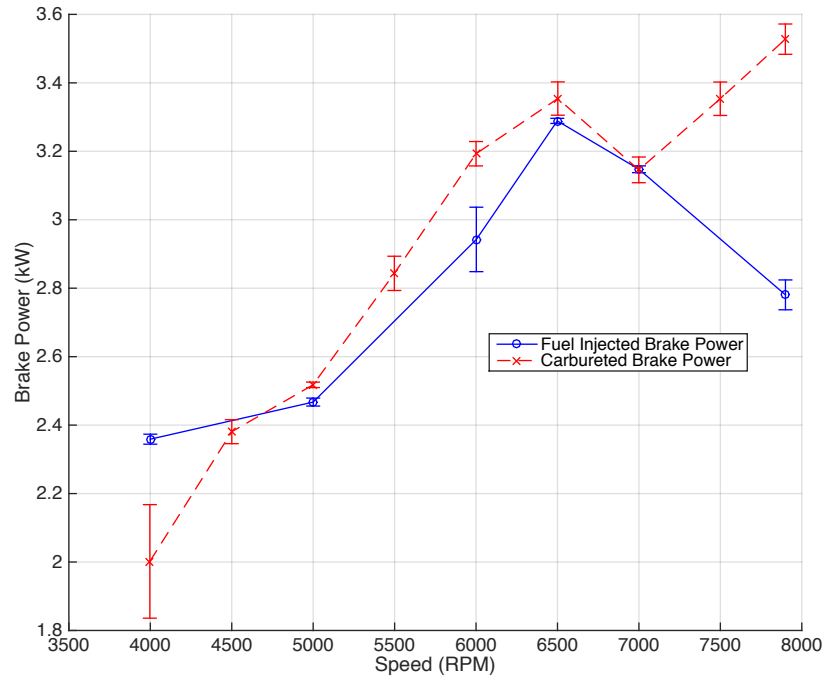
Figure 4.5. Brake power produced by the 55 cm^3 engine equipped with carburetor and EFI.

The carburetors originally equipped on the 3W engines were simple in design and had limited ability to precisely meter fuel. There were two needles available to adjust the high speed and low speed circuits and tuning required a fine touch to optimize. The fuel injection configuration provided precise control of fuel, within the ability to maintain a steady state condition as the engine performance drifted. For this series of tests, the engine was tuned by seeking an equivalence ratio, $\phi = 1.1 \pm 0.05$. Figure 4.6 shows that equivalence ratio was controlled within this band as compared to the carburetor which exhibited a step between low-speed and high speed operation. The box represents the target range for equivalence ratio.
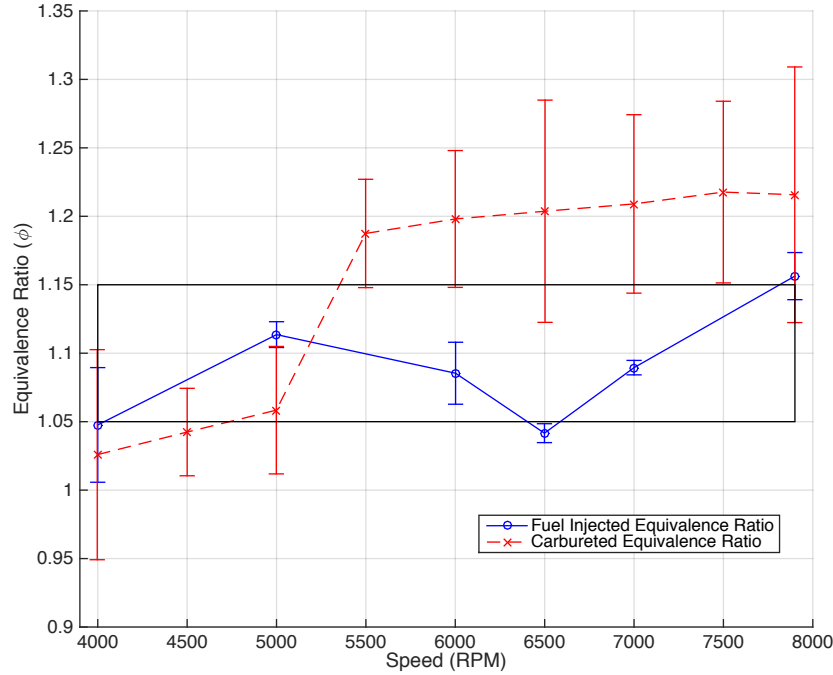
Figure 4.6. Equivalence ratio of the 55 cm^3 engine equipped with carburetor and EFI.

Brake fuel conversion efficiency was expected to improve significantly when the engine was equipped with EFI. The fuel injector was superior at atomizing the fuel in the intake charge, providing finer droplets and aiding combustion. Lower equivalence ratios, closer to stoichiometric for most of the operating range also reduced excess fuel in the cycle. With the exception of 4500 RPM, where no data was collected, the fuel injected configuration outperformed the carbureted configuration, as seen in Figure 4.7.
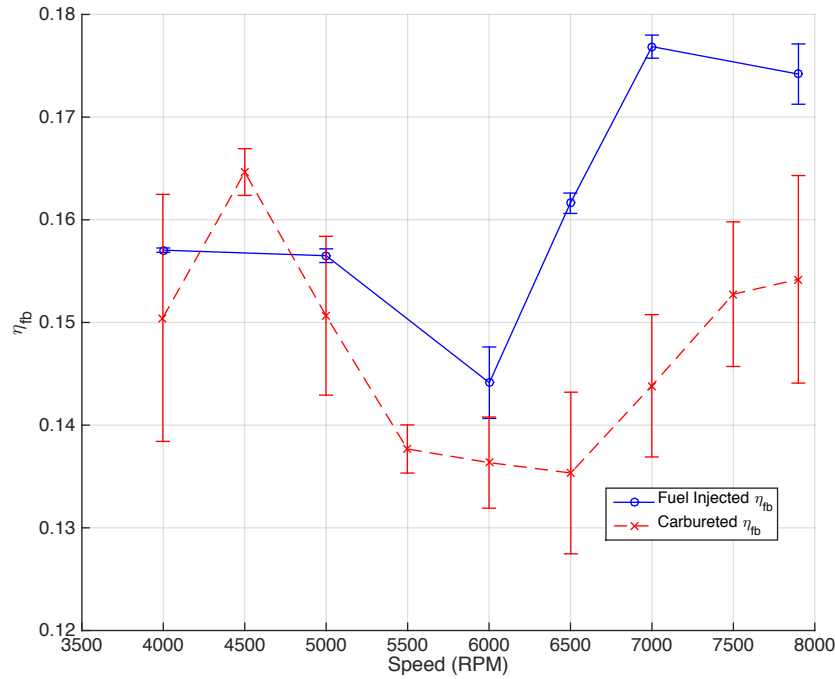
Figure 4.7. Brake fuel conversion efficiency of the 55 cm^3 engine equipped with carburetor and EFI.

Brake specific fuel consumption was compared between the two configurations as seen in Figure 4.8. It is mathematically related to the inverse of η_{fb} and has a similar trend.
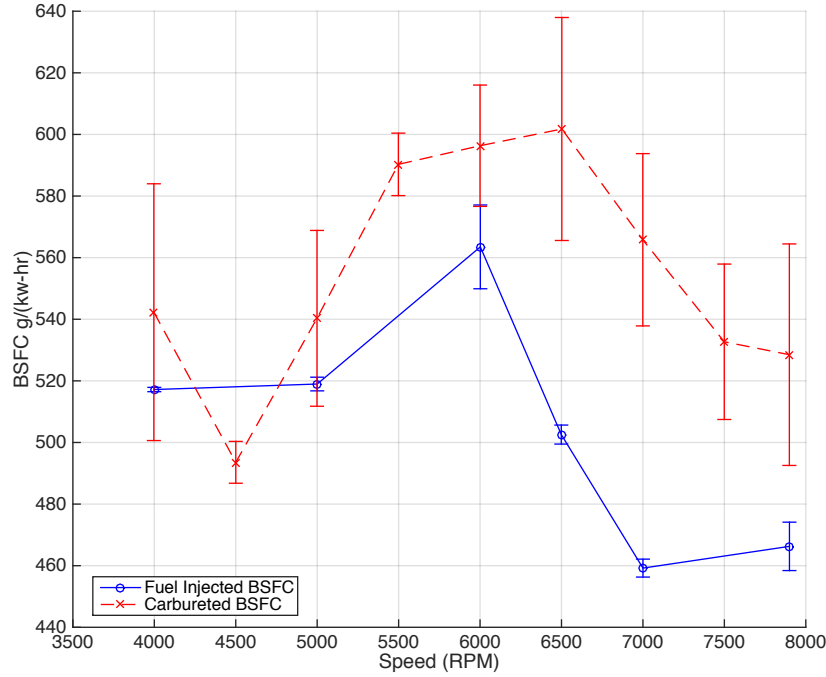
Figure 4.8. Brake specific fuel consumption of the 55 cm^3 **engine equipped with carburetor and EFI.**

The last parameter compared was delivery ratio (Λ). Delivery ratio was previously defined in Equation 2.10 with respect to the mass of intake air. Experimentally it was obtained as a function of mass flow rates for a simpler, unobtrusive measurements in real time. Delivery ratio is redefined in Equation 4.5 with the intake air mass flow rate, the speed of the engine, and the equation of state to determine intake air density.

$$\Lambda = \frac{\dot{m}_{intake}}{\rho V_d N} = \frac{\dot{m}_{intake}}{\frac{P_{intake}}{RT_{intake}} V_d N} \tag{4.5}$$

Delivery ratio is a measure of the effectiveness of the intake charging process of a

two-stroke engine and was calculated for both carbureted and fuel injected configurations, as is shown in Figure 4.9. A higher delivery ratio makes additional intake charge available to the engine for combustion. Delivery ratio is dependent on multiple dynamic effects that change as a function of speed so the behavior of this parameter can be highly variable. In a two-stroke engine, excess fresh charge, beyond what is required, will be lost through short circuiting into the exhaust. Both engine configurations exhibited similar behavior above 5000 RPM. The fuel injected configuration had a lower delivery ratio for all speeds except 4000 RPM, where both engines had ratios greater than one. Delivery ratios greater than one are possible in two-stroke engines because of the short circuiting phenomenon. This finding is supported in the literature, as found in Heywood and Sher [10], especially at off-design operating points. Delivery ratio can be used to model short circuiting in a two-stroke engine when combined with the measurement of additional engine parameters and assumption of an appropriate scavenging model [11]. The ability to determine delivery ratio is an important precursor for the determination of scavenging efficiency and short circuiting in an engine.
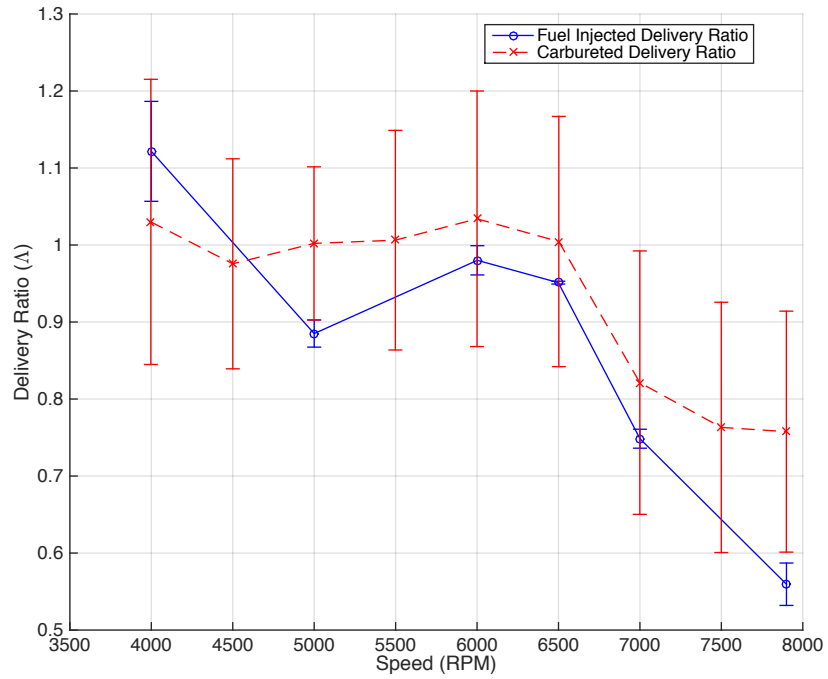
Figure 4.9. Delivery ratio of the 55 cm^3 engine equipped with carburetor and EFI.

The electronic fuel injection system installed on the 55 cm^3 engine was shown to maintain performance with respect to brake power while improving brake fuel conversion efficiency, and reduced BSFC. The ability to operate the engine with an electronic fuel injection system was demonstrated with a significant reduction in run to run variance, as shown by reduced error bars on the EFI performance data.

4.2.2 Part Throttle Performance.

Engine operability and performance at part throttle is important for usability of the engine in different regimes. In crankcase scavenged two-stroke engines, part throttle operation can be the most efficient operating point since pumping losses are reduced and there is less intake charge available to short circuit [10]. The 55 cm^3 engine was tested at PT to compare to the WOT data already collected. Part throttle data was defined as nominally one half of the airflow of the WOT conditions. Equivalence ratio was recorded at each of the operating points for WOT and PT conditions and is shown in Figure 4.10. The EFI system was able to maintain similar equivalence ratios between both throttle settings. The box represents the target range for equivalence ratio.
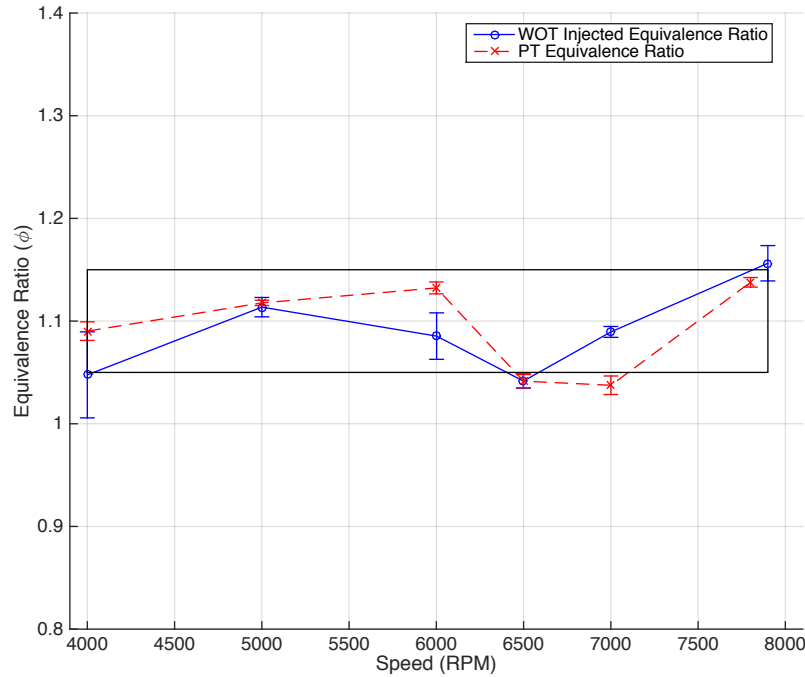
Figure 4.10. Equivalence ratio of the 55 cm^3 engine at WOT and PT.

Power at PT was reduced from the WOT condition; however, the power reduction was less than the roughly 50% reduction in measured intake airflow, and is shown with WOT power in Figure 4.11. Ratio of PT brake power to WOT brake power is represented by the black dashed line. The scale for this ratio is on the right hand axis of the plot. When averaged over the entire operating range, power was reduced 28% for a 47% reduction in intake air flow.
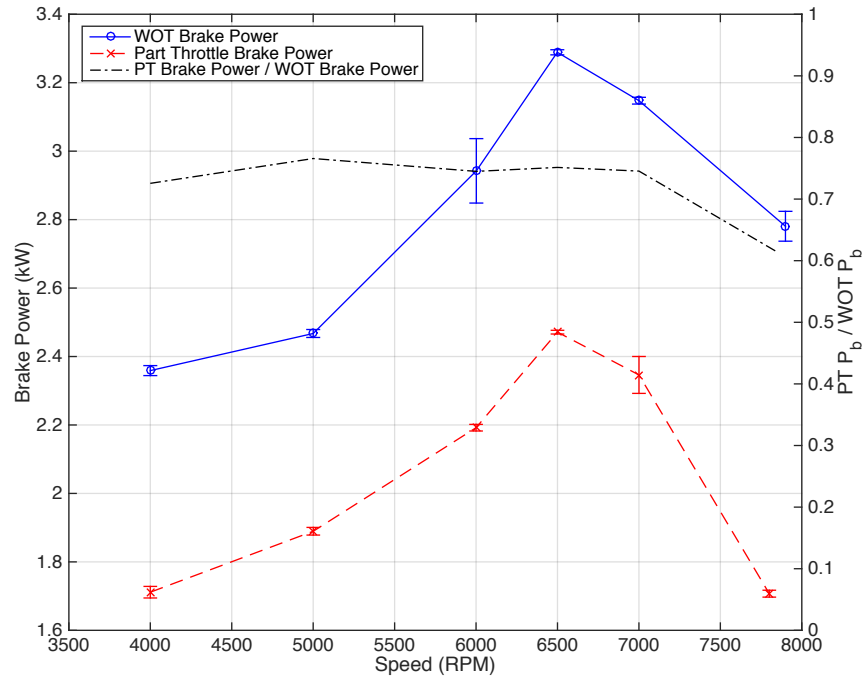
Figure 4.11. Brake power of the 55 cm^3 engine at WOT and PT.

Brake fuel conversion efficiency was increased significantly at PT conditions over WOT conditions, as shown in Figure 4.12. The increase in brake fuel conversion efficiency indicates that short circuiting was reduced significantly. Less wasted fuel due to reduced to short circuiting would increase brake fuel conversion efficiency since more of the fuel consumed contributes to useful work. Over the operating range, brake fuel conversion efficiency at PT was increased 36% over WOT.
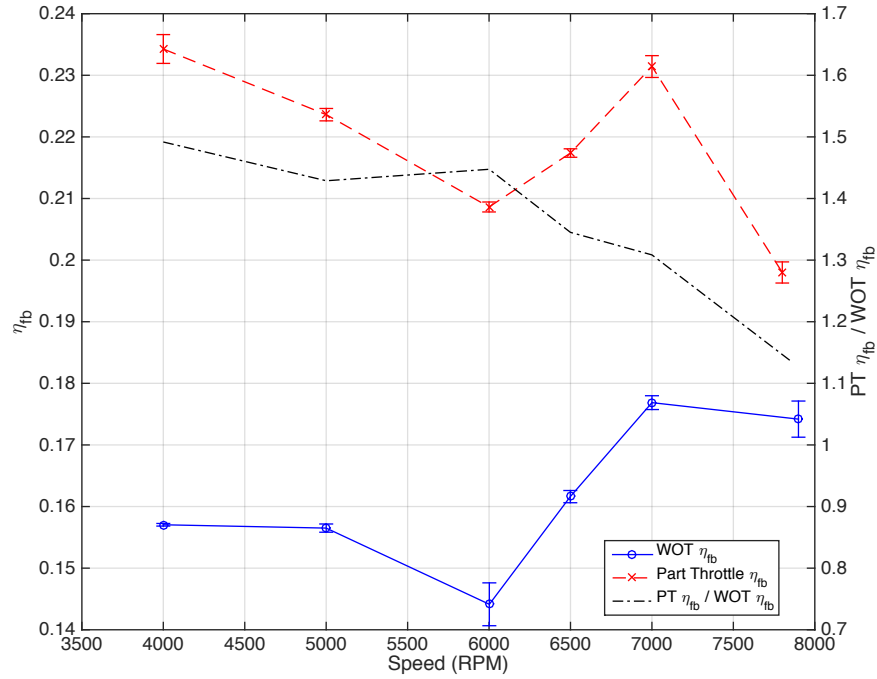
Figure 4.12. Brake fuel conversion efficiency of the 55 cm^3 engine at WOT and PT.

Brake specific fuel consumption is inversely related to brake fuel conversion efficiency and was improved by 26% over WOT conditions, as shown in Figure 4.13.
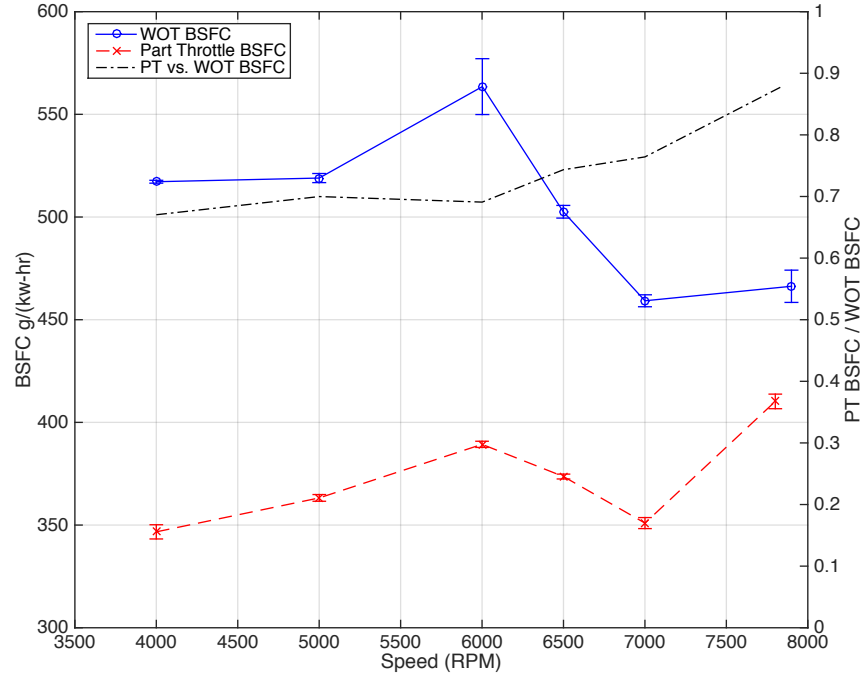
Figure 4.13. Brake specific fuel consumption of the 55 cm^3 engine at WOT and PT.

Finally, delivery ratio for the PT conditions was reduced by 47% over WOT conditions, as shown in Figure 4.14. It follows the same pattern as at WOT since the intake air flow measurement was used to define the half throttle condition.
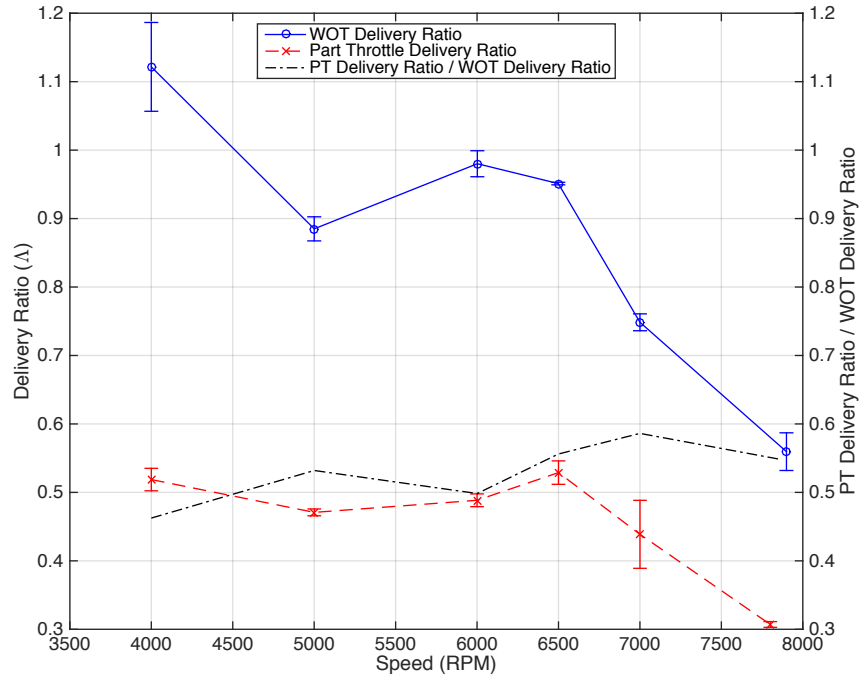
Figure 4.14. Delivery ratio of the 55 cm^3 engine at WOT and PT.

4.3 FTIR Spectroscopy Measurements of Exhaust Gasses

The following section discusses the results gathered from the FTIR spectroscopy measurements of the exhaust gasses. Two measurement techniques were attempted for the collection of this data; time-resolved step-scan and time-averaged linear-scan. The process of gathering data as well as the analysis and findings will be presented for each method.

4.3.1 The Instrument Response Function.

Tests conducted in both linear-scan mode and step-scan mode require a background spectrum to use as a reference. This background spectrum was used to find the absorbance of the sample and is representative of the instrument response function (IRF). The manner in which the background spectrum was collected is an important step required to obtain quality data. For consistency, a background scan was taken before the start of every test. After a test, used windows would be removed and the fixture cleaned of any residue using methanol. Cleaned windows and graphite gaskets to the steel fixture would be installed. The methanol used to clean the fixture and was detectable in the UHC absorbance band, between 3020 cm^{-1} to 2811 cm^{-1} by the FTIR spectrometer after reassembly. The CO_2, absorbance band from 2401 cm^{-1} to 2222 cm^{-1} was unaffected. The exhaust fan was run for up to 30 minutes before the baseline scan was obtained to clear residual vapors out of the exhaust manifold and optical probe. The nitrogen purge flowed during this time to evacuate the optical path outside of the probe. After the methanol had dispersed, a background scan was collected. This background was the average of 100 interferograms taken over the course of one minute at a resolution of 4 cm^{-1}. A typical interferogram collected as a background scan is shown in Figure 4.15. A background transmission spectrum showing the IRF is shown in Figure 4.16.
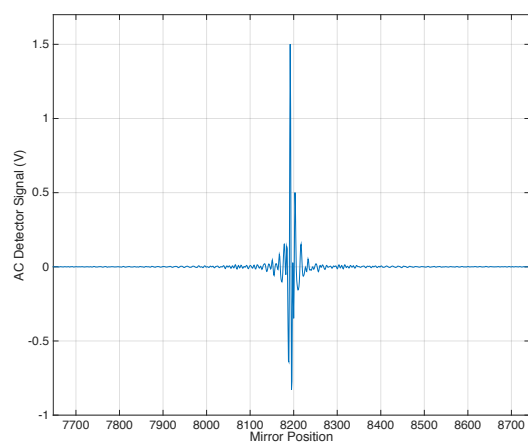
Figure 4.15. A typical interferogram collected in linear-scan mode.
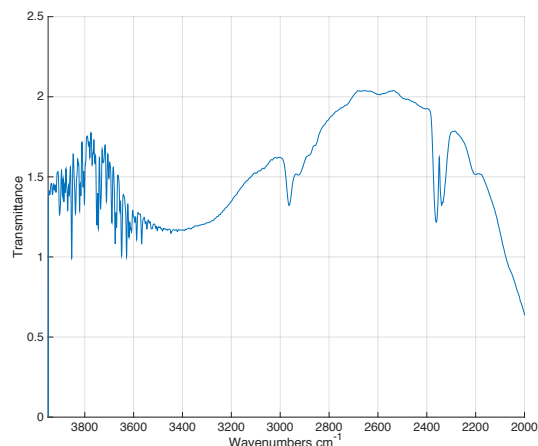
Figure 4.16. A typical background spectrum from the linear-scan interferogram.

During a test, carbon soot and UHC would accumulate on the sapphire windows. Carbon soot behaves similar to a blackbody and absorbs light uniformly across all wavelengths. The accumulation of soot on the windows would change transmission of the system so that a baseline collected in the start of a test would no longer represent the IRF. A simple simulation was performed to understand the effect of a gradual drop in transmission through the sample chamber due to soot accumulation on the windows. A background interferogram collected using the FTIR spectrometer was modified in this simulation. This data was representative of the IRF and was selected to minimize the number of independent variables. A linear, one-sided apodization function that started at unity and reduced in magnitude to 0.5 was applied to the data from one end of the interferogram to the other. The modified and original IRF interferograms were then processed into single beam transmission spectra. These spectra are plotted against each other in Figure 4.17. It can be seen that the simulated, sooted transmission spectrum shows less transmittance than the original. When these two spectra are divided by each other, there is a constant ratio for all wavelengths of light. No spectral information was lost in this process; only

the magnitude of the signal was reduced. The constant reduction of transmittance across all wavelengths allowed a simple correction to be applied to the data in either transmission form or absorbance without the loss of spectral information.
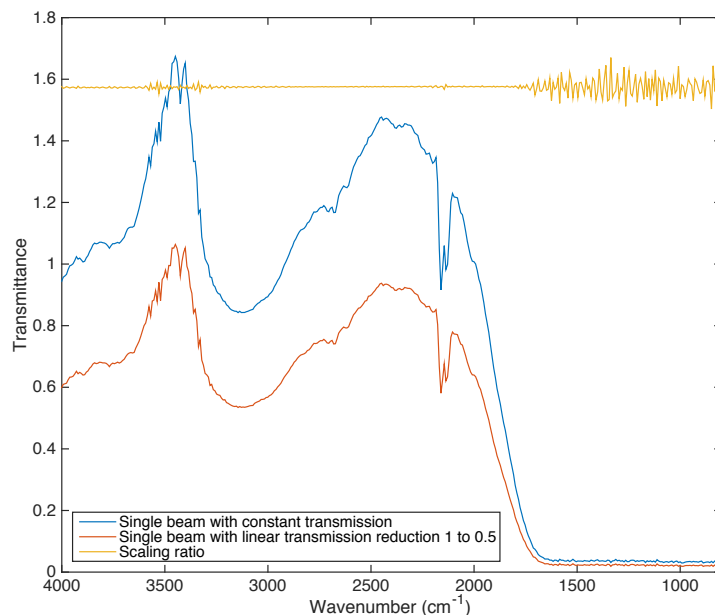
Figure 4.17. Simulation of the effects of broadband sooting on IRF transmittance.

When a sample spectrum was collected, the transmission of the sample was typically much smaller than the background. Once absorbance was found, the reduced power of the sample transmittance was corrected through the application of a baseline shift to the spectrum. A section of the absorbance spectrum with no absorbance information was found, from 2574 cm^{-1} to 2382 cm^{-1}. The level of absorbance in this band was selected as the reference for the absorbance baseline. The value of this section was averaged and subtracted from all points in the absorbance spectrum. A baseline shift of the absorption spectrum is mathematically identical to the multiplication of the sample's transmittance spectrum to a level consistent with the background, similar to what is shown in Figure 4.17. This is due to the logarithmic

nature of absorbance, as originally defined in Equation 2.22

Efforts were made to ensure repeatability in measurement of exhaust gas species concentration. Testing in step-scan mode showed that the sapphire windows would accumulate a coating of oil and soot over the duration of the test, which cause the IRF to differ from the background spectrum collected. The oil posed a significant challenge as liquid-phase hydrocarbons absorb strongly and are indistinguishable from the gas phase UHC which are being measured. Figure 4.18 shows a sapphire window and the window mounting assembly after removal from the optical probe with approximately 50 minutes of run time.
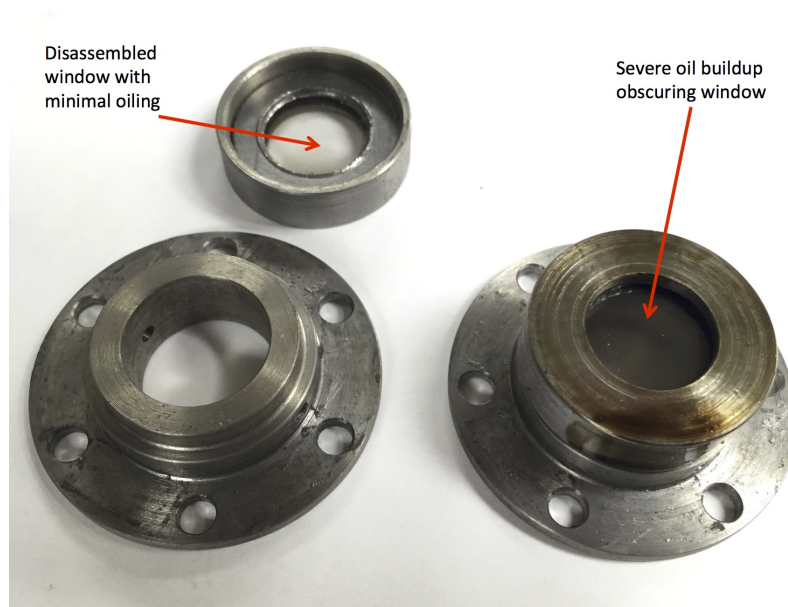
Figure 4.18. Sapphire window and window mounting assembly after a test showing oil buildup.

A test was performed to monitor the UHC measurements over time at a constant operating condition, 6000 RPM and WOT. The engine was run and the FTIR spectrometer was used to collect absorbance data at regularly spaced intervals for 1100 seconds. This speed and load setting exhibited some of the highest short circuiting for a worst case scenario of oil buildup on the windows. The operating point was

moved to 7000 RPM and 7900 RPM for the end of the test before the engine was stopped. Figure 4.19 shows the relative concentrations for this test with the time the engine was held on condition marked by the rectangle. The relative concentration for CO_2 is very steady, with a CoV of only 0.7%. On the other hand, the concentration of UHC has a CoV of 24.3% over this range.
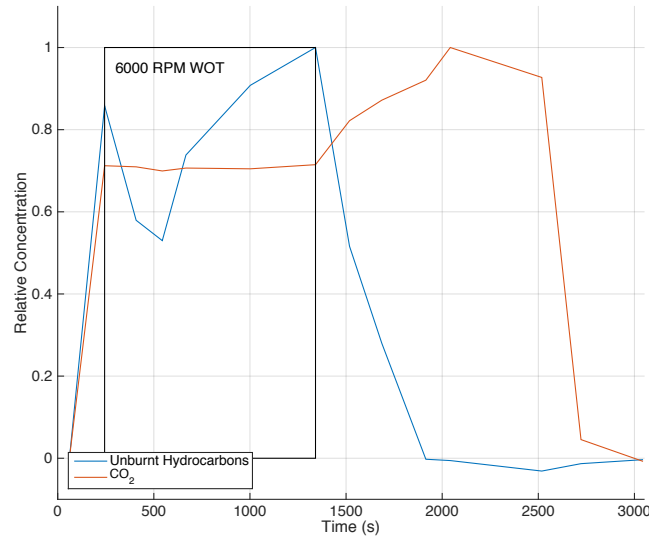
Figure 4.19. Relative concentrations over time of UHC and CO_2.

Relative concentrations, compared to the maximum of this test, were extracted using the method described in Section 4.3.4. The relative concentration of UHC wandered significantly. It was suspected that the temperature of the windows affected the affinity for the premixed lubricating oil and other UHC to adhere to the surface. When the engine was run at higher speeds later in the test, the measured relative concentrations of UHC was significantly reduced. The higher speeds had higher exhaust gas temperatures and significantly less short circuiting. It is hypothesized that these conditions allowed deposited UHC to burn-off so that no UHC was detected once the engine is shut off after 3000 seconds. It is clear that there is significant experimental uncertainty in measured relative concentration of UHC. The relative concentrations

for CO_2 were unaffected by absorbance in the UHC band so its value was used as a reference to ensure quality data was gathered and the measurements were consistent.

4.3.2   Crank-Angle Resolved Step-Scan.

The third research objective for this project was to develop a method for quantification of exhaust gas species with respect to crank angle degrees of the engine. Time-resolved step-scan was identified as a promising method to enable this measurement due to the ability to maintain the mirror at a stationary position with high precision. This differs from linear-scan modes where the mirror moves at a constant velocity and the detector signal is sampled at regular time intervals to collect the interferogram data. The fixed position of the mirror in step-scan mode allows a repeating process to occur and the detector measurements can be timed to the repeating process instead of the position of the mirror. This characteristic is ideal for internal combustion engines since their cycle of operation is a repeatable process with some variance.

The acquisition of spectral data using step-scan FTIR spectroscopy involves a complex series of events. The mirror was moved in discrete steps along the distance required by the desired spectral resolution. The FTIR spectrometer tracked the movement using the HeNe laser detector. The HeNe laser detector signal is a sinusoid centered on zero volts. The interferometer could stop the mirror at the zero crossing of the detector signal. The mirror remained fixed until commanded to move again by the data acquisition equipment. Figure 4.20 shows the sequence of events carried out for a short, 25 position, simulated step-scan experiment. The continuous interferogram is sampled only at discrete, widely spaced points. This produces a discrete approximation of the interferogram with widely spaced points at positions dictated by the interference fringes of the HeNe laser, which dictated a minimum

100

sample spacing of $\lambda_{HeNe}/2 = 316.5\ nm$. This simulation included a small number of points for simplicity; a real test sampled thousands of mirror positions to resolve the desired spectral resolution. The continuous interferogram is shown on this figure only as a reference for understanding of what is actually sampled by the mirror at the fixed points. The step-scan measurement does not capture the continuous information between the sample points.
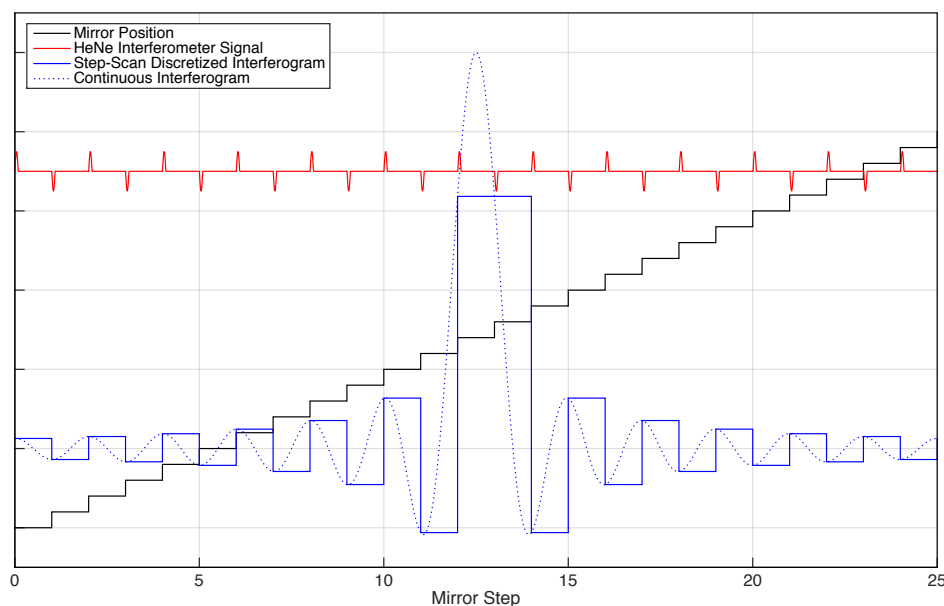
Figure 4.20. Simulation of a 25 point step-scan experiment.

The step-scan experiments allowed simplified data collection for the high-speed repeating process of the engine cycle. In these experiments, the engine position was tracked and a system of digital signals was exchanged between the data acquisition equipment and the FTIR spectrometer to coordinate the position of the mirror, as described in Section 3.3.2. To successfully complete the measurement, the number of mirror positions must be known. To sample the detector at every zero-crossing of the HeNe laser detector signal would require many thousands of points. To reduce

the burden of data collection, experiments with small spectral ranges can space the samples farther apart. Integer multiples of $\lambda_{HeNe}/2$ between one and nine were available for sample spacing. A sample spacing that is too high will cause spectral data to be lost, while a sample spacing too low extends the time required to make the measurement. Based on the information provided by the manufacturer, a sample spacing of four was chosen to allow the minimum number of mirror positions to be sampled while still allowing the desired spectral range to be resolved, up to 3950 cm^{-1}.

Unlike linear-scan measurements which produce two-sided interferograms, step-scan measurements are one-sided so that spectral data collection starts at the centerburst of the interferogram and proceeds to the wings. Sampling the one sided interferogram reduces the amount of time and mirror positions required to perform the measurement; however, the interferogram cannot be fully processed into a transmittance spectrum from this information. The Fourier transformed spectral information does not include the correct phase information in the output of a one-sided interferogram. The solution was to sample a smaller, symmetric interferogram around the centerburst and use the phase information produced by the Fourier transform to perform the Mertz phase correction on the larger, one-sided interferogram [7]. A symmetric, 256 sample interferogram was chosen for phase correction, which added 128 points before the centerburst. The required length of the interferogram was calculated to be 2208 samples at a sample spacing of four and including the phase correction samples.

To increase SNR of the measurement, 100 engine cycles at each mirror position were recorded to minimize the effect of cycle to cycle variation on the averaged interferograms. Table 4.4 shows the calculated data acquisition times at the various operating speeds of the engine. Long duration measurements were required to collect the vast amount of data needed to make a measurement.

Table 4.4. Estimated step-scan data collection times.

Engine Speed (RPM)	4000	5000	6000	6500	7000	7900
Mirror Steps	2208	2208	2208	2208	2208	2208
Estimated Collection Time (s)	3312	2649	2208	2038	1893	1677

4.3.2.1   Step-Scan Data Collection and Processing.

Data collection for the step-scan mode was difficult due to the long duration required for tests. Several challenges were encountered during engine operation that precluded the collection of quality data. Alignment of the optics was a difficult to maintain over the length of the test. The optical breadboard base provided adequate stability for the optics but the intense vibration of the engine would unseat the adjustment screws and misalign the optics. The fiber connectors would also become unseated and lose focus. Blue grade threadlocker was applied to all of the threaded and removable fixtures on the optical setup which securely held the optics in place.

To test the step-scan system, a test was performed at 6000 RPM. A full length test was conducted to gather data and determine the quality of the measurement. This dataset was used to develop the MATLAB based data processing algorithm. The raw data that were recorded by the data acquisition equipment were saved in a binary file which was first read into memory and compressed. This data was read serially and the analog detector signal was sorted based on mirror position, encoder position, and engine cycle. The 100 engine cycles sampled for each mirror position were averaged into the crank-angle resolved interferograms and prepared for Fourier transform processing. The processing algorithm formatted the crank-angle resolved interferograms to be visualized as a 3D surface that can be viewed and manipulated by the user. An abridged example crank-angle resolved interferogram surface with

centerburst is shown in Figure 4.21 and Figure 4.22.
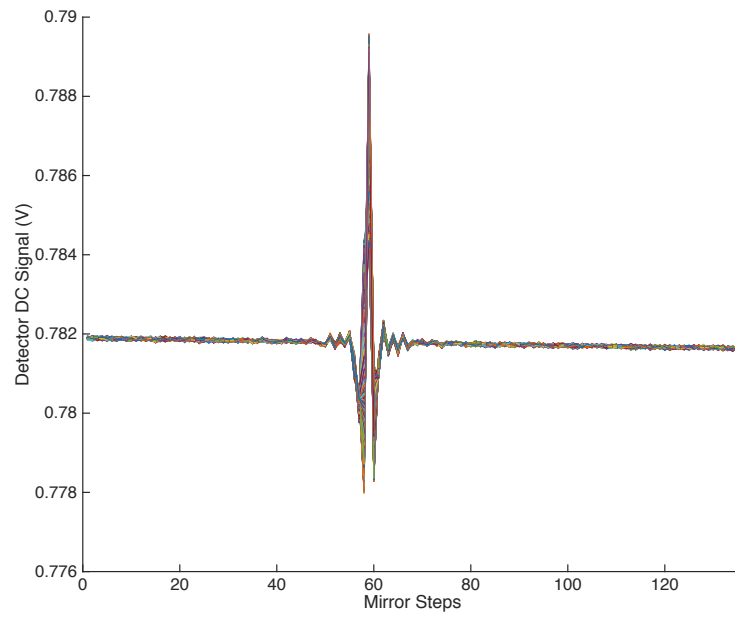
Figure 4.21. Profile view of crank-angle resolved interferogram surface showing interferogram detail.
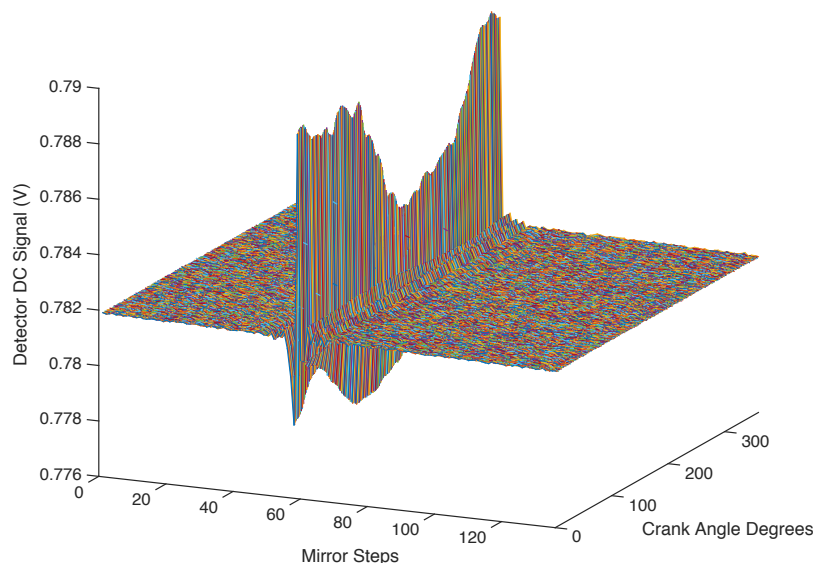
Figure 4.22. Alternate view of crank-angle resolved interferogram surface showing detail of angular resolution.

The Fourier transform algorithm followed the conceptual flow described by Griffiths and de Haseth for processing interferograms [7]. This algorithm first applied apodization to the interferogram with the apodization function centered on the centerburst. The Norton-Beer strong apodization function was applied to the data to duplicate the processing performed by the FTIR spectrometer software. The general form of this equation and its coefficients are documented in Section 2.3.3.1.

A fast Fourier transform was performed on the interferogram after apodization. The complex FFT output was phase corrected using the Mertz phase correction described in Section 2.3.3.2. The phase information came from the phase information extracted from the smaller, symmetric interferogram. This process produced a single beam transmission spectrum for each of the individual crank-angle bins. The transmission spectra for the sample and background were then processed for absorbance.

4.3.3 Step-Scan Results and Troubleshooting.

After the data from the initial test was fully processed, it was observed that the magnitude of the interferogram signal was very weak with significant levels of noise. The first 120 points of the interferogram are shown in Figure 4.23. These data are presented in the same way as those in Figure 4.21, yet the interferograms are very different in appearance. There was no identifiable centerburst in the crank-angle resolved dataset even though the centerburst was passed at mirror step 135. Some additional signal was detected at this point but it was small compared to the rest of the noise. This result began a process of troubleshooting to better understand why the signal was diminished compared to that observed through the linear-scan operation.

Figure 4.23. Interferograms from the first crank-angle resolved step-scan test presented with respect to mirror position.

106

The crank-angle resolved interferograms were Fourier transformed to extract spectral data. The spectra are presented with respect to CAD in Figure 4.24. It is clear that no spectral data could be recovered from the collected interferograms as the spectra are dominated by noise in this case.
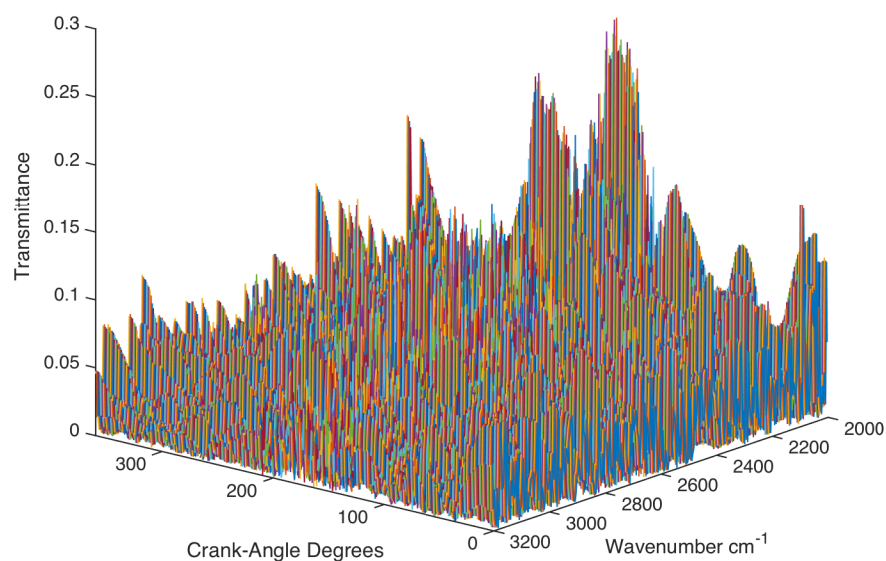
Figure 4.24. Spectra from the first crank-angle resolved step-scan test presented with respect to CAD with no identifiable spectral data.

In Figure 4.25, it appeared that broadband absorbance information was captured by the detector, when viewed with respect to CAD. The features shown in the detector signal were repeatable and lasted for the duration of the test. During another test of the step-scan system, the optics became mis-aligned so that no light was being transmitted through the system. The same angular resolved feature was seen in this errant case. It was determined that electronic noise from the ignition coil was being picked up by the detector and was producing this pattern.
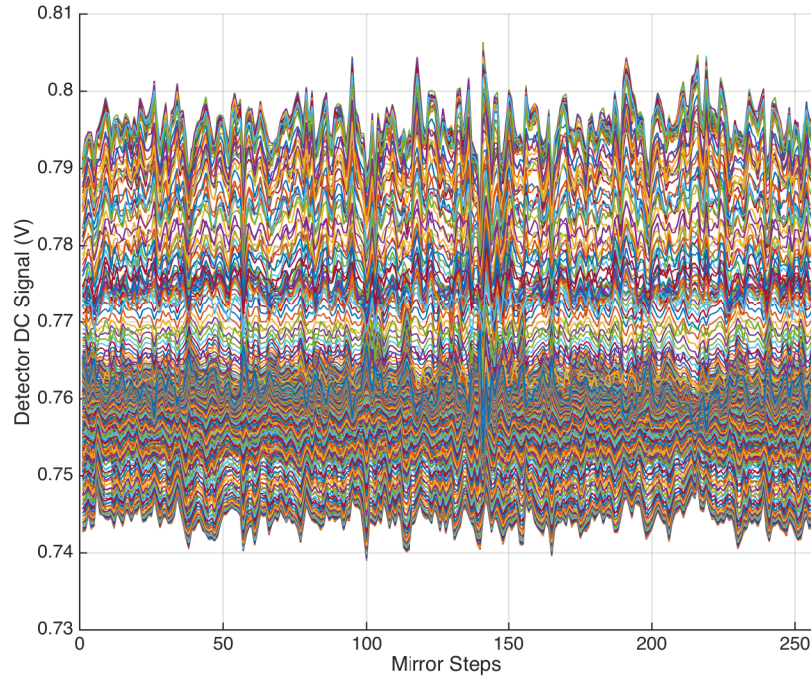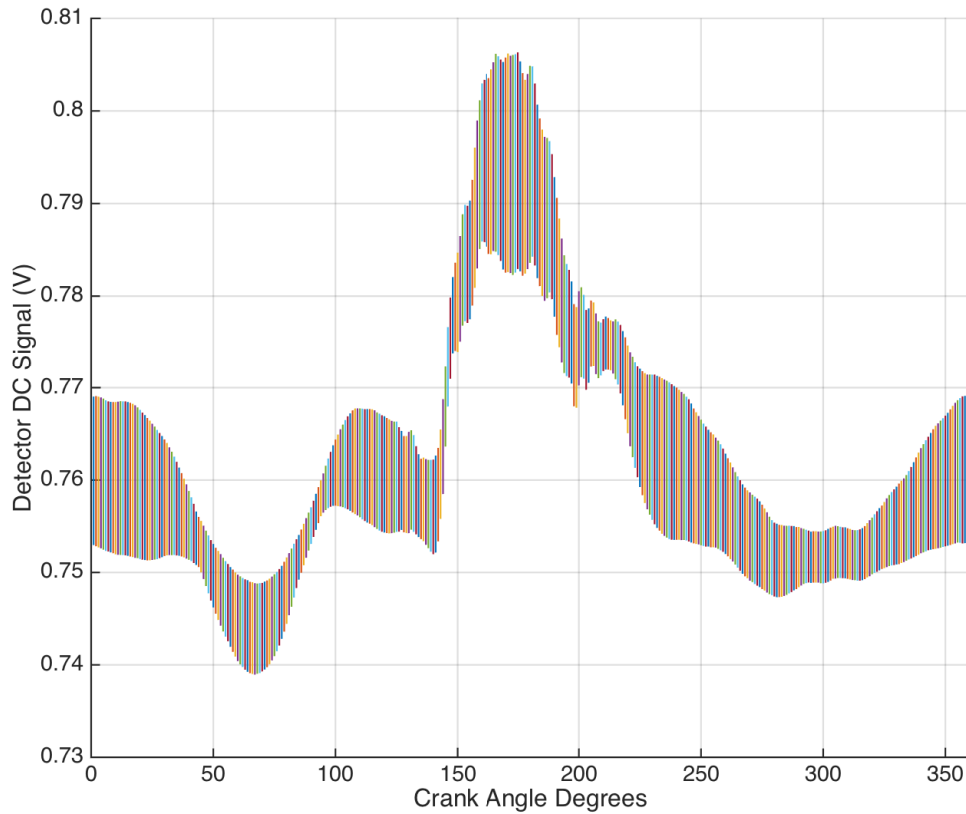
Figure 4.25. Interferograms from the first crank-angle resolved step-scan test presented with respect to CAD.

All of the crank-angle resolved interferograms were averaged into a single, time-averaged interferogram to provide more insight into the quality of the signal and are shown in Figure 4.26. The average of all interferograms was hypothesized to provide a significant increase in SNR. Even with this advantage, the data were dominated by noise and the peak to peak magnitude of the centerburst was only approximately 6 mV. Figure 4.26 presents the time-averaged step-scan interferogram on the same scale as a typical linear-scan step-scan interferogram for comparison. The linear-scan interferogram was collected using an AC coupled analog signal so the DC offset has been filtered. It is clear that the level of signal is several orders of magnitude less

108

than that collected during linear-scan data acquisition.
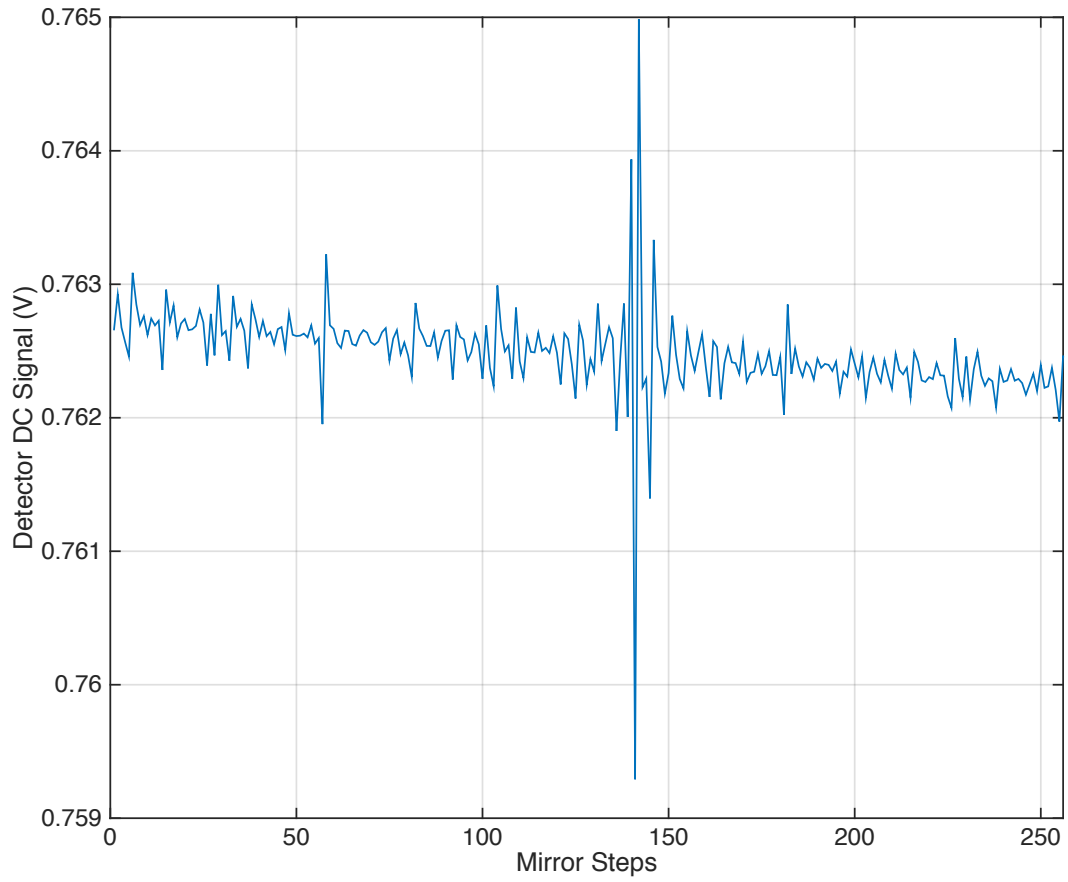
Figure 4.26. Time-averaged interferogram from the first crank-angle resolved step-scan test with very low signal.
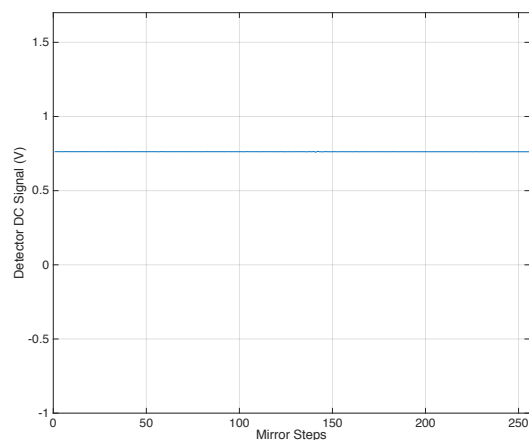
Figure 4.27. Time-averaged interferogram collected in step-scan mode on common voltage scale.
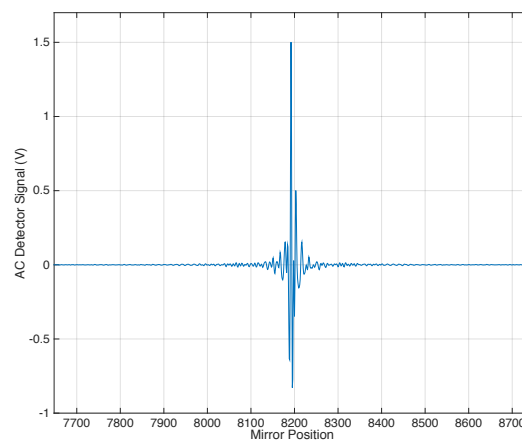
Figure 4.28. A typical background interferogram collected in linear-scan mode on common voltage scale.

Figure 4.29 shows the time averaged spectrum extracted from the mean of all collected interferograms. This is compared to the background interferogram presented earlier but shown in Figure 4.30. Even with the increase in SNR that comes from averaging spectra collected over all CAD, there is no identifiable information in this single beam spectrum.
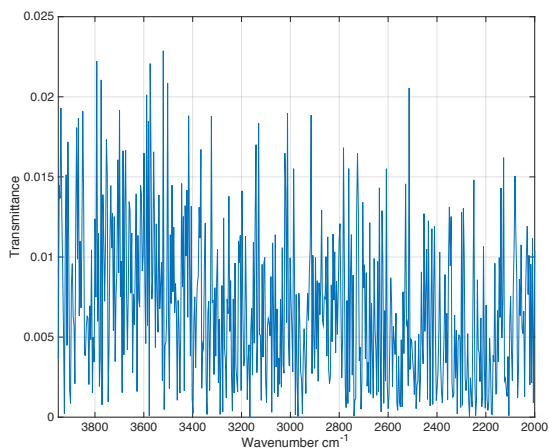
Figure 4.29. Time-averaged spectrum from a step-scan test with no identifiable spectra data.
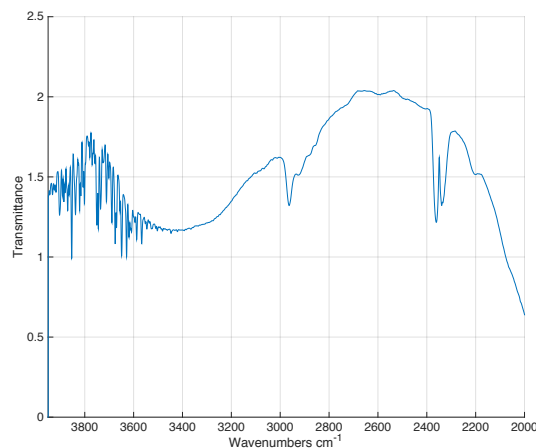
Figure 4.30. A typical background spectrum from a linear-scan interferogram.

The low SNR observed in the collected data initially led to a hypothesis of high electrical noise dominating the signal. To combat this, new cables were run between the MCT detector and the data acquisition equipment. A high-quality, coaxial cable with an additional grounded shielding jacket was installed to carry the analog signal. This did reduce the noise floor, but it did not increase the peak to peak magnitude of the interferogram. While troubleshooting, the analog detector signal was sampled in linear-scan mode by a high-speed scope to analyze the signal. This signal showed a 2.0 V peak to peak magnitude on centerburst. The difference in the continuous analog signal from the detector does not change if the device is used in step-scan or linear-scan so this strong signal seen in linear-scan mode should be the same signal produced by step-scan mode.

The wide sample spacing used in step-scan measurements was suspected to be aliasing out spectral data. Figure 4.31 shows the centerburst from a step-scan test with a sample spacing of four and it is clear that the periodic signal is under-resolved. It was decided to run additional tests with the minimum sample spacing to see if additional signal could be resolved. A sample spacing of one is impractical from a standpoint of running the engine as it will quadruple the number of mirror steps and time required to gather the data. For the purposes of troubleshooting, only the centerburst needed to be captured to determine the effect of the change in sample spacing. This provided enough information to understand the effect on measured signal strength. The output of the quadrature encoder was simulated so that troubleshooting tests could be run with the engine off since they rely on the external clock. The engine was not operated to reduce the amount of variables to consider when troubleshooting.

Figure 4.32 shows the centerburst from a test with a sample spacing of one. The peak to peak magnitude of 22 mV was significantly higher than the 7.5 mV seen in the

wider sample spacing tests. Also, more oscillations are seen around the centerburst. Even with a sample spacing of one, the samples are spaced too far apart relative to the periodic function of the interferogram and this wide spacing contributed to aliasing of the signal and the loss of spectral information. It is important to note that the sample spacing of one is the minimum available value and represents an optical path difference per step of $\lambda_{HeNe}/2 = 316.4 \ nm$ between points. A smaller interval is not available due to the way in which the mirror is tracked. Both Figure 4.31 and Figure 4.32 have the same spectral resolution and represent the same physical traverse of the interferometer mirror; the steps in Figure 4.31 are four times larger than those in Figure 4.32. Without aliasing, the same interferogram would be seen in both figures.
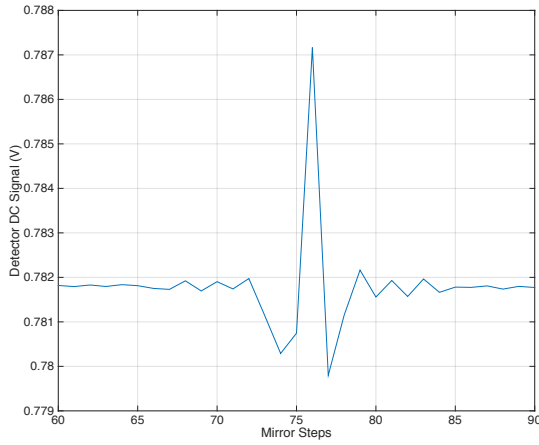
Figure 4.31. Sample spacing of four with severe aliasing.
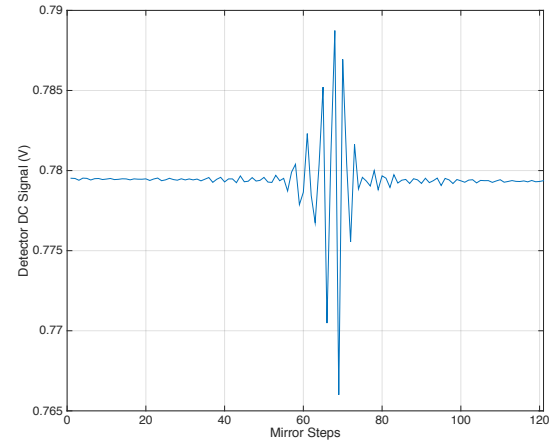
Figure 4.32. Sample spacing of one with reduced aliasing.

The sample spacing of one was able to resolve more of the signal; however, the true peak to peak magnitude of 2.0 V at the centerburst remained aliased. There is no way to further reduce the length of the mirror step or change the relative sampling locations of the mirror beyond what was already explored. The nature of step-scan mode requires a very high signal strength to overcome the limitations of mirror positioning and the inherent poor SNR. This type of measurement was not

well suited to the limited signal strength of a fiber coupled measurement. It was decided that further testing in time-resolved step-scan mode would not be attempted because of these limitations.

4.3.4 Time-Averaged Linear Scan.

After the unsuccessful attempt at step-scan data collection, a time-averaged linear-scan mode was used. This method of data collection was implemented using the standard data acquisition tools included in the FTIR spectrometer including the internal ADC and processing software. This method revolved around the linear-scan data collection technique, where the interferometer mirror moves continuously in one direction at a constant velocity. The mirror is tracked by the HeNe laser interferometer signal and the detector is sampled at regular spacings of the mirror. The constant speed of the mirror allows for sampling of the detector at additional mirror positions not possible in the step-scan mode, since it is not limited by ability of the interferometer to stabilize the mirror at a fixed position. A typical linear-scan test would sample 16384 interferogram points, compared to 2208 for the step-scan measurement of the same resolution. The additional sampled mirror positions in linear-scan mode contributes to high measurement fidelity and improved SNR over step-scan mode.

The mirror required a finite amount of time to traverse the distance specified by the measurement resolution. A resolution of 4 cm^{-1} was selected which required a mirror traverse of 0.25 cm. To properly time-average the signal, 100 scans were collected and averaged. The mirror would traverse the scanned distance in 300 ms and return to the start over an additional 300 ms. At this resolution, the spectrometer was able to make the 100 scans in 61 seconds. Table 4.5 shows the number of engine cycles sampled over the course of the measurement.

Table 4.5. Engine cycles observed by linear-scan tests.

Engine Speed (RPM)	4000	5000	6000	6500	7000	7900
Mirror Scans	100	100	100	100	100	100
Engine Revolutions	2033	2542	3050	3304	3558	4015

The linear-scan interferograms were averaged into a single interferogram and then Fourier transformed to produce a single-beam transmission spectrum, as shown in Figure 4.33. A series of three linear-scan tests were performed within the first 10 minutes of operation for each speed and throttle setting tested. These tests were conducted two minutes apart. To attempt to minimize variance during testing, the single beam spectra were monitored during collection so that data was collected once transmission in the UHC band had appeared to stabilize. The engine performance was recorded using the low speed data acquisition setup as well as the high speed combustion analyzer setup described in Section 3.1. Before the test, a single beam transmission spectrum was recorded with clean sapphire windows installed. This spectrum was used as the background scan for all measurements at an operating condition. For primary data collection, three separate samples were taken at each operating condition, from 4000 RPM to 7900 RPM at WOT and PT. Examples of the background transmission spectrum as well as the three sample transmission measurements are shown in Figure 4.33. It can be seen that significant differences in transmittance exist between the three sample scans; however, these were corrected through a baseline shift of the absorbance spectrum, as discussed in Section 4.3.1.
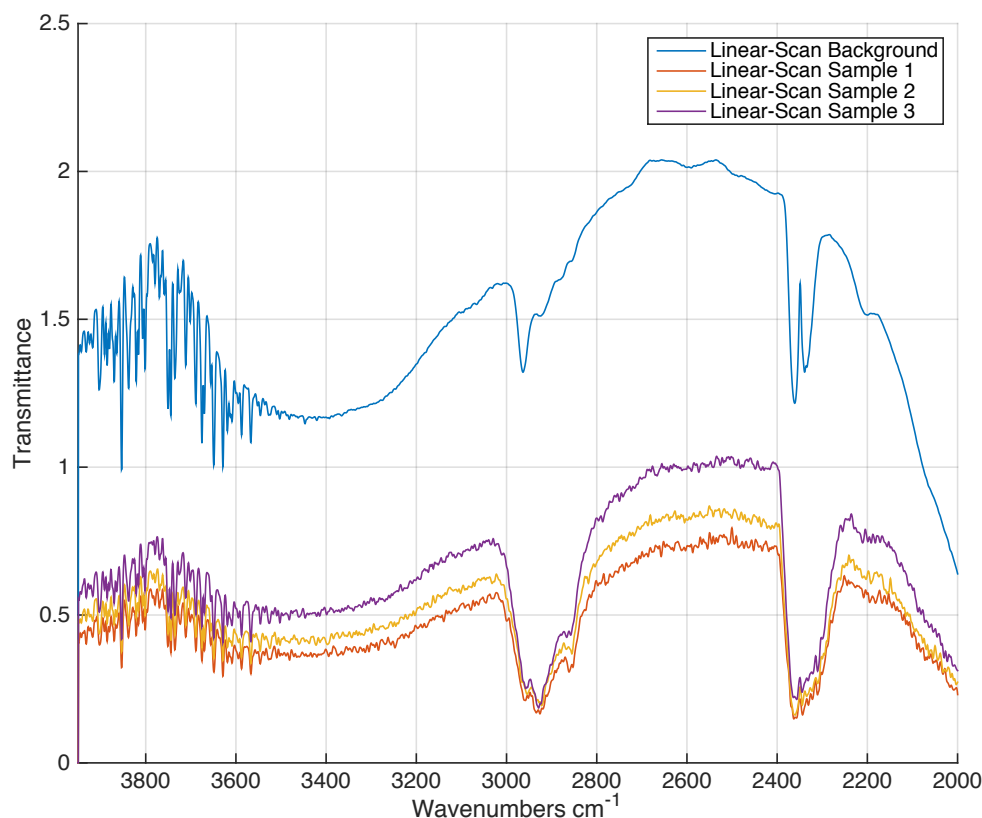
Figure 4.33. Linear-scan single beam background and sample spectra collected at 5000 RPM and WOT.

The absorbance spectra were found by using Equation 2.22, in the manner described in Section 2.3.1. Differing levels of power in the transmission spectra were corrected by setting the portion of the spectrum between the HC absorption band and CO_2 absorption band to zero absorbance. Due to the logarithmic properties of absorbance, a simple additive baseline shift of the absorbance spectrum is equivalent to multiplying the single beam transmission spectrum back to a consistent level with the baseline. Figure 4.34 shows the absorbance spectrum of the three samples recorded at WOT and 5000 RPM after the absorbance spectra had been baseline shifted to correct for differences in transmission seen in Figure 4.33. The relative

concentrations of both CO_2 and UHC were found by numerically integrating the area under the curve. The limits of integration for each substance corresponded to to the absorbance band of that substance in the mid-IR range. The blue rectangle shows the limits of integration for CO_2, from 2401 cm^{-1} to 2222 cm^{-1}, and the red rectangle shows the limits of integration for UHC, from 3020 cm^{-1} to 2811 cm^{-1}.
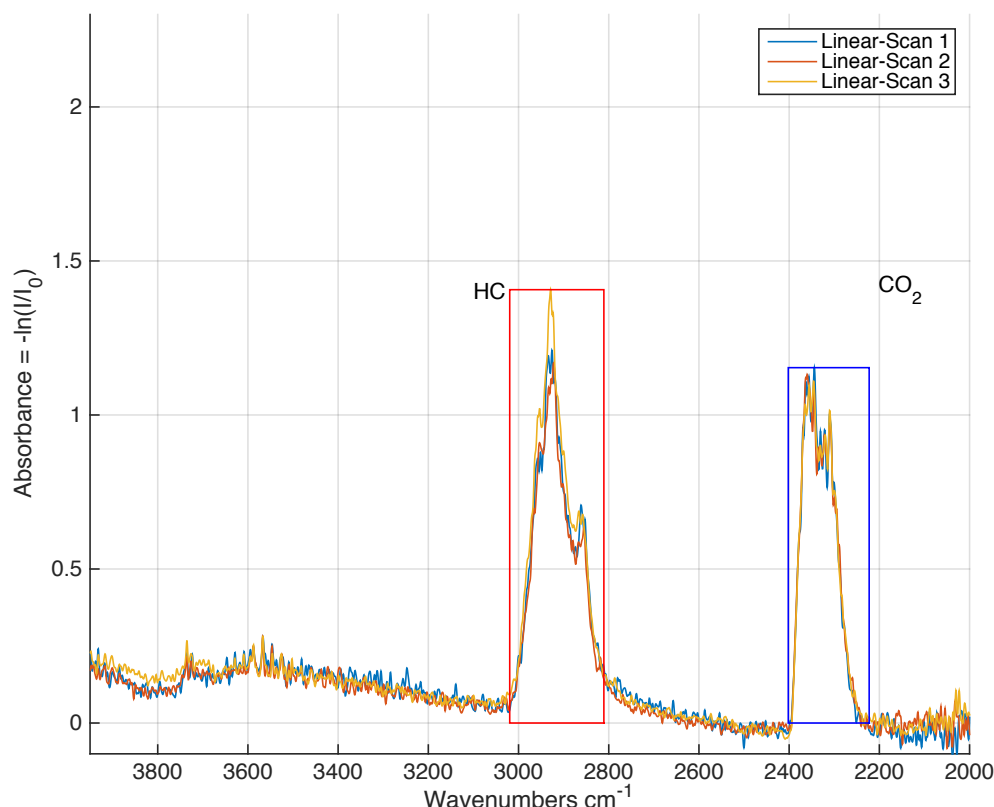
Figure 4.34. Absorbance spectra collected at 5000 RPM and WOT.

The integrated areas within the chosen absorbance bands were averaged at each operating condition. The integrated areas inside the absorbance bands were normalized by those at the reference condition of peak power at 6500 RPM and WOT to produce relative concentrations. These concentrations are not absolute molar values but they are directly proportional to the molar concentration of the substance

116

according to Beer's Law.

Figure 4.35 shows the relative concentration of UHC and CO_2 in the exhaust at WOT. Higher speeds show decreased levels of UHC in the exhaust. Delivery ratio was plotted on the same scale to show the correlation with the amount of fresh charge delivered to the engine. It is clear that the level of unburnt UHC is elevated at higher delivery ratios. This shows that short circuiting is closely related to delivery ratio. The relative concentration is reduced at high RPM as delivery ratio decreased, indicating reduced short curcuiting. If combustion efficiency is assumed to remain constant at all speeds, the increase in CO_2 concentration can be attributed to reduced dilution of the combustion products by fresh charge in the exhaust. Equivalence ratio and combustion phasing are two of the main factors that control combustion efficiency in ICE [9] and both of these parameters were tightly controlled in this experimental setup. The error bars on relative concentration represent the standard deviation calculated from the three, time-averaged scans taken at each operating condition and is indicative of the sample to sample variation observed during each test.

Included in the figure is an estimate of short-circuiting made by Ausserer et al. using a combination of gas chromatography (GC) methods [1]. Sample bags were filled with exhaust from the same 55 cm^3 engine at the same conditions used for the FTIR spectroscopy measurements for engine speed, throttle setting, equivalence ratio, combustion phasing, and operating temperature. Short circuiting estimates were developed using the average of the gas chromatography - mass spectrometry (GC-MS) and the gas chromatography - thermal conductivity detector (GC-TCD) methods to measure the absolute concentrations of unburnt hydrocarbons in the exhaust. This data was fed into an energy balance to provide the short circuiting ratio (R_{sc}) at each operating condition. The estimates for short circuiting ratio at each speed were normalized against the measured $R_{sc} = 58\%$, at WOT and 6500 RPM for comparison

to the relative concentrations collected via FTIR spectroscopy. The selection of the same reference point for all measurements places each measurement on a common, unit-less scale for direct comparison between methods. The relative short circuiting data from the GC methods closely follows delivery ratio at WOT, and agrees with the trend of data collected by FTIR spectroscopy for UHC. Additional variance is seen in the FTIR spectroscopy measurement of UHC.
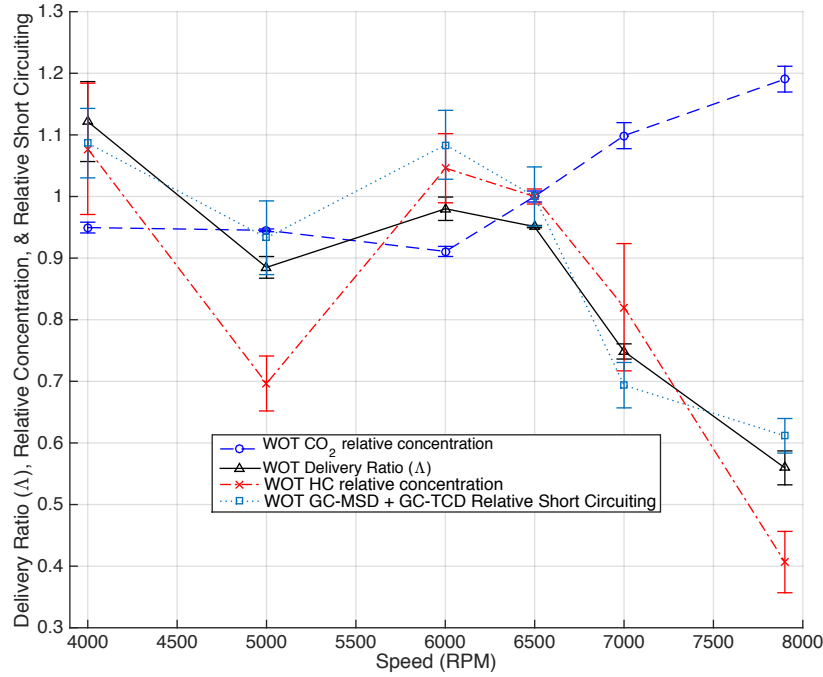
Figure 4.35. Relative concentrations of UHC and CO_2 at WOT.

Figure 4.36 shows the relative concentrations of UHC and CO_2 at PT conditions. The same reference condition of peak power at 6500 RPM and WOT was used to normalize this data set. Presence of UHC in the exhaust again follows delivery ratio. There is a maximum 21% concentration UHC at 4000 RPM relative to the reference point and a minimum of no detected UHC at 7000 RPM. The 7900 RPM operating condition had a significant increase in relative concentration of UHC. Relative con-

centrations of CO_2 are higher than the reference maximum due to further reduced dilution of combustion products by fresh charge short circuited in the exhaust.

The GC data for PT was normalized against peak power at WOT and 6500 RPM as well. The GC data shows that the relative short circuiting closely follows delivery ratio. The FTIR spectroscopy measurements indicate significantly lower UHC concentrations at all RPM than was detected through the GC methods.
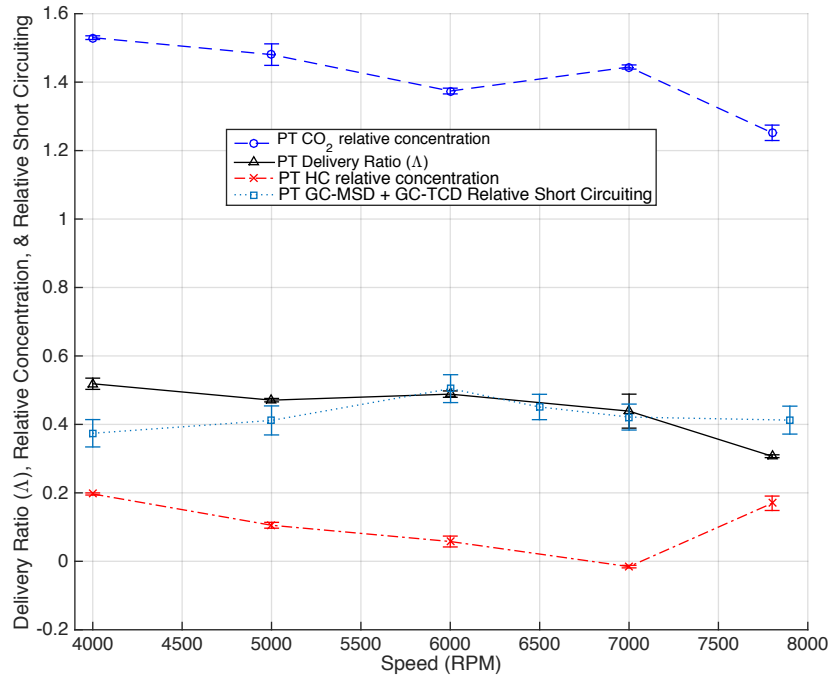
Figure 4.36. Relative concentrations of UHC and CO_2 at PT.

The comparison of gas chromatography and FTIR spectroscopy methods to detect concentration of UHC in the exhaust showed significant disagreement between the measurements. The short circuiting ratio, as measured by the GC technique, closely followed delivery ratio across the speed range at both WOT and PT. The FTIR spectroscopy measurements were able to capture the trends of the data but significant variance in the measurement exists. This variance was originally demonstrated in

Figure 4.19 where the relative concentration of UHC had a CoV of 24.3% while the engine was held on-condition at 6000 RPM and WOT. Each experimental method has its advantages and disadvantages though; the GC methods required a labor intensive collection of sample bags as well as hours of sample processing for final results while the FTIR spectroscopy measurement can be taken and analyzed in minutes for faster results. The GC methods are also unable to distinguish CO_2 from other species, giving FTIR spectroscopy a clear advantage in that case. Despite the limitations encountered, the use of FTIR spectroscopy for in-situ exhaust gas measurements was promising for its ability to quickly measure concentrations of exhaust species on a time-averaged basis. The development of time-resolved FTIR spectroscopy makes it an even more powerful tool than what is already being used.

V. Conclusions and Recommendations

This chapter will review the research objectives posed in Chapter I and describe the way in which they were met. The analysis and results found in Chapter IV will be summarized. Recommendations for ongoing and future work will be made based on the findings of this research effort.

5.1 Research Objectives

This work fulfilled the first two research objectives originally posed in Section 1.3, while partially fulfilling the third.

1. Quantify the parasitic losses on engine performance due to drivetrain friction on the small engine research bench and develop a correction for collected data.

2. Convert a 55 cm^3 two-stroke engine to electronic fuel injection, quantify performance, and compare to the performance of the carbureted configuration.

3. Develop both time-averaged and crank-angle resolved quantifications of exhaust gas emissions using FTIR spectroscopy.

A facility designed for testing small internal combustion engine known as the small engine research bench was used for data collection and testing in this effort. This facility was equipped with a dynamometer and full suite of engine diagnostic equipment to quantify the performance of the engines tested. The facility was equipped to operate three two-stroke engines with displacements of 28 cm^3, 55 cm^3, and 85 cm^3. These engines were chosen because they existed in a range where thermal losses were hypothesized to dominate the total losses experienced by the engine. The engines also shared many geometric similarities in design and have proven ideal candidates for comparative testing [20] [22].

5.2 Findings

The first phase of this research effort focused on the development of an apparatus to dynamically test and quantify the parasitic friction due to the moving components in the dynamometer drivetrain. A brushless electric motor was mounted on a reaction cradle designed to measure the torque produced while the drivetrain was spun. The difference in power measured at the dynamometer and the electric motor was found at speeds between 3000 RPM and 7000 RPM. A linear correction of 78.8 W per 1000 RPM was developed and applied to previous performance data collected by Rowton [22]. It was shown that engine performance improved significantly with the correction applied and that as much as 40% of the brake power produced by the engine was lost to drivetrain friction before it was measured by the dynamometer. This correction was implemented into the data analysis workflow of the small engine research bench to correct present and future data as well.

Conversion of the 55 cm^3 two-stroke engine to electronic fuel injection was performed using a kit that replaced the carburetor with a custom throttle body and fuel injector. A laboratory ECU was used to control the fuel injection system. The engine was tested at speeds between 4000 RPM and 7900 RPM. The small engine research bench was used to collect performance data on the engine. It was shown that peak power was comparable between carbureted and EFI configurations. Fuel consumption, as measured by BSFC, was reduced significantly with fuel injection. The engine was also tested at WOT and PT conditions in the EFI configuration. It was shown that at PT, engine power was reduced only 28% while intake air mass flow was reduced 47%, on average. The testing also revealed that PT BSFC decreased 26% over WOT conditions. The improvements in performance at part throttle were attributed to reduced pumping losses and most significantly, reduced short-circuiting across the speed range.

The 55 cm^3 engine equipped with EFI was used as the basis to develop the FTIR spectroscopy exhaust gas emission analysis capability. An optical probe was designed by the author and manufactured to allow in-situ measurements of the high-temperature exhaust gasses in the manifold. This optical probe was coupled to the FTIR spectrometer through fiber optics that enabled remote sensing. A crank-angle resolved step-scan measurement technique was developed and tested. It was found that due to aliasing of the interferograms, insufficient spectral data could be recovered. A time-averaged linear-scan measurement technique was used to collect spectral absorbance data at engine speeds ranging from 4000 RPM to 7900 RPM at both WOT and PT. The relative concentrations of CO_2 and UHC were found by integrating the area under the absorbance spectra at each operating condition and were compared to the reference condition of peak power at 6500 RPM and WOT. It was shown that the concentration of UHC follows the delivery ratio at WOT and PT and is an indicator of short-circuiting in the exhaust.

5.3 Conclusions

A few, primary conclusions can be drawn from this work. First, a dynamometer based experimental setup used for engine performance measurements requires an analysis of the friction introduced by the spinning components. In this case, it was found that the losses were far more than expected and could not be ignored. The use of an electric motor with the means to spin the drivetrain and measure power absorbed provides a consistent, repeatable method to quantify drivetrain friction and was used to obtain a correction factor.

Second, electronic fuel injection enabled superior fuel consumption on the 3W-55i engine, as compared to the carbureted configuration. The simple carburetors equipped from the factory tune did not adequately meter fuel to the engine and

created inefficient, fuel-rich conditions for most speeds tested. The dynamic process of scavenging in small two-stroke engines makes them highly sensitive to intake geometry and the fuel injection throttle body changed delivery ratio across the speed range. Care should be taken in any crankcase scavenged two-stroke application to ensure that performance is not adversely affected by a different throttle body design.

Third, Fourier transform infrared spectroscopy is a promising diagnostic technique for the measurement of exhaust gas concentrations in small, two-stroke engines. Interference of liquid phase UHC proved to be a significant challenge; however, UHC concentration data were collected that showed agreement with another, gas chromatography based, diagnostic method that measured short-circuiting in the exhaust. Linear scan FTIR spectroscopy techniques provide a quick way to collect time averaged data of the exhaust gas species. Step-scan FTIR spectroscopy incurred a significant SNR disadvantage due to the wide sample spacing and did not resolve any spectral data in these experiments. Step-scan mode is not useful in its current form with ICEs because of the prohibitively long tests required to for collection of sufficient spectral information.

5.4 Recommendations for Future Work

Several areas for further research were identified during this effort that would build understanding of the operation of small two-stroke internal combustion engines. The drivetrain friction measurement hardware was designed in a manner so that it could be attached in parallel to the engine and used for motored friction tests of the engine. Motored friction tests use an instrumented, external power-source such as an electric motor, to spin a non-firing engine and measure the amount of power lost to pumping and mechanical friction inside the engine. Motored friction is not always representative of friction in a running engine due to reduced loading on the bearings;

however, a significant body of work exists so results could be directly compared to other engines of various sizes.

The development of a technique to collect crank-angle resolved absorbance spectra remains an unsolved problem. An alternate technique to perform this measurement is available, which combines a repeating linear-scan measurement with engine position data to reconstruct crank-angle resolved interferograms and absorbance spectra. This technique has been proven to work by Rein [19] and development of the data-acquisition and processing capability is already underway as of this writing. Crank-angle resolved absorbance spectra are desired for the ability to show the variation of exhaust properties over time as the combustion products are replaced by short-circuited fresh charge. The advantages of linear-scan FTIR spectroscopy will be required to resolve the spectral information present in the challenging measurement environment of the engine exhaust. Combined with the time-averaged analysis capability, short circuiting can be fully investigated in the 28 cm^3, 55 cm^3, and 85 cm^3 two-stroke engines. Data collected from the three engines can be used to develop an understanding of how short circuiting may vary between engines of different sizes.

Finally a reduction of short-circuiting is possible through the use of a tuned exhaust manifold. A custom manifold designed for each of the three engines could be used to improve trapping efficiency and reduced short circuiting without sacrificing peak power of the engine. These manifolds are commonplace in modern two-stroke engines and take advantage of reflected pressure waves to force short-circuited fresh charge back into the cylinder.

Bibliography

1. Ausserer, Joseph K., Kevin P. Horn, Marc D. Polanka, Paul J. Litke, and Keith D. Grinstead. "Quantification of Short-Circuiting and Trapping Efficiency in a Small Internal Combustion Engine by GC-MS and GC-TCD". *SAE Small Engine Technology Conference*, 2015.

2. Ausserer, Joseph K, Paul J Litke, Jon-Russell Groenewegen, Alexander Rowton, Marc D Polanka, and Keith Grinstead. "Development of Test Bench and Characterization of Performance in Small Internal Combustion Engines". 2013. URL `http://dx.doi.org/10.4271/2013.32.9036`.

3. Ausserer, Joseph K., Alex K. Rowton, Keith D. Grinstead, Paul J. Litke, and Marc D. Polanka. "Comparison of In-Cylinder Pressure Measurement Methods in a Small Spark Ignition Engine". November 2014. URL `http://dx.doi.org/10.4271/2014.32.0007`.

4. Blair, G. P. "Prediction of Two-Cycle Engine Performance Charcteristics". *SAE Transactions*, 85, 1976. URL `http://dx.doi.org/10.4271/760645`.

5. Crosbie, Steven C. *Increasing Reliability of a Small 2-Stroke Internal Combustion Engine for Dynamically Changing Altitudes*. Thesis, Air Force Institute of Technology, March 2012.

6. Gierczak, Christine A., J. M. Andino, James W. Butler, G. A. Heiser, Gerald Jesion, and T. J. Korniski. "FTIR: Fundamentals and Applications in the Analysis of Dilute Vehicle Exhaust". *Proc. SPIE*, 1433:315–328, 1991. URL `http://dx.doi.org/10.1117/12.46178`.

126

7. Griffiths, Peter R. and James A. De Haseth. *Fourier Transform Infrared Spectrometry*. Chemical Analysis. Wiley-Interscience, Hoboken, N.J., 2nd edition, 2007. ISBN 9780471194040.

8. Herget, William F. and Steven R. Lowry. "Auto Exhaust Gas Analysis by FTIR Spectroscopy". *Proc. SPIE*, 1433:275–289, 1991. URL `http://dx.doi.org/10.1117/12.46171`.

9. Heywood, John B. *Internal Combustion Engine Fundamentals*. McGraw-Hill series in mechanical engineering. McGraw-Hill, New York, 1988. ISBN 007028637.

10. Heywood, John B and Eran Sher. *The Two-Stroke Cycle Engine*. Taylor & Francis Group, New York, 1999. ISBN 1560328312.

11. Hori, Kenji. "A Method of Measuring Scavenging Efficiency and its Application". *Bulletin of JSME*, 5(18):327–334, 1962. URL `http://dx.doi.org/10.1299/jsme1958.5.327`.

12. Husaboe, Travis D. *Effects of Temperature on the Performance of a Small Internal Combustion Engine at Altitude*. Master's thesis, Air Force Institute of Technology, March 2013.

13. Insitu, Inc. "Scan Eagle Product Card". 2015. URL `http://www.insitu.com/images/uploads/product-cards/ScanEagle.pdf`.

14. LumiaLabs. "SpectraPlot absorption tool". URL `http://spectraplot.com/absorption`.

15. Manning, Christopher J. and Richard A. Palmer. "Design Principles And Instrumentation For Step-Scan FTIR". *Proc. SPIE*, 1145:577–579, 1989. URL `http://dx.doi.org/10.1117/12.969610`.

16. Menon, Shyam and Christopher Cadou. "Scaling of Miniature Piston-Engine Performance Part 1: Overall Engine Performance". *Journal of Propulsion and Power*, 29(4):774–787, 2013. URL `http://dx.doi.org/10.2514/1.B34638`.

17. Menon, Shyam and Christopher Cadou. "Scaling of Miniature Piston-Engine Performance Part 2: Energy Losses". *Journal of Propulsion and Power*, 29(4):788–799, 2013. URL `http://dx.doi.org/10.2514/1.B34639`.

18. Ohigashi, Schunichi and Yoshisuke Hamamoto. "Cylinder Gas Composition of Small 2-Stroke Cycle Gasoline Engine". 1971. URL `http://dx.doi.org/10.4271/710143`.

19. Rein, Keith D. *High-Resoltuion Spectroscopic Measurement of Small Molecules in Combustion*. Thesis, University of Wisconsin - Madison, 2014.

20. Rittenhouse, Joshua A. *Thermal Loss Determination for a Small Internal Combustion Engine*. Thesis, Air Force Institute of Technology, March 2014.

21. Rittenhouse, Joshua A., Alexander K. Rowton, Joseph K. Ausserer, and Marc D. Polanka. "Preliminary Thermal Loss Measurements for a Small Internal Combustion Engine". 2014. URL `http://dx.doi.org/10.2514/6.2014.0529`.

22. Rowton, Alex K. *Measuring Scaling Effects in Small Two-Stroke Internal Combustion Engines*. Thesis, Air Force Institute of Technology, June 2014.

23. Rowton, Alex K, Joseph K Ausserer, Keith Grinstead, Paul J Litke, and Marc D Polanka. "Measuring Scaling Effects in Small Two-Stroke Internal Combustion Engines". 2014. URL `http://dx.doi.org/20.4271/2014.32.0010`.

24. Sher, Eran. "Scavenging the Two-Stroke Engine". *Progress in Energy and Combustion Science*, 1990. URL `http://dx.doi.org/10.1016/0360-1285(90)90045-5`.

25. Smith, Brian C. *Fundamentals of Fourier transform infrared spectroscopy.* CRC Press, Boca Raton, 1996. ISBN 0849324610.

26. Thorlabs. "Thorlabs fluroide multimode mid-IR fibers". URL `http://www.thorlabs.com/newgrouppage9.cfm?objectgroup_id=7062`.

27. USAF. "United States Air Force RPA Vector", 2013.

28. USMC. "ScanEagle in Iraq on Launcher", 2005. URL `http://www.usmc.mil/marinelink/image1.nsf/Lookup/2005417115454`.

29. Wilson, Cary W. *Performance of a Small Internal Combustion Engine Using N-Heptane and Iso-Octane.* Thesis, Air Force Institute of Technology, March 2010.

30. Zill, Dennis G. and Michael R. Cullen. *Advanced Engineering Mathematics.* Jones and Bartlett, third edition, 2006. ISBN 9780763779665.

REPORT DOCUMENTATION PAGE

Form Approved
OMB No. 0704–0188

1. REPORT DATE *(DD–MM–YYYY)*
05–29–2015

2. REPORT TYPE
Master's Thesis

3. DATES COVERED *(From — To)*
Sept 2013 — June 2015

4. TITLE AND SUBTITLE

Exhaust Composition in a Small Internal Combustion Engine Using FTIR Spectroscopy

5a. CONTRACT NUMBER

5b. GRANT NUMBER

5c. PROGRAM ELEMENT NUMBER

6. AUTHOR(S)

Horn, Kevin P. Capt, USAF

5d. PROJECT NUMBER

5e. TASK NUMBER

5f. WORK UNIT NUMBER

7. PERFORMING ORGANIZATION NAME(S) AND ADDRESS(ES)

Air Force Institute of Technology
Graduate School of Engineering and Management (AFIT/EN)
2950 Hobson Way
WPAFB OH 45433-7765

8. PERFORMING ORGANIZATION REPORT NUMBER

AFIT-ENY-MS-15-J-042

9. SPONSORING / MONITORING AGENCY NAME(S) AND ADDRESS(ES)

Department of Aeronautical Engineering
2950 Hobson Way
WPAFB OH 45433-7765
DSN 271-0690, COMM 937-255-3636
Email: marc.polanka@afit.edu

10. SPONSOR/MONITOR'S ACRONYM(S)

11. SPONSOR/MONITOR'S REPORT NUMBER(S)

12. DISTRIBUTION / AVAILABILITY STATEMENT

DISTRIBUTION STATEMENT A:
APPROVED FOR PUBLIC RELEASE; DISTRIBUTION UNLIMITED.

13. SUPPLEMENTARY NOTES

This material is declared a work of the U.S. Government and is not subject to copyright protection in the United States.

14. ABSTRACT

The mission-specific needs of small, remotely piloted aircraft demand lighter, more efficient engines with increased performance for their propulsion systems. A wide range of experimental efforts were undertaken to further the ability to obtain performance data on small engines as well as to develop understanding of their operation. Data were collected to quantify friction losses present in the dynamometer drivetrain on the small engine research bench. A correction and calibration model was developed for brake power collected by the dynamometer. Mechanical efficiencies for 28 cm^3, 55 cm^3 and 85 cm^3 engines were 92.4%, 91.3% and 89.7%, respectively. Maximum fuel conversion efficiency for the three engines was calculated to be 14.9%, 15.4% and 18.3% at peak power, respectively. A 55 cm^3 two-stroke engine was converted to electronic fuel injection and its performance was tested and compared to the same engine equipped with a carburetor. Peak power was comparable between carbureted and EFI configurations. Fuel consumption, as measured by brake specific fuel consumption, was reduced significantly. Time-averaged and crank-angle resolved methods for the analysis of exhaust gasses in a 55 cm^3 two-stroke engine using Fourier transform infrared spectroscopy (FTIR) were developed and tested. Spectral features for CO_2 and unburnt hydrocarbons (UHC) were resolved. The time-averaged absorbance measurements showed that short-circuiting, as a function of the concentration of UHC, followed delivery ratio (Λ) at wide open throttle.

15. SUBJECT TERMS

FTIR, spectroscopy, internal combustion engine, UAV, RPA, two-stroke engine, exhaust composition

16. SECURITY CLASSIFICATION OF:

a. REPORT	b. ABSTRACT	c. THIS PAGE
U	U	U

17. LIMITATION OF ABSTRACT
U

18. NUMBER OF PAGES
148

19a. NAME OF RESPONSIBLE PERSON
Dr. Marc D. Polanka, AFIT/ENY

19b. TELEPHONE NUMBER *(include area code)*
(937) 255-3636, x4714; marc.polanka@afit.edu

Standard Form 298 (Rev. 8–98)
Prescribed by ANSI Std. Z39.18